

School of Electrical and Information Engineering  
University of the Witwatersrand, Johannesburg  
Private Bag 3, 2050, Johannesburg, South Africa

**ELEN4000: Design Project**  
**ANTENNA ARRAY DESIGN TO DETECT AND TRACK MAN MADE SPACE**  
**DEBRIS IN LOW EARTH ORBIT**  
23 October 2018

**Supervisor:** Dr. R Dreyer

Kelvin da Silva  
835842  
835842@students.wits.ac.za

**ABSTRACT**

This paper presents the theoretical design of a ground based phased array radar to detect and track space debris in Low Earth Orbit (LEO). The system takes the form of a  $76 \times 76$  planar array made up of 5776 half-wave crossed dipole elements operating at a frequency of 440 MHz. The radar system was configured in a monostatic topology and operated in a pulsed wave mode with a pulse width of  $37 \mu\text{s}$  and a pulse repetition frequency of 64.86 Hz. A Gaussian power distribution was applied to the elements of the array. The phased array has a maximum gain of 46.54 dBi and a minimum half power beam width (HPBW) of  $0.83^\circ$  when directed along array bore sight. After performing a sensitivity analysis on the system, it was found that the gain decreased, HPBW increased and side lobes gains increased as the steering angle departed from bore sight. The field of view (FOV) was defined as the angle range up to which perfectly conducting spherical debris having radii of 5 cm could be detected with a signal to noise ratio of  $\geq 7 \text{ dB}$  while the sensitivity of the side lobe was less than that of the main lobe. In the  $\phi=0^\circ$  and  $\phi=90^\circ$  planes the FOV had an angular extent of  $\theta=\pm 25^\circ$ . In the  $\phi=45^\circ$  and  $\phi=135^\circ$  planes the FOV had an angular extent of  $\theta=\pm 35^\circ$ . At the furthest extent of the FOV, the gain of the steered beam was 42.70 dBi and the HPBW was  $1.09^\circ$  and was able to detect a 5 cm radius sphere up to altitudes of approximately 1000 km. Through neglecting signal processing as well as data transfer and communication infrastructure of the system, a cost analysis was performed and was found to cost R 664 795 697.90. Future work in the areas of maintaining the maximum gain of the main beam when steering has been recommended.

**Keywords:** crossed dipole, LEO, monostatic, radar, phased array, pulsed wave, space debris, steering.

**Contents**

<b>1. INTRODUCTION</b>	<b>1</b>
<b>2. BACKGROUND</b>	<b>1</b>
2.1 Problem Statement . . . . .	1
2.2 Requirements and success criteria . . . . .	2
<b>3. LITERATURE REVIEW</b>	<b>2</b>
3.1 Radar . . . . .	2
3.2 Radar Topologies . . . . .	2
3.3 Propagation Environment . . . . .	3
3.4 Transmission Losses . . . . .	3
3.5 Existing Solutions of Application . . . . .	4
<b>4. DESIGN SYNTHESIS</b>	<b>5</b>
4.1 System Overview . . . . .	5
4.2 Operating Frequency . . . . .	6
4.3 Radar Technology and Topology . . . . .	6
4.4 Single Array Element . . . . .	7
4.5 Optimizing Array Gain . . . . .	7
4.6 Optimizing Side Lobes . . . . .	8
4.7 Matching . . . . .	9
4.8 SNR and Debris . . . . .	9
4.9 Feeding Network . . . . .	10
4.10 Phasing Network . . . . .	11
4.11 System Location . . . . .	11
<b>5. OPTIMIZATION</b>	<b>12</b>
<b>6. CRITICAL ANALYSIS</b>	<b>13</b>
6.1 Environmental Impact . . . . .	13

6.2	Performance . . . . .	13
6.3	Cost Breakdown . . . . .	14
<b>7.</b>	<b>DISCUSSION</b>	<b>14</b>
7.1	Trade-offs . . . . .	14
7.2	Future Work . . . . .	15
<b>8.</b>	<b>CONCLUSION</b>	<b>15</b>
<b>A</b>	<b>Non-Technical Report</b>	<b>i</b>
<b>B</b>	<b>Single Element Radiation Patterns</b>	<b>iii</b>
<b>C</b>	<b>Array Radiation Patterns</b>	<b>v</b>
<b>D</b>	<b>Power Distribution</b>	<b>viii</b>
<b>E</b>	<b>Antenna and Feeding Network Matching</b>	<b>viii</b>
<b>F</b>	<b>Debris Orbit Altitude-Range Model</b>	<b>xi</b>
<b>G</b>	<b>Cost-Performance Optimization Algorithm</b>	<b>xi</b>
<b>H</b>	<b>Sensitivity Analysis and Steering</b>	<b>xiii</b>
<b>I</b>	<b>Cost Analysis</b>	<b>xxxii</b>

## List of Figures

1	System block diagram shown through a single element in the phased array. . . . .	5
2	Relationship between number of elements per row/column and gain for optimal parameters.	8
3	Power distribution of elements in the peripheral and centre row in the phased array. . . .	9
1	Radiation pattern of a single half-wave crossed dipole antenna cut through $\phi = 0^\circ$ . . . .	iii
2	Radiation pattern of a single half-wave crossed dipole antenna cut through $\phi = 45^\circ$ . . . .	iii
3	Radiation pattern of a single half-wave crossed dipole antenna placed $\frac{\lambda}{4}$ above an infinite ground plane cut through $\phi = 0^\circ$ . . . . .	iv
4	Radiation pattern of a single half-wave crossed dipole antenna placed $\frac{\lambda}{4}$ above an infinite ground plane cut through $\phi = 45^\circ$ . . . . .	iv

5	Radiation pattern of a 64x64 array with optimal $d$ and $h$ values and uniform distribution through a $\phi = 0^\circ$ cut. . . . .	v
6	Radiation pattern of a 64x64 array with optimal $d$ and $h$ values and uniform distribution through a $\phi = 45^\circ$ cut. . . . .	v
7	Radiation pattern of a 64x64 array with optimal $d$ and $h$ values and uniform distribution through a $\phi = 90^\circ$ cut. . . . .	vi
8	Radiation pattern of the final 76x76 array with non-uniform distribution $\phi = 0^\circ$ cut. . .	vi
9	Radiation pattern of the final 76x76 array with non-uniform distribution $\phi = 45^\circ$ cut. . .	vii
10	Radiation pattern of the final 76x76 array with non-uniform distribution $\phi = 90^\circ$ cut. . .	vii
11	Heat-map representation of the power distribution of the 76x76 planar phased array. . .	viii
12	VSWR of each dipole in the half wave crossed dipole when matched to a $50 \Omega$ source. . .	viii
13	Mismatch loss of each dipole in the half-wave crossed dipole element. . . . .	ix
14	The real component of impedance for each dipole in the half-wave crossed dipole element.	ix
15	The imaginary component of impedance for each dipole in the half-wave crossed dipole element. . . . .	x
16	Visual representation of distributed feed network matching. . . . .	x
17	Visual representation of the relationship between debris altitude and radar range. . . .	xi
18	Flow diagram of the algorithm used in determining the optimal number of elements per row/column in the $n \times n$ phased array. . . . .	xii
19	Resulting radiation pattern when system is steered to $\phi=0^\circ, \theta=5^\circ$ . . . . .	xiii
20	Resulting radiation pattern when system is steered to $\phi=0^\circ, \theta=10^\circ$ . . . . .	xiii
21	Resulting radiation pattern when system is steered to $\phi=0^\circ, \theta=15^\circ$ . . . . .	xiv
22	Resulting radiation pattern when system is steered to $\phi=0^\circ, \theta=20^\circ$ . . . . .	xiv
23	Resulting radiation pattern when system is steered to $\phi=0^\circ, \theta=25^\circ$ . . . . .	xv
24	Resulting radiation pattern when system is steered to $\phi=45^\circ, \theta=5^\circ$ . . . . .	xv
25	Resulting radiation pattern when system is steered to $\phi=45^\circ, \theta=10^\circ$ . . . . .	xvi
26	Resulting radiation pattern when system is steered to $\phi=45^\circ, \theta=15^\circ$ . . . . .	xvi
27	Resulting radiation pattern when system is steered to $\phi=45^\circ, \theta=20^\circ$ . . . . .	xvii
28	Resulting radiation pattern when system is steered to $\phi=45^\circ, \theta=25^\circ$ . . . . .	xvii
29	Resulting radiation pattern when system is steered to $\phi=45^\circ, \theta=30^\circ$ . . . . .	xviii
30	Resulting radiation pattern when system is steered to $\phi=45^\circ, \theta=35^\circ$ . . . . .	xviii

31	Sensitivity of the main beam when the system is steered to $\phi=0^\circ$ , $\theta=0^\circ$ . . . . .	xix
32	Sensitivity of the most dominant side lobe ( $\theta=\pm 2.99^\circ$ ) when the system is steered to $\phi=0^\circ$ , $\theta=0^\circ$ . . . . .	xix
33	Sensitivity of the main beam when the system is steered to $\phi=0^\circ$ , $\theta=5^\circ$ . . . . .	xx
34	Sensitivity of the most dominant side lobe ( $\theta=-2.01^\circ$ ) when the system is steered to $\phi=0^\circ$ , $\theta=5^\circ$ . . . . .	xx
35	Sensitivity of the main beam when the system is steered to $\phi=0^\circ$ , $\theta=10^\circ$ . . . . .	xxi
36	Sensitivity of the most dominant side lobe ( $\theta=-78.5^\circ$ ) when the system is steered to $\phi=0^\circ$ , $\theta=10^\circ$ . . . . .	xxi
37	Sensitivity of the main beam when the system is steered to $\phi=0^\circ$ , $\theta=15^\circ$ . . . . .	xxii
38	Sensitivity of the most dominant side lobe ( $\theta=-63.5^\circ$ ) when the system is steered to $\phi=0^\circ$ , $\theta=15^\circ$ . . . . .	xxii
39	Sensitivity of the main beam when the system is steered to $\phi=0^\circ$ , $\theta=20^\circ$ . . . . .	xxiii
40	Sensitivity of the most dominant side lobe ( $\theta=-54.5^\circ$ ) when the system is steered to $\phi=0^\circ$ , $\theta=20^\circ$ . . . . .	xxiii
41	Sensitivity of the main beam when the system is steered to $\phi=0^\circ$ , $\theta=25^\circ$ . . . . .	xxiv
42	Sensitivity of the most dominant side lobe ( $\theta=-47^\circ$ ) when the system is steered to $\phi=0^\circ$ , $\theta=25^\circ$ . . . . .	xxiv
43	Sensitivity of the main beam when the system is steered to $\phi=45^\circ$ , $\theta=5^\circ$ . . . . .	xxv
44	Sensitivity of the most dominant side lobes ( $\phi=173^\circ$ , $\theta=-3.5^\circ$ and $\phi=97^\circ$ , $\theta=3.5^\circ$ ) when the system is steered to $\phi=45^\circ$ , $\theta=5^\circ$ . . . . .	xxv
45	Sensitivity of the main beam when the system is steered to $\phi=45^\circ$ , $\theta=10^\circ$ . . . . .	xxvi
46	Sensitivity of the most dominant side lobes ( $\phi=170^\circ$ , $\theta=-7^\circ$ and $\phi=100^\circ$ , $\theta=7^\circ$ ) when the system is steered to $\phi=45^\circ$ , $\theta=10^\circ$ . . . . .	xxvi
47	Sensitivity of the main beam when the system is steered to $\phi=45^\circ$ , $\theta=15^\circ$ . . . . .	xxvii
48	Sensitivity of the most dominant side lobes ( $\phi=169^\circ$ , $\theta=80.5^\circ$ and $\phi=101^\circ$ , $\theta=-80.5^\circ$ ) when the system is steered to $\phi=45^\circ$ , $\theta=15^\circ$ . . . . .	xxvii
49	Sensitivity of the main beam when the system is steered to $\phi=45^\circ$ , $\theta=20^\circ$ . . . . .	xxviii
50	Sensitivity of the most dominant side lobes ( $\phi=165^\circ$ , $\theta=70.5^\circ$ and $\phi=105^\circ$ , $\theta=-70.5^\circ$ ) when the system is steered to $\phi=45^\circ$ , $\theta=20^\circ$ . . . . .	xxviii
51	Sensitivity of the main beam when the system is steered to $\phi=45^\circ$ , $\theta=25^\circ$ . . . . .	xxix
52	Sensitivity of the most dominant side lobes ( $\phi=161^\circ$ , $\theta=65^\circ$ and $\phi=109^\circ$ , $\theta=-65^\circ$ ) when the system is steered to $\phi=45^\circ$ , $\theta=25^\circ$ . . . . .	xxix
53	Sensitivity of the main beam when the system is steered to $\phi=45^\circ$ , $\theta=30^\circ$ . . . . .	xxx

54	Sensitivity of the most dominant side lobes ( $\phi=156^\circ$ , $\theta=61^\circ$ and $\phi=114^\circ$ , $\theta=-61^\circ$ ) when the system is steered to $\phi=45^\circ$ , $\theta=30^\circ$ . . . . .	xxx
55	Sensitivity of the main beam when the system is steered to $\phi=45^\circ$ , $\theta=35^\circ$ . . . . .	xxxi
56	Sensitivity of the most dominant side lobes ( $\phi=152^\circ$ , $\theta=58.5^\circ$ and $\phi=118^\circ$ , $\theta=-58.5^\circ$ ) when the system is steered to $\phi=45^\circ$ , $\theta=35^\circ$ . . . . .	xxxi

## List of Tables

1	Summary of the properties of the phased array radar . . . . .	xxxii
2	Cost analysis for the construction of the phased array radar . . . . .	xxxiii

## 1. INTRODUCTION

Space debris consists of a range of man-made objects including satellite fragments, rocket stages as well as payloads and remnants of payload systems accumulated over several decades. Due to the initial negligence of the possible accumulation of space travel discards, there is a significant volume of objects present at Low Earth Orbit (LEO). These objects pose a serious threat for current and future space operations.

Therefore, a system that is capable of detecting and tracking these objects for the purpose of protecting and preserving active space infrastructure is necessary. The theoretical design of a ground based phased array radar for this application is conducted.

Essential literature necessary for purpose of making informed design decisions and a summary of currently existing solutions addressing the issue of LEO debris tracking was included in a literature review. Thereafter, the system design synthesis was highlighted and all design choices were discussed. A cost-performance optimization was performed to find the intersection between acceptable performance characteristics and low cost. A critical analysis was performed to determine the capabilities of the system and discuss its limitations. A cost analysis was performed, followed by the highlighting of major trade-offs in design choices and future recommendations to improve the device.

## 2. BACKGROUND

### 2.1 Problem Statement

The presence of LEO space debris results in a chain reaction phenomenon known as the Kessler Syndrome [1, 2]. This is the term given to the fact that having an increased number of these objects acts as an obstacle for spacecraft manoeuvres, which would in turn increase the risk and number of collisions, and inherently further increase the volume of space debris as a result [2]. The task of detecting and tracking the orbits of these objects is challenging and the devastating effects of not being able to do so are illustrated by the collision of the decommissioned Russian *Kosmos-2251* satellite with the active *Iridium-33* satellite in 2009 [1]. The consequence of the destruction of the active satellite was a loss of communication services on Earth supported by the satellite [1]. Most of the debris resulting from the collision currently orbit the Earth at speeds up to  $8 \text{ km.s}^{-1}$  and act as obstacles that threaten the safety of communication infrastructure in space required to sustain the activities of modern global society.

For this reason, an appropriate countermeasure for the purpose of minimizing the incidents of collisions is necessary. There are three main approaches to mitigating the space debris problem: collision avoidance, shielding and removal. Each approach is best suited for space debris of different sizes. For objects that are larger than 10 cm, collision avoidance is the chosen approach while applying shielding infrastructure to spacecraft bodies is the chosen mitigation technique when dealing with objects smaller than this. Collision avoidance includes the ability to detect the location of existing debris in LEO. Thicker shielding may be constructed to protect spacecraft from larger objects but this increases the cost of spacecraft manufacturing significantly. Space junk removal is appropriate for reducing the amount of space debris for a range of dimensions and several companies in the space industry are directing technological advancements in this direction [3]. While all three approaches have a role in improving Space Situational Awareness (SSA), collision avoidance is essential in improving the efficiency in the deployment of space debris cleanup strategies as well as to preserve current LEO space infrastructure. Furthermore, it is currently the approach that appears to be the most cost effective and sustainable. It is for the above mentioned reasons that a radar system to detect and track LEO space debris must be designed.

## 2.2 Requirements and success criteria

The design of a measurement system capable of detecting and tracking the trajectory of LEO (200-1800 km) space debris is required. In addition to being able to identify the altitude of the detected debris, the system must be able to track the debris detected in LEO such that its trajectory may be monitored. The infrastructure of the system must ensure that spherical debris having radii as small as 5 cm can be detected.

The focus of the design synthesis will be mainly on the design of the phased array antenna aspects of the system. Furthermore, the analysis of the cost of the design is required and the system is to be optimized accordingly. While the signal processing portion of the system is essential, complete design of this sub-system is beyond the scope of the system design. However, consideration of the subsystem must be included when analysing the sensitivity and capabilities of the system. Based on the knowledge of distribution density of debris in LEO, the field of view (FOV) of the system must be maximized to be able to detect spherical debris with 5 cm radii at altitudes up to 900-1000 km and 1400-1500 km. Lastly, an analysis of the environmental impact that the system will create must be scrutinized.

## 3. LITERATURE REVIEW

### 3.1 Radar

As defined in the applicable IEEE standard, a radar is device that transmits electromagnetic (EM) signals and receives echoes from objects of interest (targets) within its volume or range of interest [4, 5]. In a addition to detecting the presence of a target, a radar can provide the following information about a target: distance (range) using the elapsed time of transmission of the signal and reception of the returned signal; direction through the implementation of directive antenna patterns; rate of change of range by monitoring Doppler shift; description or classification of the target by analysing the variation of echoes with time [5].

The radar that is to be designed must be capable of target detection and target tracking. Target detection is the ability of the radar to distinguish the target at the receiver. In practical scenarios, the echo signal at the receiver consists of the target, noise, clutter as well as interference [5]. Clutter refers to the unwanted but correlated echoes originating from unwanted targets while interference represents unintentionally acquired signals such as radio, TV and intentional jamming signals [1, 5]. Noise is simply the uncorrelated, unwanted signals originating from receiver circuitry. Target tracking involves the process of following a moving target continuously. In doing so, the range, direction and velocity of the target can be determined. Tracking can be implemented mechanically or electronically. In terms of mechanical tracking, this approach has a significant limitation as to only being able to track a single target at a time. The electronic approach utilizes digital beam steering techniques to perform single-target as well as multitarget tracking. Since detections and tracking of space debris would require multitarget tracking, electronic tracking is more suited toward the application.

### 3.2 Radar Topologies

Radar systems can be implemented in accordance to different topologies namely: monostatic and multistatic. A monostatic radar system is one that involves the receiver and the transmitter being co-located or whereby the same antenna is used as both the transmitter and receiver of the radar [6]. A multistatic configuration is represented by a radar system that has multiple separated transmitters and receivers [1, 7]. The bistatic configuration is a subset of the multistatic configuration as it consists of a single transmitter and receiver antenna that are separated [1, 7]. Radar systems can also be classified into active and passive systems. Active radar systems are designed such that a signal is intentionally transmitted for the purpose of detecting targets whereas a passive radar system utilizes



stray EM radiation from existing broadcasting infrastructure on Earth as a transmitter/s and only requires the design of a radar receiver [1, 7].

In terms of target detection resolution, a multistatic configuration is superior to that of a monostatic arrangement because it has an increased number of observable scattering angles [7]. However, the increased resolution is dependent on the baseline between transmitter/s and receiver/s which implies that a large portion of land is required for its implementation (significantly increasing cost) [8]. The configuration may involve utilizing different properties which adds to the complexity of finding a suitable location for the implementation. Through implementation of multistatic topology, sensitivity is increased substantially since more receiving antennas leads to increased sensitivity. Essentially a trade off between cost and sensitivity as well as resolution exists. Additionally, under the assumption that TV or Radio broadcasting signals are used in a passive system, the radar will be limited to operating in a continuous wave (CW) mode instead of pulsed wave (PW) mode implying that it will only have the ability to track and determine the velocity of the target will not be able to offer range information which is essential for improving SSA. PW mode also requires less supplied power to operate per unit time.

### 3.3 *Propagation Environment*

As mentioned in the previous section, the direct environment of a ground-based radar system will consist of noise, clutter and interference. By locating the ground-based radar in certain locations, the effects of these interfering signals can be minimized. Design choices regarding these issues will be discussed in Section 4.11. The ionosphere is a portion of the Earth's atmosphere that is of significant importance when dealing with EM wave propagation. The ionosphere is made up of three layers, namely D, E and F layers ranging from nearest to the Earth's surface to farthest respectively. The ionosphere is not uniformly distributed around the Earth but the maximum extent of this layer spans 75-1000 km above the Earth's surface [5, 9]. The D layer (lowest layer of the ionosphere) absorbs EM waves and results in propagation loss. Layers E and F affect EM waves by bending them towards the Earth's surface and therefore act as a reflecting upper boundary in the earth-ionosphere waveguide utilized in TV and radio broadcasting [5]. This waveguide can be used effectively up to the frequencies of 45-50 MHz. EM waves with frequencies higher than 50 MHz are not bent and can escape to outer space. This implies that the frequency of transmission for the application of detecting and tracking space debris should be greater than this frequency. The upper bound of appropriate frequencies for the application will be dependent on the minimum size of the debris that is desired to be detected efficiently as well as atmospheric losses.

An additional effect of the ionosphere is that of polarization rotation [10]. When the EM wave passes through the ionosphere, it interacts with the layers of ionized electrons that move according to the Earth's magnetic field [10]. The direction in which these electrons move are not parallel to the electric field of the wave and therefore the polarization of the wave may be shifted. This phenomenon is known as Faraday rotation [10]. The issue becomes significant when dealing with frequencies less than 10 GHz and more specifically when EM waves are linearly polarized. The polarization of the wave is distorted and the receiver will be incorrectly polarized in relation the echo arriving back at the receiver resulting in major signal losses. By circularly polarizing the transmitted wave, the Faraday rotation will add to the polarization and will remain circular [10].

### 3.4 *Transmission Losses*

Transmission losses may be divided into propagation losses and local losses. Atmospheric losses and free space loss make up propagation losses while local losses consist of equipment losses or specifically, feeder losses [10]. Local losses are directly related to antenna matching as well as feeding network matching which will be discussed in Section 4.9. Free space loss is the decreasing power density of the signal as it is radiated spherically from the signal source [5, 10]. The monostatic radar range

equation shown in Equation 1 inherently accounts for free space losses experienced travelling towards and returning from the space debris target whereby  $P_r$  is the power received from the echo of the target (W),  $P_t$  is the peak transmitted power (W),  $G_t$  is the transmitter gain,  $G_r$  is the receiver gain,  $\sigma$  is the radar cross section (RCS) of the target ( $\text{m}^2$ ),  $\lambda$  is the wavelength of the centre frequency of the transmitted signal (m) and  $r$  is the distance from the transmitter/receiver to the target (m) [5].

$$P_r = \frac{P_t G_t}{4\pi r^2} \sigma \frac{1}{4\pi r^2} \frac{\lambda^2 G_r}{4\pi} \quad (1)$$

In Equation 1, the first fraction term represents the power density that the radar transmitter produces at the target. The product of this term and the  $\sigma$  term is the hypothetical power intercepted by the radar target [5]. The second fraction term represents the isotropic spreading of the target intercepted power back at the radar receiver and is a power density [5]. The last fraction term is the effective aperture of the radar receiver and when multiplied by the power density, is the the total power collected by the radar receiver [5].

Atmospheric losses are caused by EM molecular absorption by oxygen and water vapour molecules in the atmosphere [11]. These losses increase gradually as frequency is increased and has resonant peaks at 22.3 GHz due to water vapour molecules and at 60 GHz due to oxygen [10, 11]. According to [11], the attenuation decreases with increasing altitude and usually can be neglected at altitudes greater than 10 km. Literature analysing atmospheric losses per km of signal propagation across frequency range normally do not consider frequencies below 1 GHz and those that do consider them approximate the loss per km in the order of  $10^{-3} \text{ dB.km}^{-1}$  [10, 11]. Therefore, for the application of detecting space debris at a minimum altitude of 200 km, atmospheric losses may be neglected if the operating frequency is less than 1 GHz.

### 3.5 Existing Solutions of Application

Due to the severity of the consequences and cost of destruction of operational devices in space, recent years have displayed an introduction into the detection and tracking of space debris. The majority of current available literature on the topic investigates possible solutions using radar techniques. Going beyond investigations, a company called LEOLABS was established in 2016 for the purpose of developing a worldwide network of ground-based, phased array radars that provide high resolution data of objects in LEO [12]. The company currently utilizes a 2-D planar phased array called the Poker Flat Incoherent Scatter Radar (PFISR) as well as a 1-D phased array making use of a reflector called the Midland Space Radar (MSR) [12].

The PFISR and the MSR are existing monostatic radar solutions [5]. Furthermore, both of these systems are active radar systems. There are certain advantages and disadvantages with each radar system. The PFISR has a system gain of 43 dBi and a peak transmitted power value of 2 MW [13]. These high gain and peak transmitted power values are necessary to illuminate a large enough area within the Earth's LEO region. The 2-D array results in the synthesis of a radiation pattern that allows for space debris in orbits passing through the field of view (FOV) to be detectable regardless of the direction they are travelling in. The star shaped FOV extends approximately  $\pm 30^\circ$  from the bore sight of the array implying that debris travelling through the centre of the FOV would be detectable for a maximum angular distance of  $60^\circ$  [6, 14, 15]. The main beam, that has a half power beam-width (HPBW) of approximately  $1^\circ$  can be pointed to any direction within the FOV [14, 15]. This means that more cases of detected objects have an increased chance of being tracked. While PFISR is sensitive to space objects varying in size from 10 cm or larger in diameter within LEO altitudes, it requires a high peak transmit power [14, 15].

The MSR offers the same functionality as the PFISR, however, due to its one dimensional construction, its FOV is also one dimensional [6, 12]. The FOV ranges  $\pm 60^\circ$  from the bore sight of the array in the East-West direction approximately  $\pm 1^\circ$  from the bore sight in the North-South direction [6, 12]. This

implies that there is an increased area and probability of detecting debris travelling in one direction compared to the other. The major advantage of the MSR, from a cost and environmental point of view is the fact that it only transmits 65 kW of peak power which is considerably less than that of the PFISR [6, 12]. According to LEOLAB's open source data platform, over the course of the year of 2018, an average of 10 000 objects were tracked using the PFISR whereas an average of 6 000 objects were tracked with the MSR each month [12]. Evidently, having a multidimensional FOV aids in detecting and tracking more objects in space. Both the PFISR and the MSR operated within the UHF range at 450 MHz and 440 MHz respectively [6, 12, 14, 15].

There is also existing literature on feasibility studies on the detecting and tracking of LEO space debris using bi-static radar topologies [1, 2]. The bi-static radar configuration named BIRALET (Bi-static Radar for LEO tracking) was used to detect a specific set of space debris at 410 MHz by using the FTS of the Italian Joint Test Range as the transmitter and the Sardinia Radio Telescope (SRT) as the receiver antenna [2]. The SRT has a gain of 47 dBi and a HPBW of  $0.8^\circ$ . The FTS has a gain of 13 dBi, a transmitter power of 4 kW and a HPBW of  $30^\circ$  [2]. Essentially, the aim is to illuminate a large region of LEO and use a highly directive receiver to detect echoes from targets. The results obtained from measuring a selected group of space debris indicated that the best result obtained from the system was detecting and tracking an object with an RCS of  $0.5 \text{ m}^2$  at an altitude of 948.8 km [2]. It should be noted that all the results were obtained when the space debris were approximately equidistant (in terms of range) between the transmitter and the receiver. Further, the RCS can be translated to a spherical object with a diameter of approximately 80 cm.

Another example of a bi-static radar that has been investigated is the Murchison Widefield Array (MWA) [1]. This radar system takes the form of a passive technology in a sense that the MWA acts as the receiver while several FM radio stations (87.5-108 MHz) act as transmitters. The transmitted power is modelled as 100 kW and the MWA beam was roughly  $40^\circ$ . The system was found to feasibly detect objects with a radius of 0.5 m or greater at altitudes up to 1000 km. While the development of a system such as this one appears to be efficient, it should be noted that the installation of the receiver antennas is required to be in an extremely radio quiet area. Furthermore, since the transmitted signal is a continuous wave (CW), range information of the detected target remain unknown.

## 4. DESIGN SYNTHESIS

### 4.1 System Overview

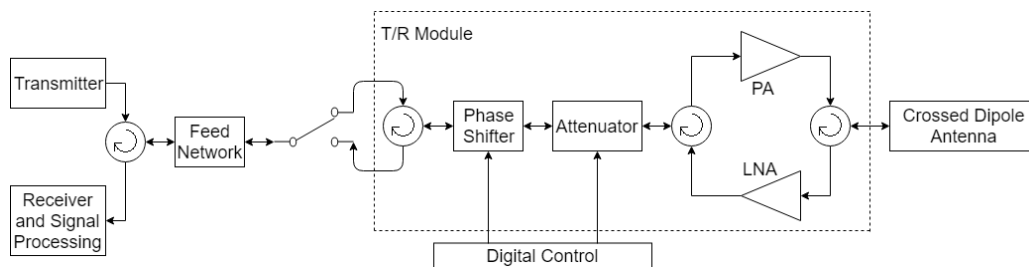


Figure 1: System block diagram shown through a single element in the phased array.

The active monostatic radar makes use of a planar square array ( $76 \times 76$ ) made up of 5776 half-wave crossed dipoles when transmitting pulses into space and receiving echoes from debris in LEO. In transmission mode, a pure tone is generated and sent to each transceiver module in the array via a distributed feed network. Each transceiver module is able to be digitally controlled in terms of phase delays and amount of power sent to each element in the array. This control will be used to electronically steer the direction in which an EM wave must be transmitted and received. The manipulated tone is then amplified by a high power amplifier (PA) and finally radiated from each

element in the array. In receiving mode, an echo from a detected target is received from each element in the array. The received signal is sent to the transceiver module and amplified by a low noise amplifier (LNA). Circulators ensure that the received signal does not travel toward the output of the PA. The signal can be manipulated further with digital control. The signals from each transceiver module are sent through the feeding network where they are combined and collected. This resultant signal then undergoes signal processing to determine the range of the target as well as the direction it is travelling in. Figure 1 illustrates the path of the signals in both modes for a single element.

## 4.2 Operating Frequency

Based on the information provided in the literature review, it was decided that the most appropriate frequency for detecting space debris having a diameter of approximately 10 cm was within the UHF band (0.3-2 GHz) but no higher than 1 GHz [5, 10, 11]. Since LEOLABS is a currently existing and successful solution provider in detecting and tracking space debris the operating frequency of 440 MHz was selected as this frequency is within the usable frequency range of the PFISR [6, 10–13]. The wavelength of the an EM wave corresponding to this frequency is 68.18 cm. If the debris to be detected is assumed to be spherical, the geometrical scattering limit is to be utilized when approximating the RCS of a sphere having a radius ( $a$ ) greater than or equal to  $0.5\text{ m}$  since  $\lambda \ll 2\pi a$ . The geometrical scattering limit allows the RCS of an object to be calculated as  $\sigma = \pi a^2$  [1]. When the wavelength  $\lambda > 2\pi a$ , the RCS is described by Rayleigh scattering as  $\sigma = 9\pi a^2 (\frac{2\pi a}{\lambda})^4$  [1]. While the RCS of objects is reduced significantly according to Rayleigh scattering, it was seen to be a suitable trade-off decision compared using higher frequency and having significant propagation losses.

Throughout the later stages in the development of the system, it was discovered that the 440 MHz falls under the Amateur Radio-location frequency allocation in South Africa [16]. For this reason, all dimensions of the designed system will not only be provided in metric units but also in terms of wavelength as the solution will be scalable according to frequency. In future developments of the system, a frequency band dedicated to space research or astrological research should be selected [16]. The effect of using a frequency within the Amateur Radio-location band would be an increased level of interference but this can be minimized by selecting an implementation location that is radio silent. Furthermore, echoes from target debris may cause significant interference for amateur radio locators which could be argued to be unethical.

## 4.3 Radar Technology and Topology

It was decided that the most cost effective topology for the radar system was the active mono-static radar. Obtaining knowledge and data of the altitude of the detected space debris was seen of utmost importance in improving SSA and for this reason, a passive system would be inappropriate. Furthermore, the power density of stray EM radiation would be too low implying that the receiving array would require an exorbitant number of receiving antenna to maximize the gain to effectively detect and track targets. This would increase construction costs significantly. While implementation of an active radar would require an increased power consumption for operation, it allows for a more holistic solution in a sense that all aspects of the radar system are controlled by the users.

A mono-static topology was not only chosen for the purpose of minimizing the cost of implementation by requiring less land, but the complexity of the system would be reduced significantly. The signal processing component of the monostatic radar is simplified as no synchronization modulation schemes are required to determine range, but rather the time difference between signal transmission and echo reception would be necessary. In terms of illumination within the field of view, the mono-static radar requires the same phasing for both transmission and reception in a given direction whereas phasing for the transmitter and receiver in a bi-static radar is not same and is more complex.

Much like the PFISR, the system to be designed would take the form of square planar array for the

purpose of acquiring a symmetrical FOV that is more likely to detect and track space debris due to a wide angular extent in all directions. As is discussed in Section 4.8, the frequency range of interest spanning 26.918 kHz was considered to be the bandwidth  $B$ . The pulse width  $\tau$  of the system could be approximated as  $\tau = \frac{1}{B}$  and was found to be  $\tau=37\mu\text{s}$  [17]. Using the maximum range to detect debris, the Pulse Repetitive Frequency (PRF) was calculated to be 64.86 Hz [17].

#### 4.4 Single Array Element

The half-wave crossed dipole antenna was chosen as the element that would make up the phased array. The reasons behind this design choice included the fact that the half-wave crossed dipole antenna is capable of circular polarization and due to the fact it can be designed to have a broader band using wide diameter hollow pipes, ensuring a more uniform gain in a wider frequency range [18]. This allowed for the assumption that the gain would be the same across the frequency range of interest. The length of each dipole in the half-wave crossed dipole antenna was 30.62 cm ( $0.45\lambda$ ) for reasons that will be discussed in Section 4.7. The element was designed in CADFEKO such that one dipole was parallel to the x-axis and the other was parallel to the y-axis. The positive x-axis corresponds to  $\phi = 0^\circ$  and the positive y-axis corresponds to  $\phi = 90^\circ$ . Each dipole had a centre fed source with an impedance of  $50\ \Omega$  and had a vertical distance separation of 5 mm ( $\ll \lambda$ ). The source connected to the dipole parallel to the y-axis was phase shifted by  $90^\circ$  in relation to the source connected to the element parallel to the x-axis. Figure 1 and Figure 2 in Appendix B show the radiation pattern of the single half-wave crossed dipole that was left hand circularly (LHC) polarized at  $\phi = 0^\circ$  and  $\phi = 45^\circ$  phi cuts respectively.

Evidently, there is equal gain in both  $\theta = 0^\circ$  and  $\theta = 180^\circ$ . However, the polarization in the  $\theta = 180^\circ$  direction will be right hand circularly polarized (RHC). This energy is required to be directed in the opposite direction and the polarization needs to be LHC. This issue was rectified by making use of an infinite ground plane. Figure 3 and Figure 4 show the radiation patterns of the single element placed  $\frac{\lambda}{4}$  above the ground plane at  $\phi = 0^\circ$  and  $\phi = 45^\circ$  phi cuts respectively. The reflection brought about the ground plane not only corrects the polarization but also allows the EM waves that travelled in opposing directions to be added constructively, improving the gain in the  $\theta = 0^\circ$  direction.

#### 4.5 Optimizing Array Gain

The planar array was developed iteratively in CADFEKO. The changes per iteration consisted of manipulating the parameters of inter-element distance  $d$  as well as the height of the elements above the ground plane  $h$ . The effects of parameter manipulation were performed on a 20x20 array and each parameter was tested by keeping the other constant. The effects of decreasing  $h$ , where the initial value was 17 cm ( $\frac{\lambda}{4}$ ), resulted in increases in gain, decreases in HPBW and kept side lobe gain constant and the opposite was true when the  $h$  was increased. Decreasing  $d$ , from an initial value of 45 cm ( $0.66\lambda$ ), showed to decrease gain, increase HPBW and decrease side lobe gain and the opposite applied when  $d$  was increased. The desired radiation pattern for an array for the application of detecting space debris would be a maximised gain, minimized HPBW and minimized side lobe gain.

OPTFEKO was utilized for the purpose of executing a dual parameter optimization for the purpose of maximizing gain in the 20x20 array. The default Automatic optimization algorithm was used for this purpose. The ranges provided for optimization were 10-20 cm and 34-65 cm for  $h$  and  $d$  respectively. Given these input parameters, the optimization found that  $h=13.02$  cm and  $d=58.99$  cm were the optimum values required to maximise gain. Simulations were then performed whereby the number of elements per row were incremented in twos from 2-32 and the maximum gain in each case was recorded. Thereafter the data was fitted to provide the relationship in Figure 2. The radiation pattern of a 64x64 element array is shown by Figure 5 - Figure 7 in Appendix C.

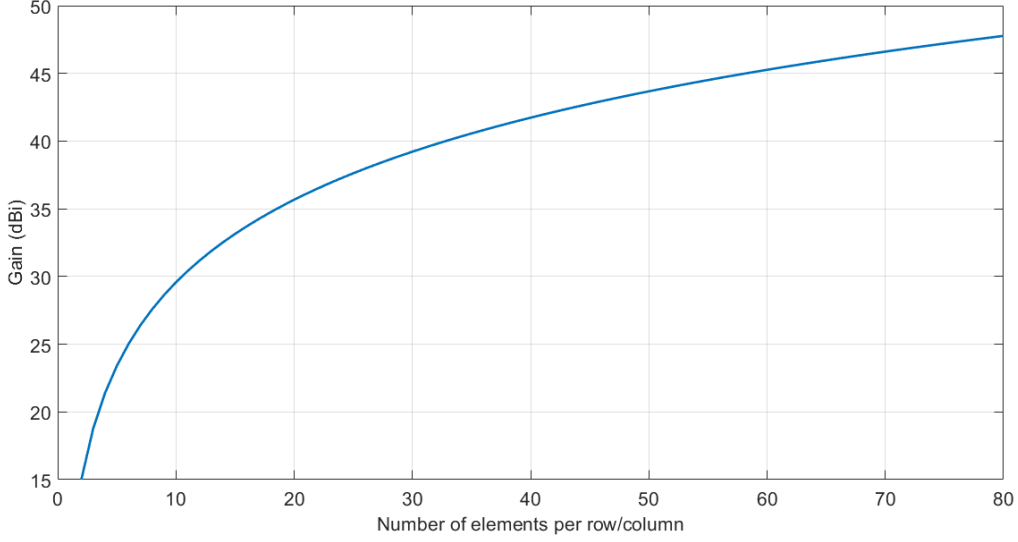


Figure 2: Relationship between number of elements per row/column and gain for optimal parameters.

The transitions in radiation pattern for  $\phi = 0^\circ - 90^\circ$  were the same for  $\phi = 90^\circ - 180^\circ$ ,  $\phi = 180^\circ - 270^\circ$  and  $\phi = 270^\circ - 0^\circ$ . Furthermore, the radiation patterns for  $\phi = 45^\circ, 135^\circ$  were the same and  $\phi = 0^\circ, 90^\circ$  were the same. Evidently, the size of the side lobes nearest to the main beam in the  $\phi = 0^\circ, 90^\circ$  directions were significant. If the radar was to detect a small object at maximum altitude in the  $\theta = 0^\circ$  direction and a large object was at a minimum altitude and in the side lobes direction, the chances of an ambiguous received echo would be increased. For this reason, these side lobes are required to be reduced. The approach used to minimize these side lobes is discussed in Section 4.6. The final and complete phased array took the form of a 76x76 planar array (5776 elements). Section 5 discusses the procedure undertaken to arrive at this specific number of elements under the consideration of a cost-performance optimization. Figure 8 - Figure 10 in Appendix C detail the radiation pattern of the final design of the phased array.

#### 4.6 Optimizing Side Lobes

A trade-off exists when maximising gain in an array with uniform distribution of power as it comes at the cost of increasingly dominant side lobes [8]. Several tapering approaches aid in reducing side-lobes at the cost of decreasing gain and increasing HPBW [8]. The three power distribution schemes that were investigated included the Binomial distribution, a Sinc function distribution obtained through an Invasive Weed Optimization (IWO) as well as the Gaussian distribution [8, 19]. The Binomial distribution was ineffective for array dimensions greater than 20x20 since the gradient of the applied taper was already too steep and resulted in the elements located toward the periphery of the array being supplied with insignificant power. While there were no side lobes, the gain could never be increased to the required level for detecting space debris with a reasonable peak transmit power. The Sinc function distribution had slightly inferior performance in relation to that of the Gaussian distribution as it required a steeper taper to provide the same effect as that of the Gaussian distribution.

The Gaussian distribution was investigated and implemented using the `imgaussfilt()` MATLAB function which was a 2-D filter used in image processing [20]. For the purpose of obtaining a normalized Gaussian distribution of a square matrix, a square matrix populated with ones was initialized and the filter was applied to it. Manipulating the filter size allowed for the ability to manipulate the gradient of the applied taper. The input arguments of the function were the initialized matrix and a numerical value that would determine the filter size. The optimal numerical value for the function was found to be  $0.3241n$ , where  $n$  is the number of elements per row/column of the phased array. This resulted in normalized range of matrix values of 0.1-1.0. Figure 3 shows sub-plots of the distribution

in row 1 and row 38 of the matrix. The procedure taken to determine the optimum corner element normalized power is discussed in Section 5. Furthermore, a heat-map representation of the normalized power distribution of the phased array can be found in Figure 11 in Appendix D.

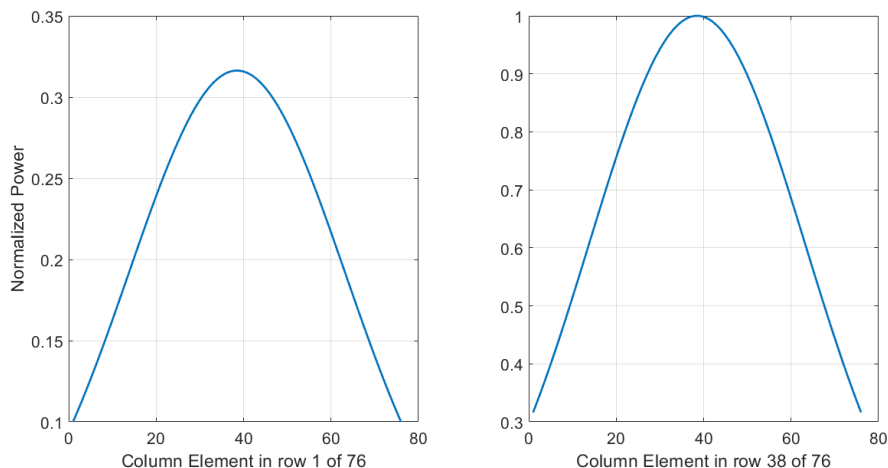


Figure 3: Power distribution of elements in the peripheral and centre row in the phased array.

#### 4.7 Matching

Matching antennas to their feeders is essential for the purpose of minimizing losses (maximum power transfer) as well as minimizing the Voltage Standing Wave Ratio (VSWR). While matching circuits could have been designed in the form of RLC and open/short stub circuits, this approach was expected to increase the cost of array construction due to the large number of elements (5776). The chosen approach was to find the correct length of each dipole in the half-wave crossed dipole element such that its input impedance would be as close to  $50\ \Omega$  as possible. The length of the dipole was initially  $\frac{\lambda}{2}$  in length and was shortened until the VSWR of the dipoles in the element was minimized. The minimized VSWR of each dipole was 1.12:1 and 1.18:1 at 440 MHz which was seen as acceptable for the application and the final length of each dipole was 30.62 cm ( $0.45\lambda$ ). The VSWR of each dipole in the element as a function of frequency can be seen in Figure 12 in Appendix E. The mismatch losses of each dipole as a function of frequency are shown in Figure 13 in Appendix E and are found to be -0.01 dB and -0.03 dB. Included in Appendix E are plots of the real and imaginary components of impedance for each dipole as a function of frequency in Figure 14 and Figure 15 respectively.

Since each element in the array is LHC polarized, the echo to be received after interacting normally with the target will still be circularly polarised but in the opposite direction, RHC. This implies that the phase shifter connected to the dipole parallel to the y-axis must be able to apply a phase delay of  $90^\circ$  when the phased array radar is transmitting and  $-90^\circ$  when receiving. At this stage, it is acknowledged that matching this stage of the system was not conducted and investigations into matching this stage of the system are recommended for future work. Therefore, it was assumed that the stage of the system between each transceiver and antenna element was matched.

#### 4.8 SNR and Debris

Several assumptions regarding the debris to be detected were made. The space debris that is to be detected will be assumed to be completely conductive. The reason behind this assumption is due to the fact that these objects are commonly fragments of man-made metallic structures. Furthermore, these objects are assumed to be spherical in shape. This assumption was made because currently existing literature use this assumption to evaluate the sensitivity of radar systems and a spherical shape will ensure a constant RCS of the object as it orbits around the Earth while rotating [1]. An

additional assumption made to simplify analysis was that debris orbited Earth at a constant speed of  $8 \text{ km.s}^{-1}$  [21]. Space debris having diameters of 10 cm or more, are approximated to make up to 95% of the space debris population [22]. Within the region below 1800 km, the distribution of space debris by altitude is non-uniform, with peaks around 900-1000 km and 1400-1500 km [22]. Furthermore, debris with diameters of approximately 10 cm have a higher spatial density at the altitude range of 500-1000 km [22].

With the above mentioned assumptions in mind, along with the assumption that the Earth is spherical with a radius of 6371 km, the range of radar to the target should not simply be modelled as the hypotenuse of a right-angled. The curvature of the Earth should be considered. This was seen as a valid modelling choice due to the fact that  $P_r$  is inversely proportional to the  $r^4$  and would therefore act as dominant term when performing a sensitivity analysis of the system. The derived equation detailing the relationships between these variables is detailed in Appendix F. Equation 8 should be substituted into Equation 1 to accurately analyse the sensitivity of the system.

Equation 2 can be used to determine the noise floor  $N_F$  (W) of the receiver of the radar system whereby  $k$  is Boltzmann's constant,  $B$  is the bandwidth of the receiver (Hz) and  $T$  is the noise temperature of the system ( $^{\circ}\text{K}$ ) [2].

$$N_F = kTB \quad (2)$$

The bandwidth of the receiver was determined by calculating double the maximum Doppler Shift expected from a centre frequency of 440 MHz and maximum FOV angle from array bore-sight. The value of  $B$  was found to be 26.918 kHz according to Equation 3 [17].  $f_d$  is the change in frequency due to the Doppler effect (Hz),  $v$  is the velocity of the target orbiting Earth ( $\text{m.s}^{-1}$ ) and  $\beta$  is the difference between  $90^{\circ}$  and the angle between the bore-sight of the phased array and the target. The Doppler shift is 0 Hz at boresight. The  $T$  term was estimated to be  $320^{\circ}\text{K}$ . The system  $N_F$  was therefore found to be -132.3 dBm ( $5.94 \times 10^{-17} \text{ W}$ ).

$$f_d = \pm \frac{2V \cos \beta}{\lambda} \quad (3)$$

The SNR of the received power from the target echo can be determined by the ratio of Equation 1 to Equation 2. A typical radar system operates with a detection probability of 0.9 and a probability of false alarm of  $10^{-6}$ . According to [23] the required signal to noise ratio can be read off the SNR vs probability of detection graph as 13.2dB. It should be noted that this requirement is for a single pulse of a steady sinusoidal signal in Gaussian noise with negligible detection losses [23]. Furthermore, the minimum SNR required for a probability of detection of 0.9 is possible with an SNR of 7 dB. This however comes at the cost of probability of false alarm of 0.1 [23].

#### 4.9 Feeding Network

The corporate feed is one of the most commonly utilized feeding network topologies that are used in passive (no beam shifting) antenna arrays [24]. As a standalone topology, the corporate feed is not suitable for the designed array that will require active phasing and beam steering. For this reason, a distributed feed (an active form of corporate feed) should be implemented whereby each element in the array is connected to its own transceiver module [17]. Each transceiver module will consist of a digitally controlled phase shifter, digitally controlled attenuator, solid state power amplifier as well as a low noise amplifier [17]. A distributed feed may be utilized to supply each transceiver module with the 440 MHz tone that is to be amplified and variable gains can be applied to each element in the array depending on its position. Figure 16 in Appendix E shows the approach to design the distributed feed for the application. An important aspect of the feeding network is that of the losses. There is a loss in input signal power level as it travels from the transmitter to the antenna, through the coaxial cable as well as devices such as a circulator that are normally incorporated within the transceiver module.

In order to match each stage of the feed network to  $50 \Omega$ ,  $\frac{\lambda}{4}$  transformers may be implemented using



Equation 4. The required characteristic impedance  $Z_o$  to make the input impedance  $Z_{in}$  and output impedance  $Z_{out}$  of the  $\frac{\lambda}{4}$  transformer be equal to 100  $\Omega$  and 50  $\Omega$  respectively, was found to be 70  $\Omega$ . In this way each stage of the feeding network joint to two 100  $\Omega$  input impedances in parallel, will be 50  $\Omega$  yet again. Figure 16 in Appendix E visually depicts the scenario. In this way, mismatch losses in the feed network are minimized.

$$Z_o = \sqrt{Z_{in}Z_{out}} \quad (4)$$

In the latter stages of the design process it was found that a distributed feed network that divided power in each stage by 2 would not be possible for an array of 5776 elements as this was not a square number. Therefore, it has been acknowledged that further investigation into a suitable topology for the phased array radar should be conducted. For the purpose of acquiring a loss factor of the feed network, a loss of 3 dB was selected as this was the order of loss for most conventional radar systems [17].

#### 4.10 Phasing Network

Each element in the array could be phased individually through the digital control of the transceiver module. The development of the phasing network would only involve determining the progressive phase delays required between each element in the array to steer a main beam in a specified  $\phi$  and  $\theta$  direction within the FOV of the designed radar system. It has been assumed that the progressive phase delays required to steer a beam in specific directions have been pre-programmed and are controlled digitally. Equation 5 and Equation 6 provide the progressive phase delay required, for element rows/columns parallel to the x-axis and y-axis respectively ( $\psi_x$  and  $\psi_y$ ), to steer the main beam in a specific  $\phi$  and  $\theta$  direction [25, 26].

$$\psi_x = \frac{2\pi d_x}{\lambda}(\sin\theta\cos\phi) \quad (5)$$

$$\psi_y = \frac{2\pi d_y}{\lambda}(\sin\theta\sin\phi) \quad (6)$$

The variables  $d_x$  and  $d_y$  represent the inter-element spacing of elements parallel to the x-axis and y-axis respectively while  $\phi$  and  $\theta$  represent the direction which the beam should be steered to. In order to acquire the required phase delay for each element in the array, the following procedure was followed. Once the values of  $\psi_x$  and  $\psi_y$  were determined, two  $n \times n$  matrices were constructed in MATLAB to represent the phasing along the x-axis and the y-axis. One matrix was constructed by populating each row of the matrix with an increasing scalar multiple of  $\psi_x$  and the other matrix was constructed by populating each column of the matrix with an increasing scalar multiple of  $\psi_y$ . These matrices were summed to acquire the relative phase required for each element which could be imported to CADFEKO. The radiation patterns of the phased array when the main beam is steered in different directions may be found in Appendix H.

#### 4.11 System Location

The desert regions of South Africa provide highly favourable operating conditions for the high and medium frequency arrays that will be essential for the operation of the Square Kilometre Array (SKA) [27]. A major reason of the preference in these desert areas is due to a minimal population implying radio frequency interference from mobile phones, TVs and radios and other electrical devices are also minimized [27]. Other criteria that were considered when choosing an appropriate location for the SKA included the characteristics of the ionosphere, climate and subsurface temperatures, connectivity to worldwide communication for distribution of acquired data as well as infrastructure costs including power supply [27].

The SKA site is located approximately in the centre of a rectangle formed by four major towns namely Carnarvon to the SE, Vanwyksvlei to the NE, Williston to the SW and Brandvlei to the NW. There

are several areas within this rectangle that will be suitable for the operating conditions of the designed phased array radar [28]. The selection of a location of implementation of the designed system should be conducted within this area. An area within this rectangle should be selected so that the terrain is flat, placed far way from nearby towns (up to 100 km) yet be reasonably close to transport infrastructure for the sake of ease in transport of materials required for construction [28]. Furthermore, since the MEERKAT and HERA are also in close proximity to the SKA site ( $< 1$  km), it can be assumed that there is sufficient infrastructure for power supply as well as data connection infrastructure that can be developed further [27, 28]. One of the major concerns of choosing a location for implementation in this area is that echoes from target detection will interfere with that of the SKA measurements since it has a frequency bandwidth of 350 MHz - 14 GHz [29].

In order to ethically design, construct and operate the device at or near this location, a partnership with the SKA would have to be arranged such that inference with SKA measurements are minimized and in order to allow the SKA to benefit from data acquired from the designed system. Additionally, the SKA is under the protection of the Astronomy Geographic Advantage (AGA) Act of 2007 which is legislation which gives the Minister of Science and Technology the power to protect areas through regulations to preserve and develop areas suited to astrological research [30]. These regulations include the Land Acquisition Process (LAP) which details the procedures in interacting with the nearby communities and populations and will be discussed further in the Non-Technical report in Appendix A [31]. By forming a partnership with the SKA, an appropriate location that will benefit both the space debris detecting phased array and the SKA could be arranged.

## 5. OPTIMIZATION

A cost-performance optimization was performed through consideration of environmental effects in terms of the required power to operate the system. Since LEOLABS's PFISR has a peak transmit power of 2 MW, a design decision was made to develop a system with a peak transmit power of 1 MW for the purpose of minimizing environmental impacts, minimizing stress on South Africa's power distribution infrastructure and maximizing the sustainability and longevity of the system [13]. The average power of the system can be determined from the product of the peak transmit power, PRF and  $\tau$  and was calculated to be 2.4 kW [17]. Based on the transmission losses discussed in Section 4.9, the peak input transmit power and average input transmit power required to operate the system would be 2 MW and 4.8 kW respectively. This lower power solution of design has consequences of the phased array radar requiring an increased number of elements to achieve similar functionality to the LEOLABS solution. The transmit/receive modules are the most expensive component of the electrical portion of the phased array radar and the quantity of these items are directly related to the number of elements in the array. Therefore minimizing the number of elements in the array while achieving full functionality was seen to optimize the cost.

Figure 18 in Appendix G shows a flow diagram of the algorithm used to arrive at the cost-performance optimized number of elements. The algorithm takes the effects of adding/subtracting an additional row and column of elements as well as changing the taper of the power distribution of the array into account. Through numerous iterations of the algorithm, the optimal number of elements required to detect a spherical object with a radius of 5 cm located at an altitude of 1800 km in bore sight direction was 5776 ( $76 \times 76$ ). In bore sight direction and in a  $\phi=0^\circ$  cut, the difference in gain between the main beam and the largest side lobe was 28.829 dBi as shown in Figure 8 and normalized power of the corner elements of the array were found to be 0.1 after application of a Gaussian distribution. These numbers of elements in conjunction with the non-uniform power distribution resulted in a maximum gain of 46.5368 dBi and a HPBW of  $0.832^\circ$ . Based on the fact that the peak transmit power would be 1 MW, the Gaussian distribution resulted in the elements at the centre of the array transmitting peak powers of 350 W and the others were scaled accordingly.

## 6. CRITICAL ANALYSIS

### 6.1 Environmental Impact

Based on the values obtained for the required input peak and average powers for transmission, the environmental impact due to power requirements was minimized. Other environmental impacts are highlighted in Appendix A.

### 6.2 Performance

A sensitivity analysis was conducted to determine the ability of the designed system to detect spherical, perfectly conducting space debris of different radii that are at different orbit altitudes. The phased array displayed a decrease in main beam gain as the beam steering was directed further away from the the bore sight of the array. This phenomenon was analysed in the  $\phi=0^\circ$  and  $\phi=45^\circ$  directions. An additional effect of beam steering was the occurrence of significant side lobes in the directions other than the desired one. The consequence of having more than one dominant beam in the radiation pattern when steering is that ambiguities in target detections may occur. In the case that one target is in the path of the steered beam and another is in the path of a dominant side lobe, the system would be able to detect two separate echoes if the radar range to each target was not the same but would not be able to distinguish the direction from which each echo originated from. Figure 8 as well as Figure 19 to Figure 23 show the effects of steering the main beam on the radiation pattern in the  $\phi=0^\circ$  cut. Figure 9 as well as Figure 24 to Figure 30 show the effects of steering the main beam on the radiation pattern in the  $\phi=45^\circ$  cut.

The systems capabilities of detecting space debris would be feasible for altitudes whereby a perfectly conducting spherical object with a radius of 5 cm could be detected with an SNR of 7 dB or greater. Furthermore, the sensitivity of the dominant side lobes occurring when steering the beam is required to be less than the sensitivity of the steered beam while meeting the previously mentioned specification. The sensitivity analysis was conducted by utilizing the ratio of Equation 1 to Equation 2 to determine the SNR of the system when detecting spherical debris with radii  $r=2.5$  cm,  $r=5$  cm,  $r=7.5$  cm,  $r=10$  cm and  $r=1$  m at altitudes ranging from 200-1800 km. 0 dB in the sensitivity analysis represented the noise floor of the system. It should be noted that the considerations of debris altitude, Earth curvature, beam steering direction and range mentioned in Section 4.8 were considered. This allowed for the sensitivity of the system to be analysed in terms of altitude of different sized debris when steering at different angles.

When the beam is steered towards bore-sight, the sensitivity of the main beam is at its maximum and the system is capable of detecting a sphere with a radius of 5 cm at an altitude of approximately 1800 km. The sensitivity of the side lobe in this case ( $\theta=\pm 2.99^\circ$ ) is significantly less than that of the main lobe such that debris with radii as large as 10 m could not be detected at altitudes as low as 200 km. While the sensitivity of the system steered in this direction is impressive, it should be noted that no Doppler shift will be detectable since the radial component of the velocity of debris travelling in the bore-sight path is zero. Therefore, at the steering position of  $\phi=0^\circ$ ,  $\theta=0^\circ$ , knowledge of the objects velocity and whether it is travelling toward or away from the bore-sight is unknown. Only range and altitude information may be determined in this position. Figure 31 and Figure 32 in Appendix H show the sensitivity analysis of the system when steered to bore-sight.

As the beam is steered further away from bore-sight, the sensitivity of the main beam is decreased while that of the side lobe is increased. This relationship can be investigated through inspection of Figure 33 to Figure 40 in Appendix H. When the system is steered to  $\phi=0^\circ$ ,  $\theta=25^\circ$  the sensitivity of the side lobe ( $\phi=0^\circ$ ,  $\theta=-47^\circ$ ) is comparable to that of the steered main beam. Therefore, the FOV was limited to the  $\theta=\pm 25^\circ$  in the  $\phi=0^\circ$  and  $\phi=90^\circ$  directions. Within this FOV, the system would be able to detect debris with a radius of 5 cm or more at altitudes no higher than 1100 km. Objects

having radii  $\geq 7$  cm could be detected at 1800 km altitudes.

An analysis was also performed in the  $\phi=45^\circ$  direction. The sensitivity of the main beam steered to bore-sight is same as that of the previous bore-sight case, but the sensitivity of the most dominant side lobe ( $\phi=45^\circ$ ,  $\theta=\pm 2.3^\circ$ ) was even more insensitive to the main beam. A sensitivity analysis plot of this case was not included because it was seen as redundant and would not assist in finding the limitation of the FOV in the  $\phi=45^\circ$  direction. The relationship of a decreasing sensitivity of the main lobe and increasing sensitivity of relevant side lobes when steering in the  $\phi=45^\circ$  direction can be found in Figure 43 to Figure 56 in Appendix H. When the system is steered to  $\phi=45^\circ$ ,  $\theta=35^\circ$ , the resulting side lobes ( $\phi=152^\circ$ ,  $\theta=58.5^\circ$  and  $\phi=118^\circ$ ,  $\theta=-58.5^\circ$ ) become comparable to that of the main lobe as seen in Figure 55 and Figure 56 in Appendix H. Therefore, the FOV in the  $\phi=45^\circ$  and  $\phi=135^\circ$  directions is limited to  $\theta=\pm 35^\circ$ . The sensitivity of the system within the FOV in these directions would allow for the system to be able to detect objects with a radius of 5 cm at altitudes up to approximately 1000 km. Objects having radii  $\geq 7$  cm could be detected at 1800 km altitudes.

An additional characteristic of the steered main beam as it is steered away from the bore-sight is the fact that the HPBW increases. This increase in HPBW would lead to a decreasing resolution as the beam is steered away from the bore sight. The properties of the designed phased array radar are summarized in Table 1 in Appendix H.

According to the theory on the debris distribution density with respect to altitude mentioned in 4.8, the system was able to detect and have an increased probability of tracking debris in the altitudes of major concern. Therefore the design was seen to be successful and feasible solution to the problem of detecting space debris.

### 6.3 Cost Breakdown

A cost analysis of the construction of the phased array radar system was conducted. The total cost to implement the system was estimated to be R 664 795 697.90. The reasons and justifications for the pricing of all components of the cost analysis are included in Appendix I. Table 2 in Appendix I summarizes the cost analysis. While the estimated cost certainly does appear to be exorbitant, it should be noted that the system is for scientific research purposes and would most likely receive government funding. Furthermore, since the system addresses the issue of improving SSA, major organizations in the space industry would contribute to the development of the system as it serves as a means to preserve and protect current as well as future space infrastructure. Therefore, the implementation of the system does appear to be feasible and sustainable.

## 7. DISCUSSION

### 7.1 Trade-offs

Several trade-offs existed throughout the design of the system. The decision to reduce the required peak transmit power required to detect debris effectively to minimize the environmental impact had the consequence of increasing the cost to construct the phased array system. Nonetheless, it was seen as the appropriate decision when considering the long term operation of the system as the running costs are significantly less, making the design a more sustainable one.

Another trade-off situation was encountered when deciding on the type of FOV best suited for detecting space debris. When viewed from above toward array bore-sight direction, a symmetrical FOV normally provides a narrower range in terms of angular extent but due to symmetry, there is an equal chance of detection and tracking of debris travelling in all directions. A non-symmetrical FOV, usually created using a long rectangular planar array or reflector-based array, had a much larger angular extent in one direction and a much smaller on in the other. Although a symmetrical FOV was selected in this

design, once more information of the trends and most common directions travelled by debris is known, a non-symmetrical FOV may be favourable and will be cheaper to implement as significantly less radiating elements will be required.

As is the case in all engineering designs, there is a trade-off between the cost of the design and the quality of the solution. In order to develop a system with minimal losses and maximum performance, higher quality solid-state power amplifiers and co-axial cables as well as larger numbers of radiating elements and increased power requirements would be needed, increasing cost. A cheap solution is always possible at the expense of a decreased system performance. This highlights the need for a cost-performance optimization to find the intersection between acceptable performance and feasible cost.

## 7.2 Future Work

While the designed system displays traits that make it feasible for the detection and tracking of space debris, future work is necessary to improve the system further. As mentioned in Section 4.9, there was a shortcoming in the system design with the respect to the design of an appropriate feed network. A thorough design and simulation of a distributed feed providing each transceiver device with the transmitter tone should be conducted. In an attempt to operate in a partnership with the SKA, the system should be designed at frequencies below the lower bound of the SKA frequency band while taking the National radio frequency plan into consideration.

When optimizing the inter-element spacing and height above the ground plane for the purpose of maximising gain, the effect of changes of these parameters on the the side-lobes of the radiation pattern should be considered and optimally minimized. This will allow the effect of the non-uniform distribution of power to all radiating elements to be improved in terms of side lobe reduction. Additionally, a variable power distribution to array elements should be investigated. By manipulating the power distribution depending on the direction the system is being steered to, not only will the occurrence of side lobes in undesirable directions be minimized but the gain of the main beam steered in the desired direction will be increased.

Finally, the design process may be developed further through the considerations of the signal processing as well as data transfer and storage components of the system.

## 8. CONCLUSION

The design and analysis of a phased array radar system for the purpose of detecting and tracking space debris was conducted. The system was designed as a monostatic radar using a  $76 \times 76$  planar array of half-wave crossed dipoles to detect perfectly conducting and spherical space debris with radii as small as 5 cm. The major design choices were highlighted and justified. Additionally, the development of the array is discussed in detail in terms of how adverse features of the radiation patterns were addressed. A critical analysis of the system found that the sensitivity of the system decreased as the main beam was steered away from bore-sight. Furthermore, the supply power required for system operation was seen to be feasible and sustainable. A cost-performance optimization was performed for the purpose of finding the intersection between acceptable performance in detecting space debris and low cost. The estimated cost to construct phased array with components that were viewed as important in the functioning of the radar was R 664 795 697.90. The signal processing, power and data transfer infrastructure required for the device were not included in the cost analysis and hence a full implementation is expected to cost significantly more than the estimated value. Trade-offs encountered in the design were acknowledged and the future work for the purpose of improving and developing the system further were recommended.

## REFERENCES

- [1] S. J. Tingay, D. L. Kaplan, B. McKinley, F. Briggs, R. B. Wayth, N. Hurley-Walker, J. Kennewell, et al. "On the Detection and Tracking of Space Debris Using the Murchison Widefield Array. I. Simulations and Test Observations Demonstrate Feasibility." *The Astronomical Journal* 146, , no. 4, September 2013.
- [2] G. Muntoni et al. "Space Debris Detection in Low Earth Orbit with the Sardinia Radio Telescope." *Electronics*, August 2017.
- [3] Z. Guang and Z. Jing-Rui. "Space Tether Net System for Debris Capture and Removal." *4th International Conference on Intelligent Human-Machine Systems and Cybernetics*, 2012.
- [4] IEEE Standard Radar Definitions, std-686-1990.
- [5] R. Bansal. *Handobook of Engineering Electromagnetics*. Marcel Dekker Inc, 2004. Pages:377-414.
- [6] M. Nicolls et al. "Conjuction Assessment for Commercial Satellite Constellations using Commercial Radar Data Sources." *Advanced Maui Optical and Space Surveillance Technologies Conference (AMOS)*, 2017.
- [7] J. G. Trujillo, S. Halte, M. S. Perez, and P. Besso. "On the Design of a Planar Phased Array Radar Antenna Architecture for Space Debris Situational Awareness." *7th European Conference on Antennas and Propagation (EuCAP)*, 2013.
- [8] J. D. Kraus. *Electromagnetics*. McGraw-Hill Book Company, 3rd ed., 1984. Pages: 640-653.
- [9] "The Earth's Ionosphere." URL <http://solar-center.stanford.edu/SID/activities/ionosphere.html>. Last accessed: 23 September 2018.
- [10] C. J. R. Capela. "Protocol of Communications for VORSAT Satellite." *Universidade do Porto*, 2012.
- [11] G. R. Curry. *Radar Essentials - A Concise Handbook for Radar Design and Performance Analysis*. SciTech Publishing, 2012. Pages: 69-78.
- [12] "LEOLABS Data Platform." URL <https://platform.leolabs.space/>. Last accessed: 11 October 2018.
- [13] T. Valentic et al. "AMISR The Advanced Modular Incoherent Scatter Radar." *Center for GeoSpace Studies, SRI International*, 20013.
- [14] P. Shrestha, A. Maharjan, and H. Kapadia. "Radio Aurora Explorer Nano-Satellite Radar: Data Inversion." *Worcester Polytechnic Institute*, 2009.
- [15] M. J. Nicolls. "Space Debris Measurements using the Advanced Modular Incoherent Scatter Radar." *SRI International, Center for Geospace Studies*, 2008.
- [16] *National Radio Frequency Plan*. Independent Communications Authority of South Africa (ICASA), 2018.
- [17] M. A. Richards, J. A. Scheer, and W. A. Holm. "Principles of Modern Radar." *SciTech Publishing*, 2010. Pages:273-303.
- [18] A. Kiraga. "On performance of cylindrical dipole antenna in diagnostics of wave phenomena in space plasma." *34th COSPAR Scientific Assembly, The Second World Space Congress, held 10-19 October, 2002 in Houston, TX, USA., meeting abstract, id.1910*, 2002.
- [19] G. Sun, A. Wang, et al. "An Antenna Array Sidelobe Level Reduction Approach through Invasive Weed Optimization." *International Journal of Antennas and Propagation*, 2018.
- [20] "MathWorks Documentation." URL <https://www.mathworks.com/help/images/ref/imgaussfilt.html>. Last accessed: 3 October 2018.
- [21] E. Gregersen. "Space debris." *Encyclopaedia Britannica*, 2018.
- [22] National Research Council. 1995. Orbital Debris: A Technical Assessment. Washington, DC: The National Academies Press. <https://doi.org/10.17226/4765>. Pages: 63-77.
- [23] G. Brooker. *Sensors and Signals*. Australian Centre for Field Robotics, University of Sydney, 2007. Pages: 283-302.
- [24] T. A. Milligan. *Modern Antenna Design*. A John Wiley and Sons Incorporated Publication, 2005. Pages: 573-604.
- [25] H. H. Cher. "Two-Way Pattern Design for Distributed Subarray Antennas." *Naval Post Graduate*

*School*, 2012. Pages:1-13.

- [26] S. Patole and M. Torlak. "Two Dimensional Array Imaging with Beam Steered Data." *Dept. of Electrical Engineering, University of Texas, Dallas*, 2014.
- [27] "The Location Of The SKA." URL <https://www.skatelescope.org/location/>. Last accessed: 16 October 2018.
- [28] "Google Maps, SKA Radio Telescope." URL <https://www.google.com/maps/place/SKA+Radio+Telescope/@-30.5263856,20.7582003,228067m/data=!3m1!1e3!4m5!3m4!1s0x1c293d69580cbac7:0x1453ca2eb3278983!8m2!3d-30.7216391!4d21.4110768>. Last accessed: 18 October 2018.
- [29] P. J. Hall et al. "The Square Kilometre Array (SKA) Radio Telescope: Progress and Technical Directions." *Radio Science Bulletin*, 2008.
- [30] "Astronomy Geographic Advantage Act." URL <http://www.ska.ac.za/about/astronomy-geographic-advantage-act/>. Last accessed: 15 October 2018.
- [31] "Land Acquisition Process." URL <http://www.ska.ac.za/about/land-acquisitions/>. Last accessed: 16 October 2018.
- [32] "Mini-circuits RF and Microwave Components and Systems." URL <https://www.minicircuits.com/>. Last accessed: 20 October 2018.
- [33] "RS Components." URL <https://za.rs-online.com/web/c/abrasives-engineering-materials/aluminium-tubes-sheets-angles/aluminium-tubes/>. Last accessed: 20 October 2018.
- [34] "Guideline for Services and Processes for Estimating Fees for Persons Registered in Terms of the Engineering Profession Act, 2000, (Act No. 46 of 2000)." *Engineering council of South Africa*, 2013.
- [35] Alaris Antennas Senior Design Engineer, Personal Communication, 2018.

## **Appendix**

### **A Non-Technical Report**

#### **INTRODUCTION**

The design of a phased array radar system for the purpose of detecting and tracking low earth orbiting space debris is essential for maintaining the functionality of current space infrastructure. There are, however, different manners in which the design and development of such a system would have environmental, social as well as economic impacts. Impacts and considerations in these areas are discussed and highlighted.

#### **ENVIRONMENTAL IMPACTS AND CONSIDERATIONS**

The construction as well as operation of the phased array radar for the detection and tracking of space debris will have certain impacts on the environment within the vicinity. Since the construction of the radar will be land-based, a small area within the selected location for implementation will require minor excavation for the purposes of construction preparations. This implies that all vegetation and small animals within this area will be effected. In order to minimize this effect, a largely open area of land situated far from nearby towns and populations was selected. Further, within this land, the area chosen for system implementation was the one with the least dense population of vegetation and would be inspected for any signs or evidence of animal life before commencement of system implementation could be approved.

Due to the nature of the architecture of the design, birds in the area may view the structure as a suitable place to land on. If this occurs while the system is in operation, the bird will experience discomfort in the form of increased heating. To reduce cases of this scenario, bird reflectors should be installed and allow them to land in a safer area.

For this application, the radiated electromagnetic power is directed towards the sky to detect and track space debris. This implies that there will be interactions between the radiated power of the phased array and anything in its path directed into space. Structures that might interact with the radiated power include aeroplanes if flight plans involve flying over the array. In order to prevent these interactions, the system should be operated in conjunction with civil aviation flight plans. By positioning the phased array radar far from populated areas as well as designing it to minimize the horizontal electromagnetic radiation, the interactions of radiation with human beings is minimized.

All components used in the implementation of the system are compliant with the Restriction of Hazardous Substances (RoHS). This implies that health and safety of the surrounding environment will not be compromised by the use and operation of the electrical components via the leakage of harmful chemicals or substances in the specified operating conditions. Furthermore, the approach of the design was directed towards creating a solution that required less supplied power for the sake of environmental considerations. An increased required power supply would result in coal power stations having to utilize more coal per unit time, hence increasing the rate of emitted CO<sub>2</sub> into the Earth's atmosphere which should be minimized at all times.

#### **SOCIO-ECONOMIC IMPACTS AND CONSIDERATIONS**

The impacts and considerations of the designed system were taken in the context of the current South African economic position, situation and population. Due to the expected exorbitant cost of the implementation of the system, certain aspects affecting the sourcing of required components need to be discussed. The necessary components are required to be of high quality to ensure a design that is capable of acceptable performance for the application. Local Radio Frequency retailers do not



offer the required components and hence these need to be imported. South Africa's current economic situation is such that the ZAR is significantly weaker than the USD making the cost of the project increasingly expensive at this time.

Depending on the source of funding for the project, different impacts may occur. If the designed system is to be government funded, members of society, particularly those who pay taxes and are receiving insufficient service delivery from government, will feel a sense of social stigmatization towards the project. In recent years and in extreme cases, effected members of society have taken action by causing damage to property as means of expressing anger. While this scenario may not occur, it is seen as a social issue that is required to be highlighted. In the case where the project requires additional land through the SKA's Land Acquisition Process, all procedures must be conducted as stipulated in the Astronomy Geographic Advantage Act of 2007. This would involve extensive informative interactions with affected parties on upcoming developments as well as negotiations with individual property owners. Land may only be acquired once the owner of the property accepts the terms.

In a more realistic case, implementing the system as a privately funded project would reduce financial strain on the South African government. Furthermore, since the system would be aimed at improving Space Situational Awareness (SSA) to protect future and current international space infrastructure, multiple leading organisations in the space industry would contribute to development of the project to utilize the services provided by the system. This may, in turn, attract foreign investors and offer the opportunity for the South African economic situation to be improved.

In both funding cases, different type of job opportunities will be created. Contract work opportunities will be created through the hiring of manual labourers for the purposes of installing and fitting the components required for the construction. Furthermore, contract or full time jobs would be created for the purpose of inspecting that the system is in optimal operational conditions as well as maintaining and monitoring the system. Job opportunities requiring higher skill levels will take the form analysts of acquired data and communicating findings with the major space industry organisations.

## **CONCLUSION**

The environmental as well as socio-economic impacts of the design and development of a phased array radar for space debris detection are discussed. It is evident that the design process has taken the inevitable and potential environmental impacts into account and provided amelioration for these impacts. The same can be said for the addressing of socio-economic impacts. This was done through a depiction of different socio-economic cases.

## B Single Element Radiation Patterns

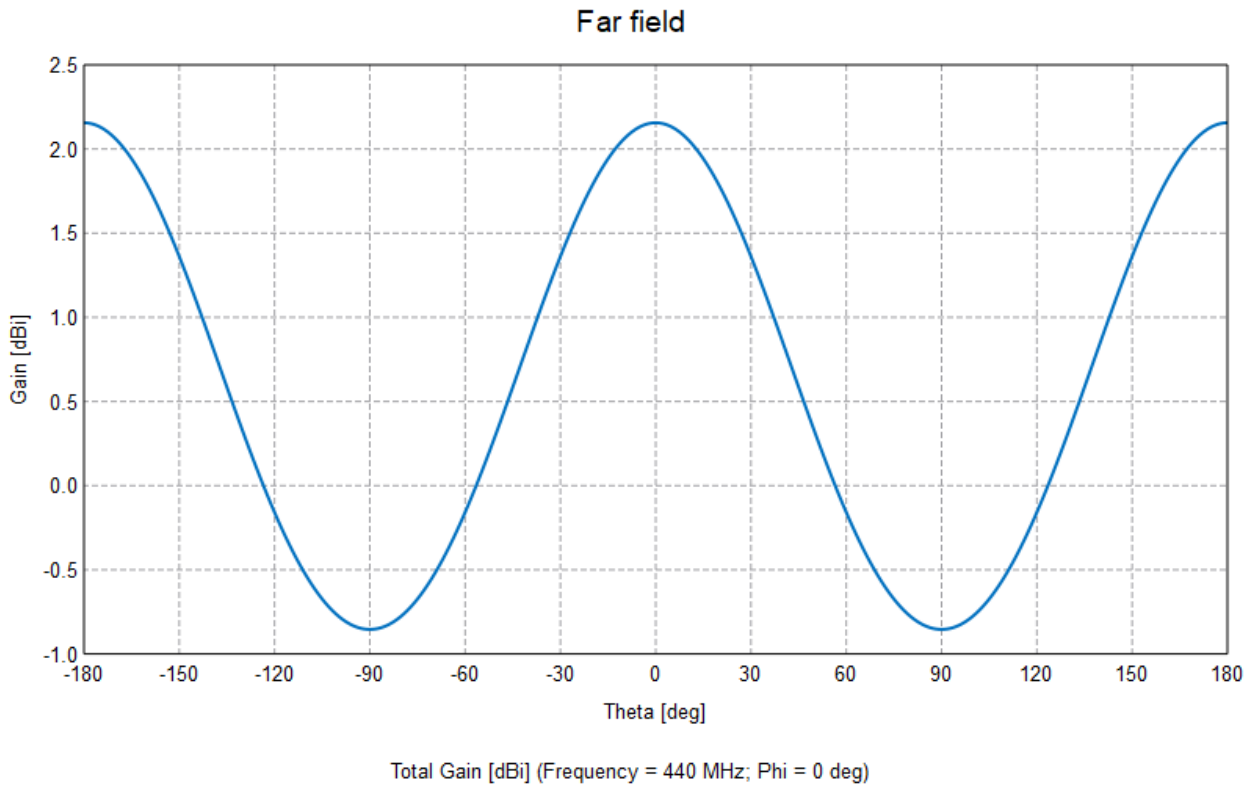


Figure 1: Radiation pattern of a single half-wave crossed dipole antenna cut through  $\phi = 0^\circ$ .

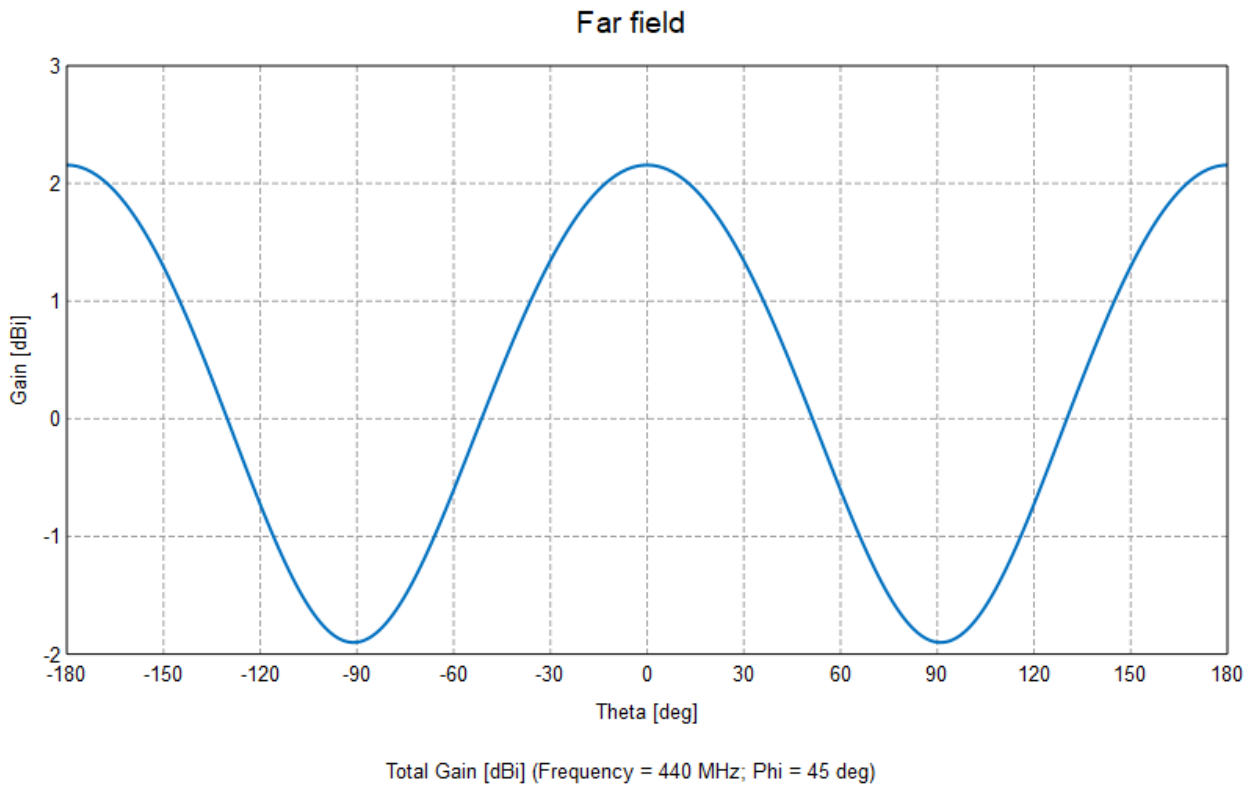


Figure 2: Radiation pattern of a single half-wave crossed dipole antenna cut through  $\phi = 45^\circ$ .

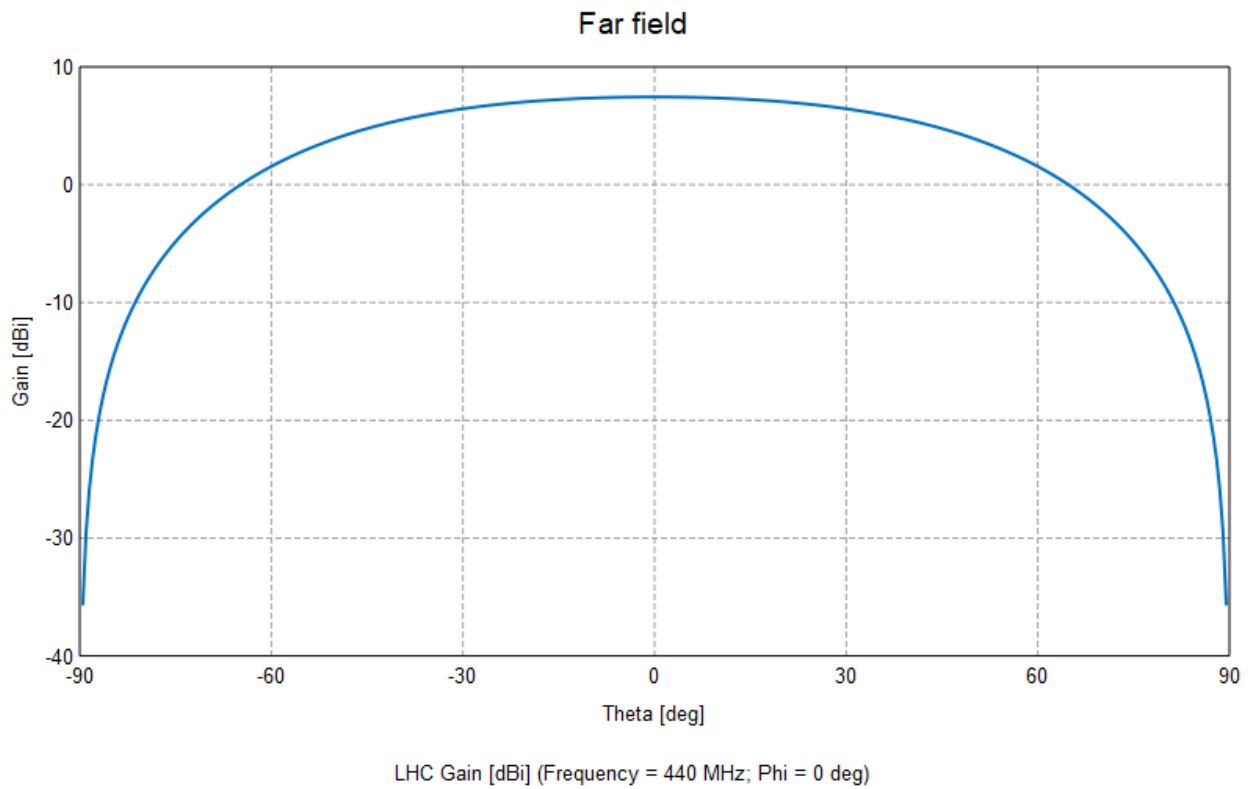


Figure 3: Radiation pattern of a single half-wave crossed dipole antenna placed  $\frac{\lambda}{4}$  above an infinite ground plane cut through  $\phi = 0^\circ$ .

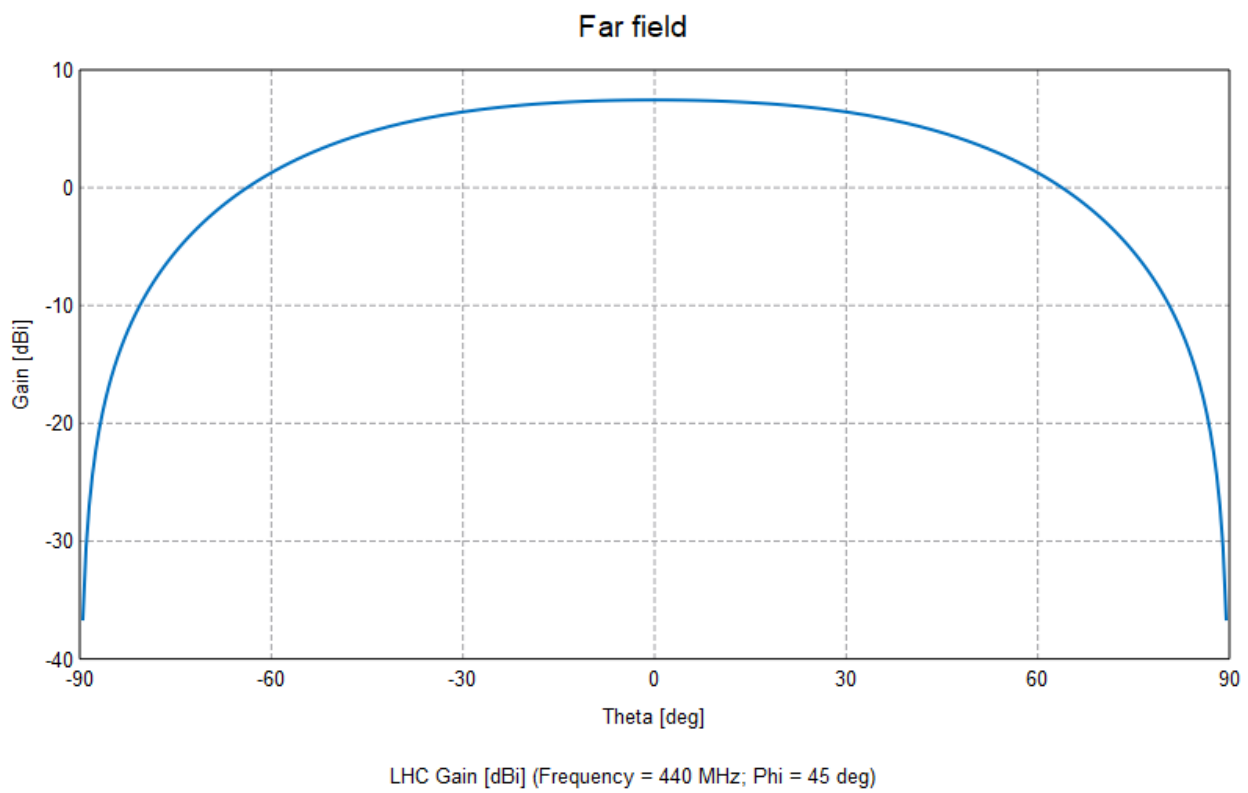


Figure 4: Radiation pattern of a single half-wave crossed dipole antenna placed  $\frac{\lambda}{4}$  above an infinite ground plane cut through  $\phi = 45^\circ$ .

## C Array Radiation Patterns

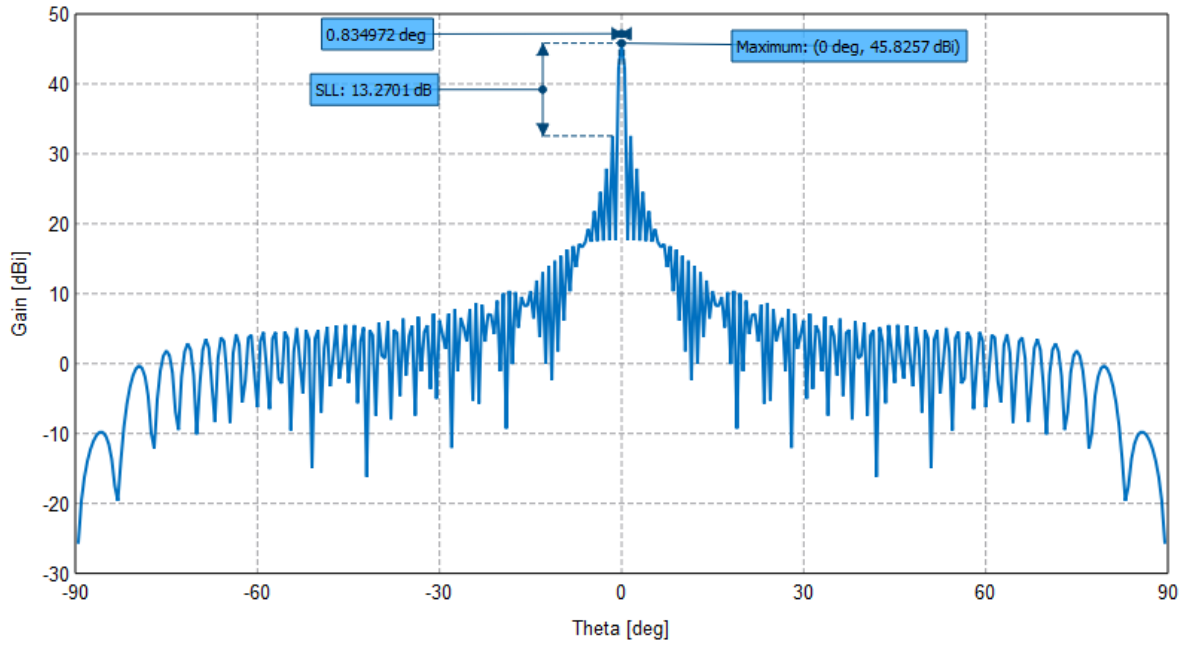


Figure 5: Radiation pattern of a 64x64 array with optimal  $d$  and  $h$  values and uniform distribution through a  $\phi = 0^\circ$  cut.

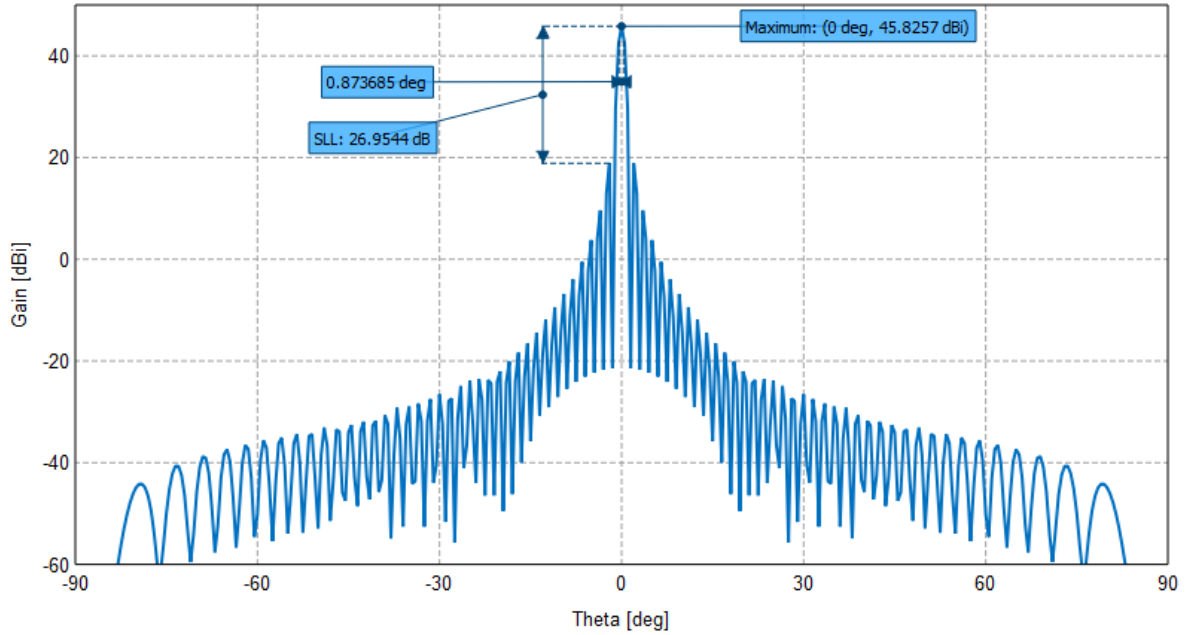


Figure 6: Radiation pattern of a 64x64 array with optimal  $d$  and  $h$  values and uniform distribution through a  $\phi = 45^\circ$  cut.

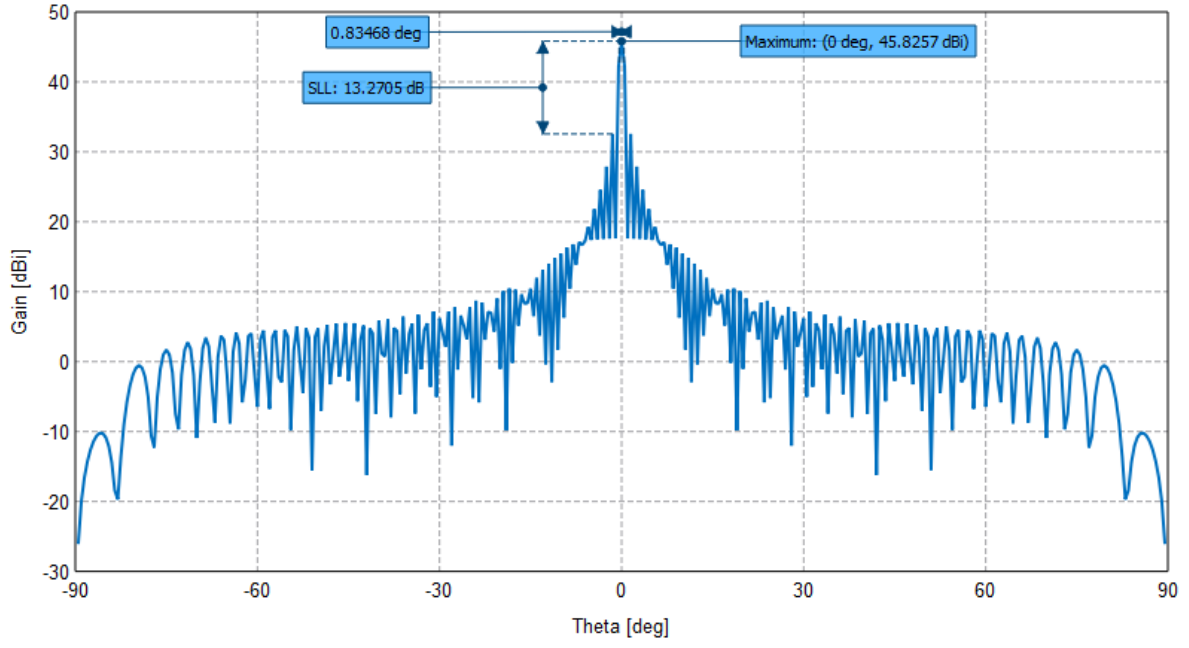


Figure 7: Radiation pattern of a 64x64 array with optimal  $d$  and  $h$  values and uniform distribution through a  $\phi = 90^\circ$  cut.

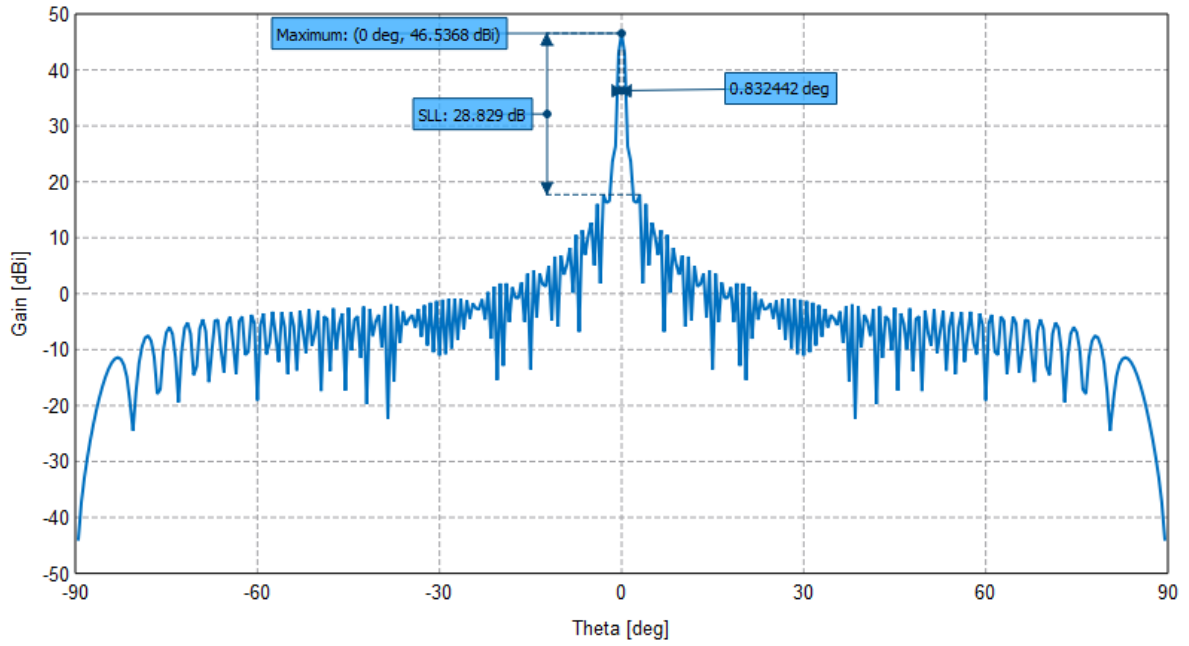


Figure 8: Radiation pattern of the final 76x76 array with non-uniform distribution  $\phi = 0^\circ$  cut.

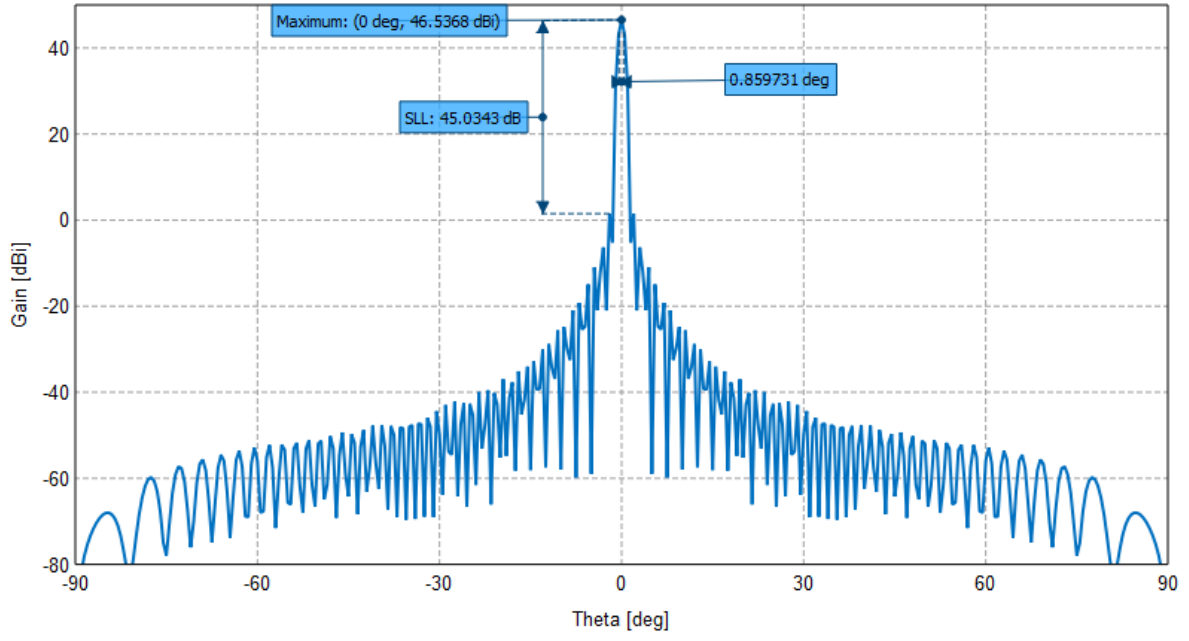


Figure 9: Radiation pattern of the final 76x76 array with non-uniform distribution  $\phi = 45^\circ$  cut.

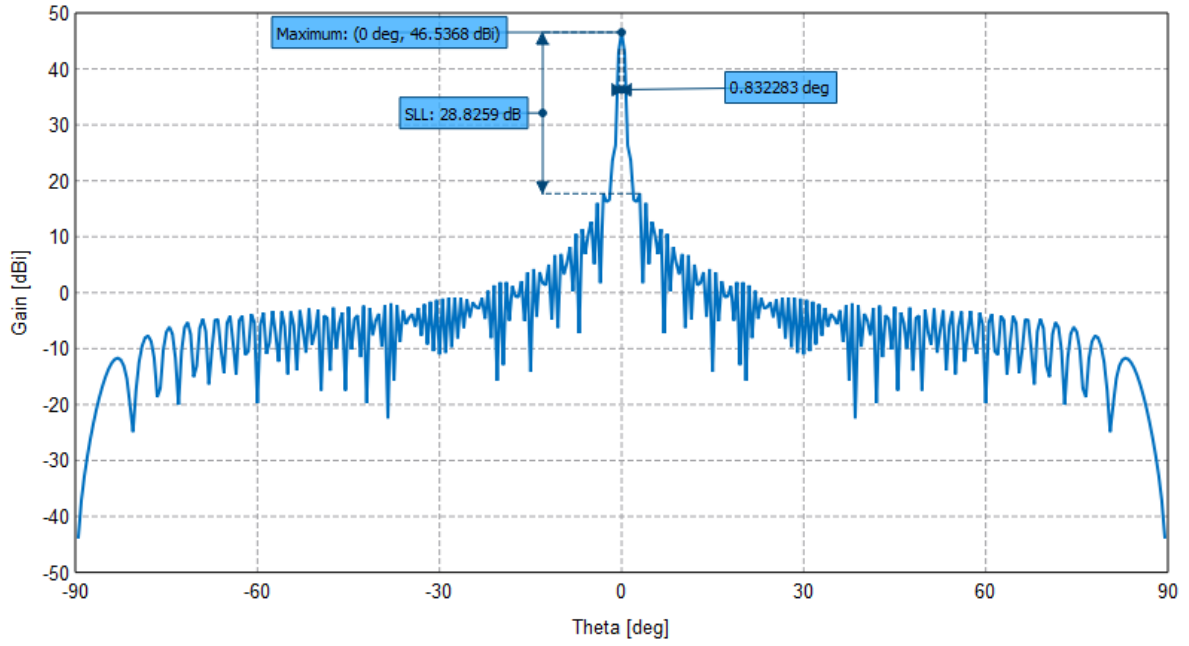


Figure 10: Radiation pattern of the final 76x76 array with non-uniform distribution  $\phi = 90^\circ$  cut.

## D Power Distribution

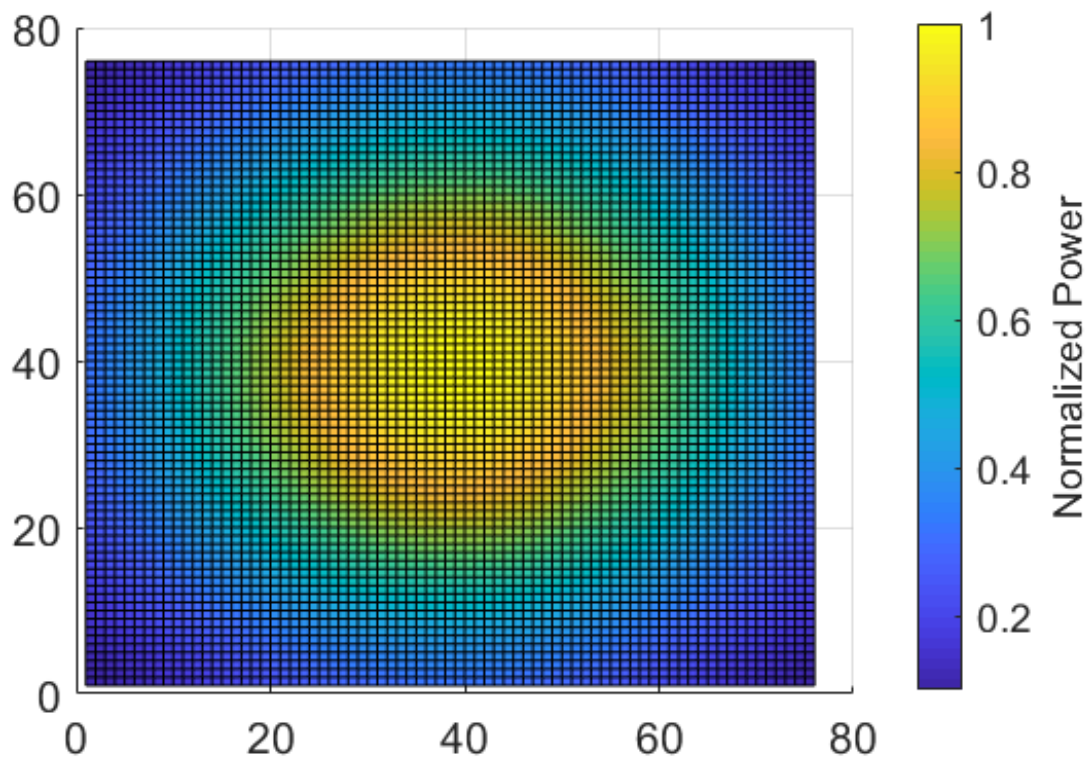


Figure 11: Heat-map representation of the power distribution of the 76x76 planar phased array.

## E Antenna and Feeding Network Matching

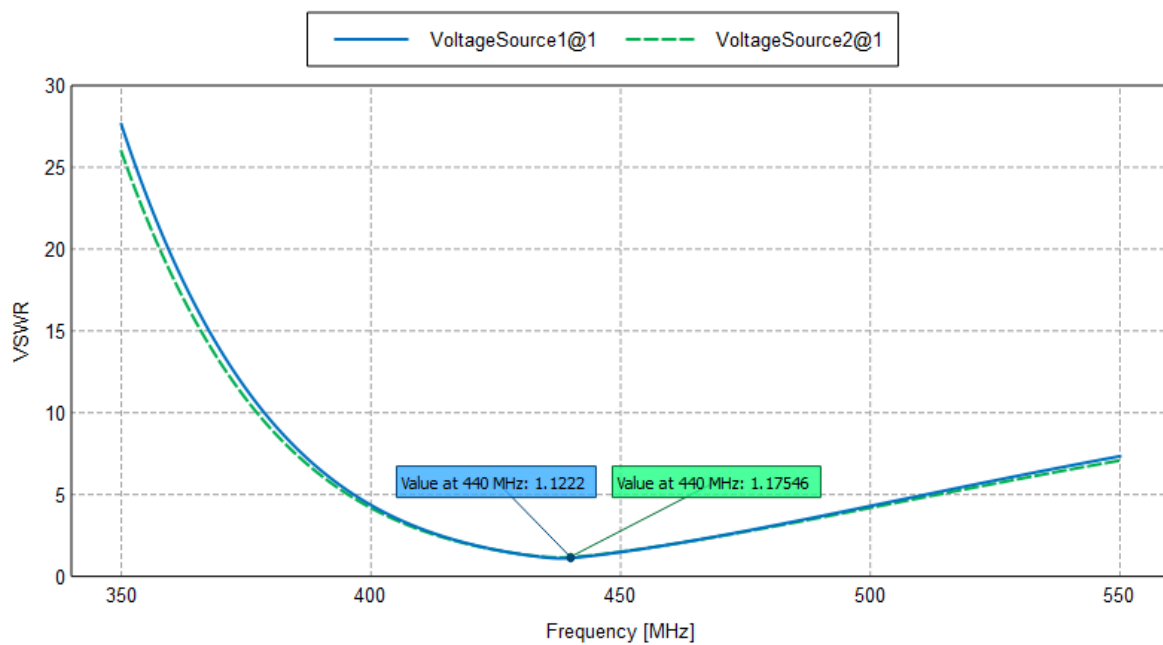


Figure 12: VSWR of each dipole in the half wave crossed dipole when matched to a 50  $\Omega$  source.

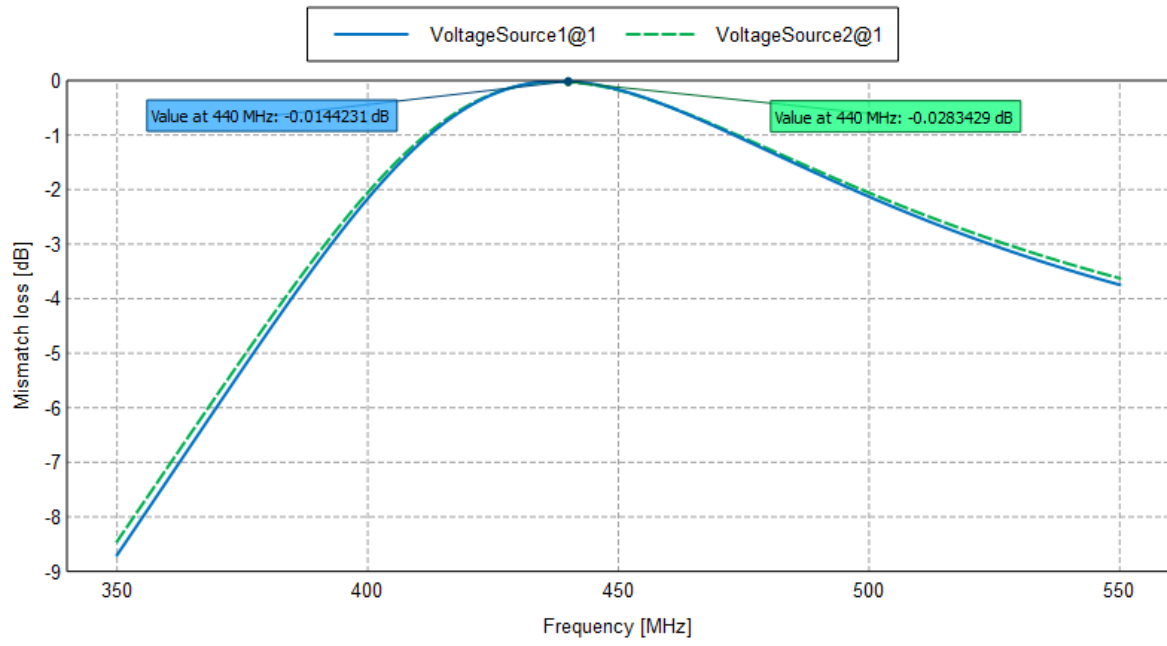


Figure 13: Mismatch loss of each dipole in the half-wave crossed dipole element.

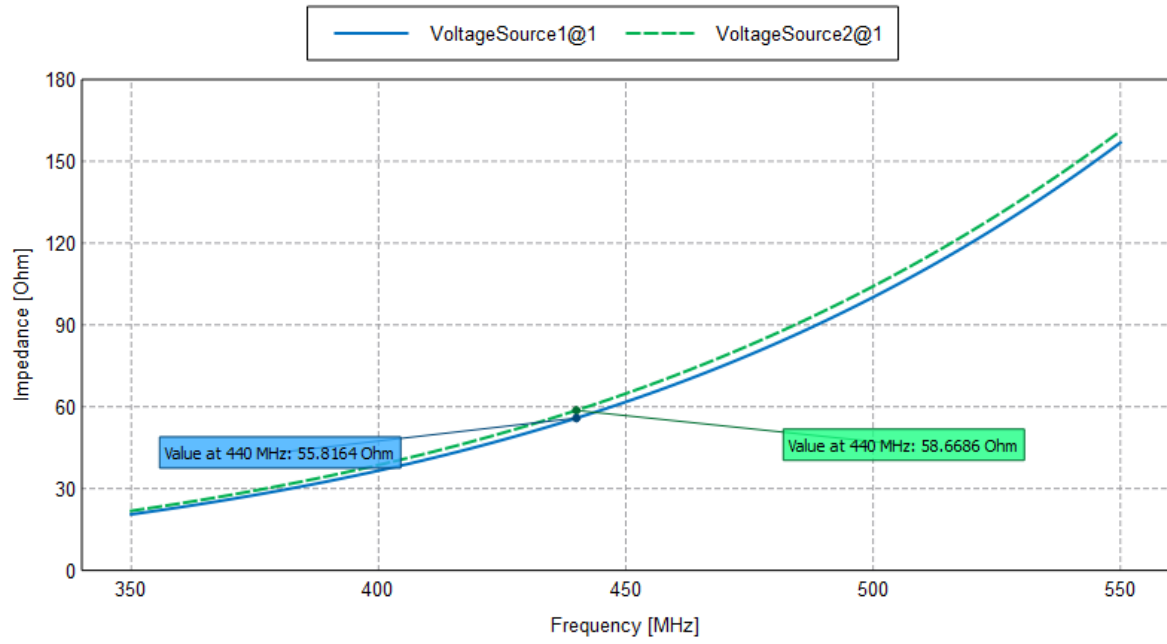


Figure 14: The real component of impedance for each dipole in the half-wave crossed dipole element.



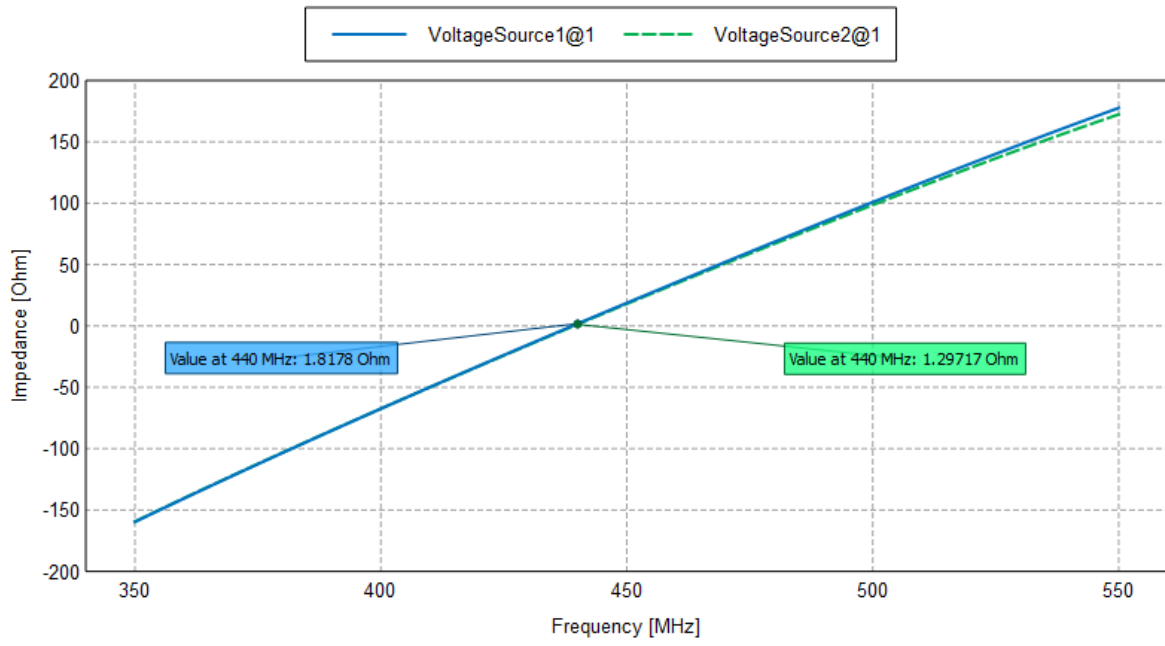


Figure 15: The imaginary component of impedance for each dipole in the half-wave crossed dipole element.

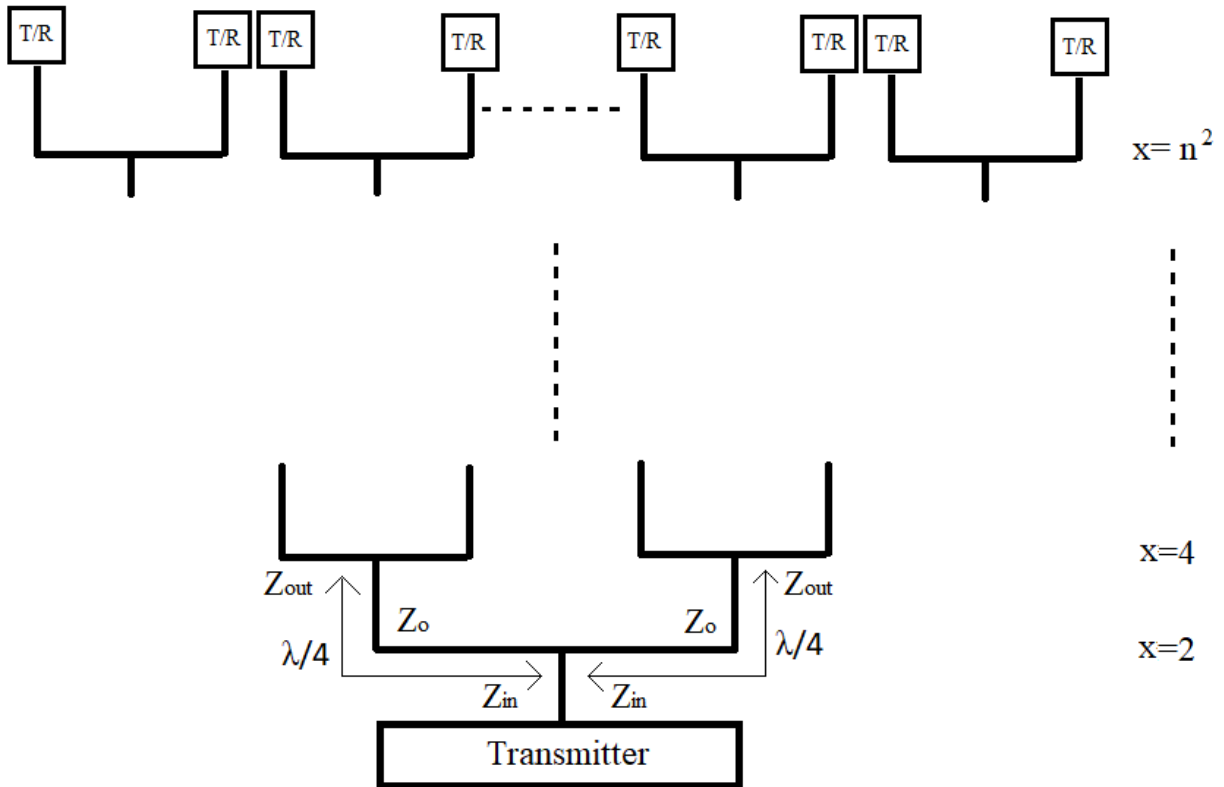


Figure 16: Visual representation of distributed feed network matching.

## F Debris Orbit Altitude-Range Model

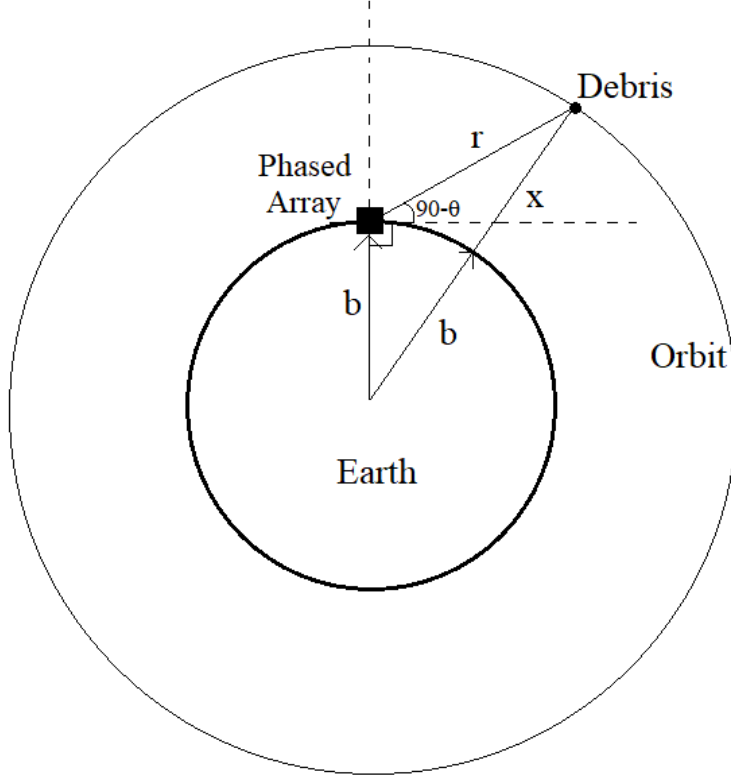


Figure 17: Visual representation of the relationship between debris altitude and radar range.

$$c^2 = r^2 + b^2 - 2rb\cos(180 - \theta) \quad (7)$$

Equation 7 is a relationship describing the Law of Cosines. In the the context of detecting space debris at different altitudes and beam steering directions,  $c$  represents the sum of the radius of a spherical Earth  $b$  (6371 km) and a specified debris altitude  $x$ .  $r$  is the radar range to the target debris and  $\theta$  symbolizes the angle from the phased array to the target debris with respect to the bore sight of the array. Essentially,  $\theta$  would also correspond to the desired  $\theta$  direction of beam steering. Equation 7 should then be manipulated using the quadratic formula such that  $r$  becomes a function of  $\theta$  and debris altitude to the surface of the Earth  $x$ . Equation 8 shows this relation where only the positive solution is valid.

$$r = \frac{2b\cos(180 - \theta) \pm \sqrt{(2b\cos(180 - \theta))^2 - 4(b^2 - (b + x)^2)}}{2} \quad (8)$$

## G Cost-Performance Optimization Algorithm

In the process of optimizing the number of elements required to achieve desirable functionality, it is evident that only two variables required manipulation, namely  $n$  the number of rows/columns required in the array (or number of elements per row/column) as well as the normalized power  $P_n$  of the elements in each corner of the array. The manipulation of  $P_n$  was performed indirectly by changing the filter size of the Gaussian filter applied to a matrix in MATLAB. Decreasing the filter size would result in an increase in the gradient of the taper and a decrease in the value of  $P_n$  while the opposite applied for increasing the filter size. The minimum normalized power value was set be 0.05 as any value lower than this was seen to be too close to zero. Essentially, if the normalized power was found to be lower than 0.05, the elements in the corner could be removed without having a significant effect

on the performance of the phased array. An optimal difference in main beam gain  $G_{main}$  and side lobe  $G_{SL}$  of between 25 dB and 30 dB when the system was steered towards bore sight was selected. The reason behind this range selection is that it allowed for debris with radii much greater than 5 cm to be in the path of the side lobe without causing ambiguity if a target with a radius of 5 cm was in the bore sight path and located 1800 km away.

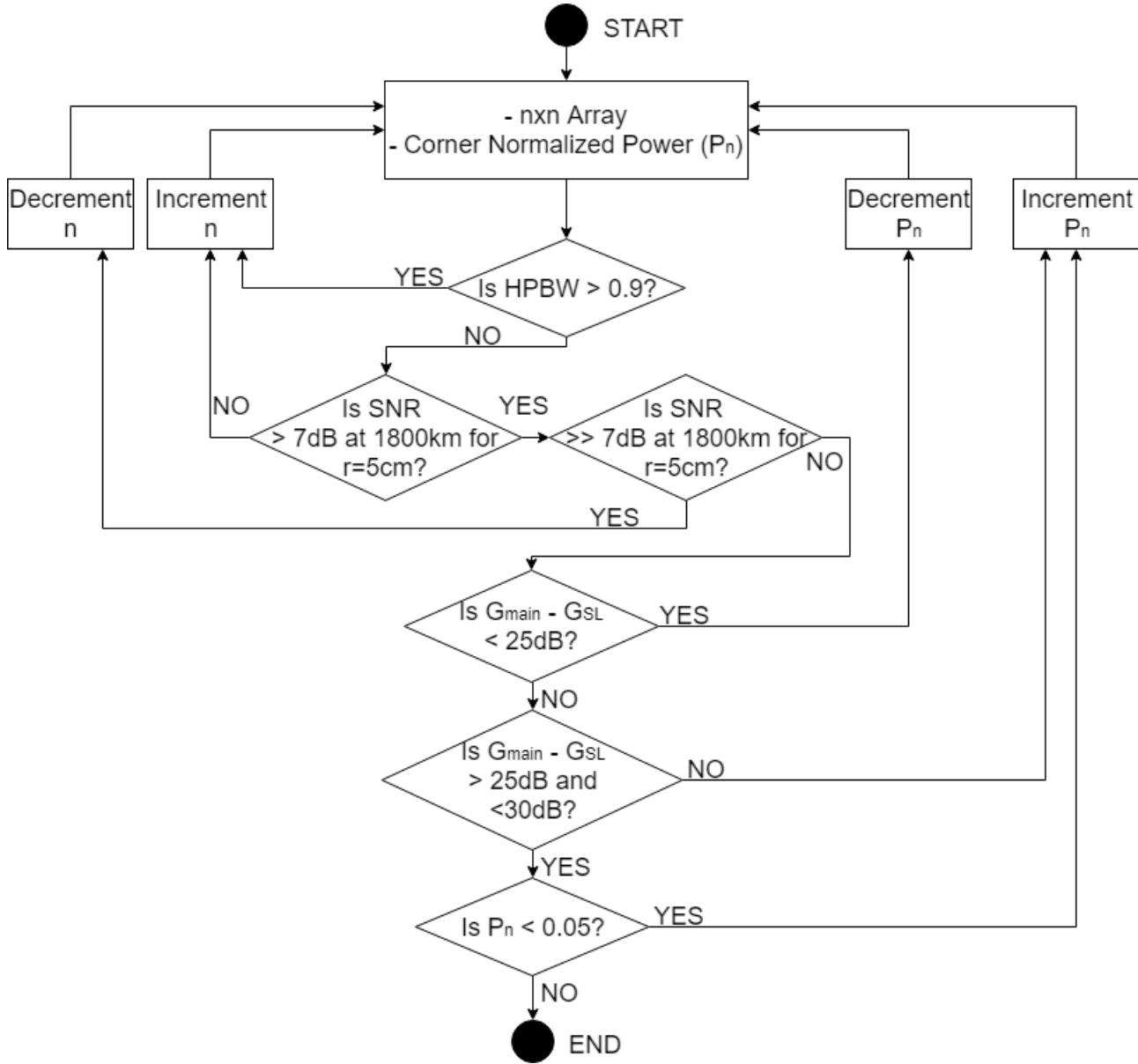


Figure 18: Flow diagram of the algorithm used in determining the optimal number of elements per row/column in the  $n \times n$  phased array.

## H Sensitivity Analysis and Steering

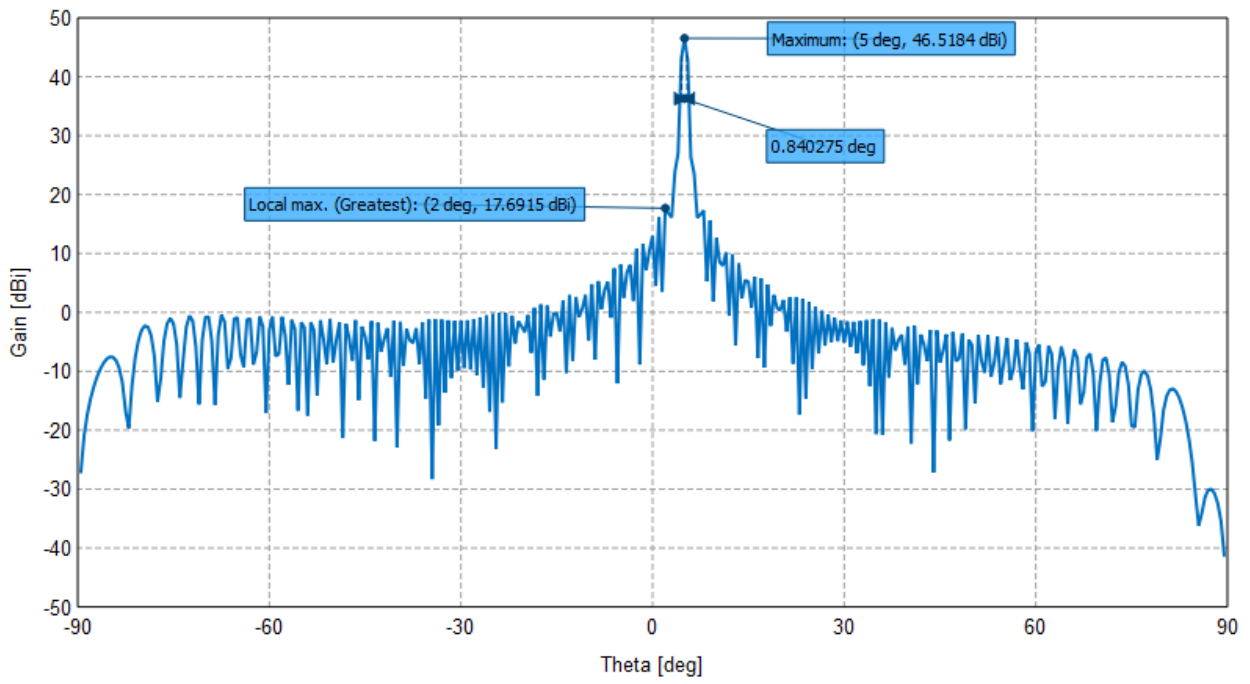


Figure 19: Resulting radiation pattern when system is steered to  $\phi=0^\circ$ ,  $\theta=5^\circ$ .

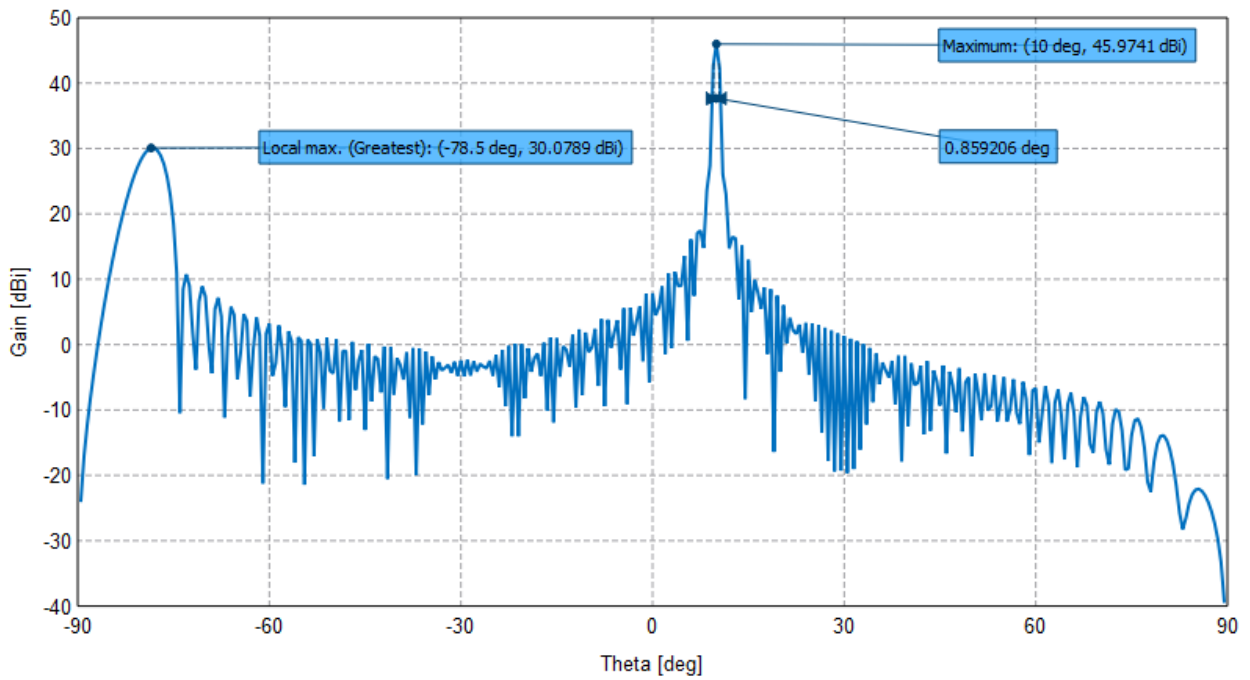


Figure 20: Resulting radiation pattern when system is steered to  $\phi=0^\circ$ ,  $\theta=10^\circ$ .

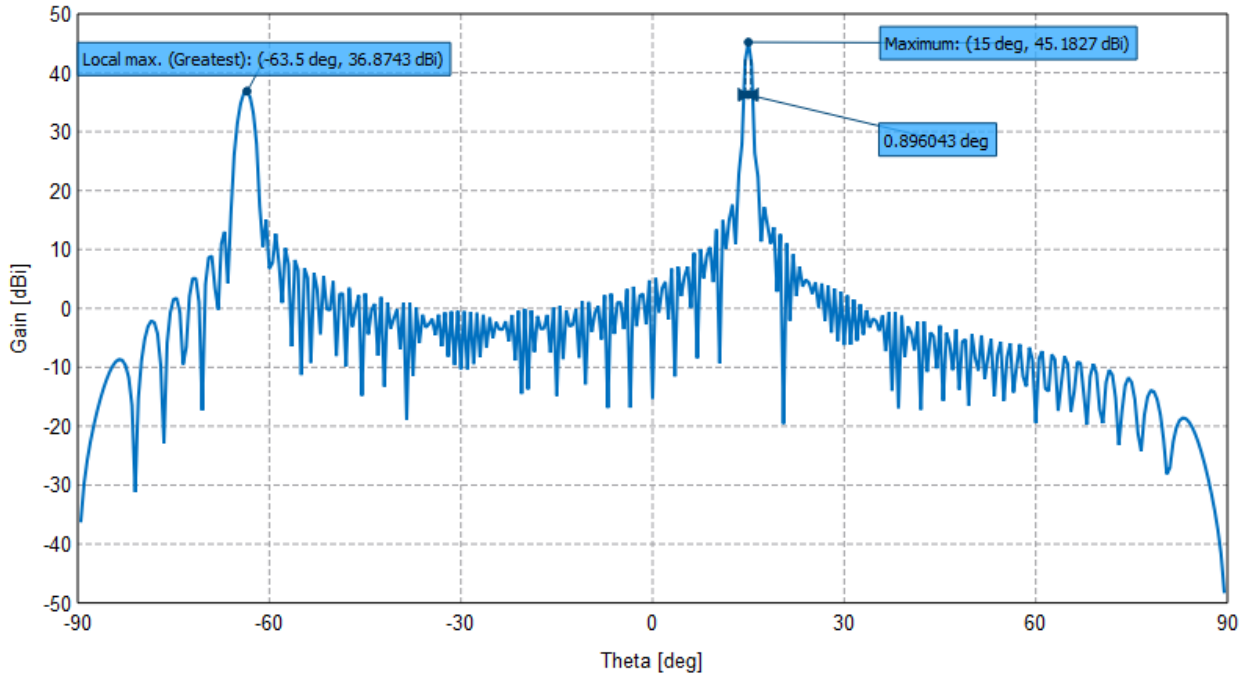


Figure 21: Resulting radiation pattern when system is steered to  $\phi=0^\circ$ ,  $\theta=15^\circ$ .

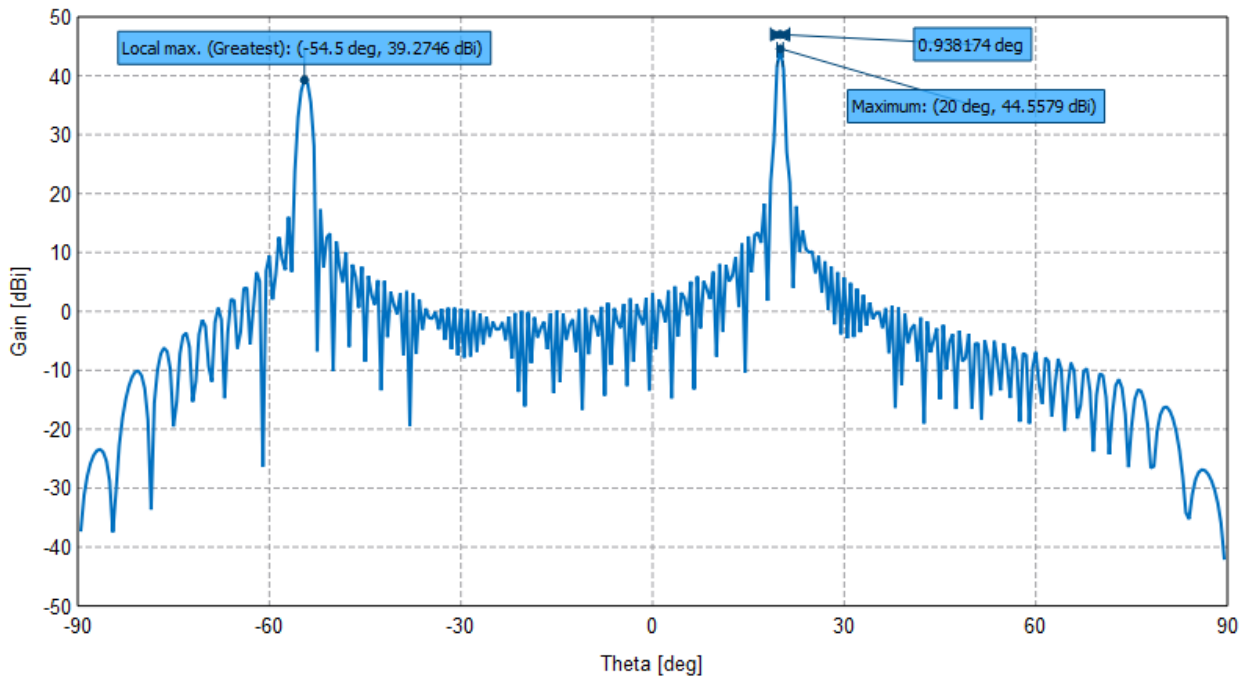


Figure 22: Resulting radiation pattern when system is steered to  $\phi=0^\circ$ ,  $\theta=20^\circ$ .

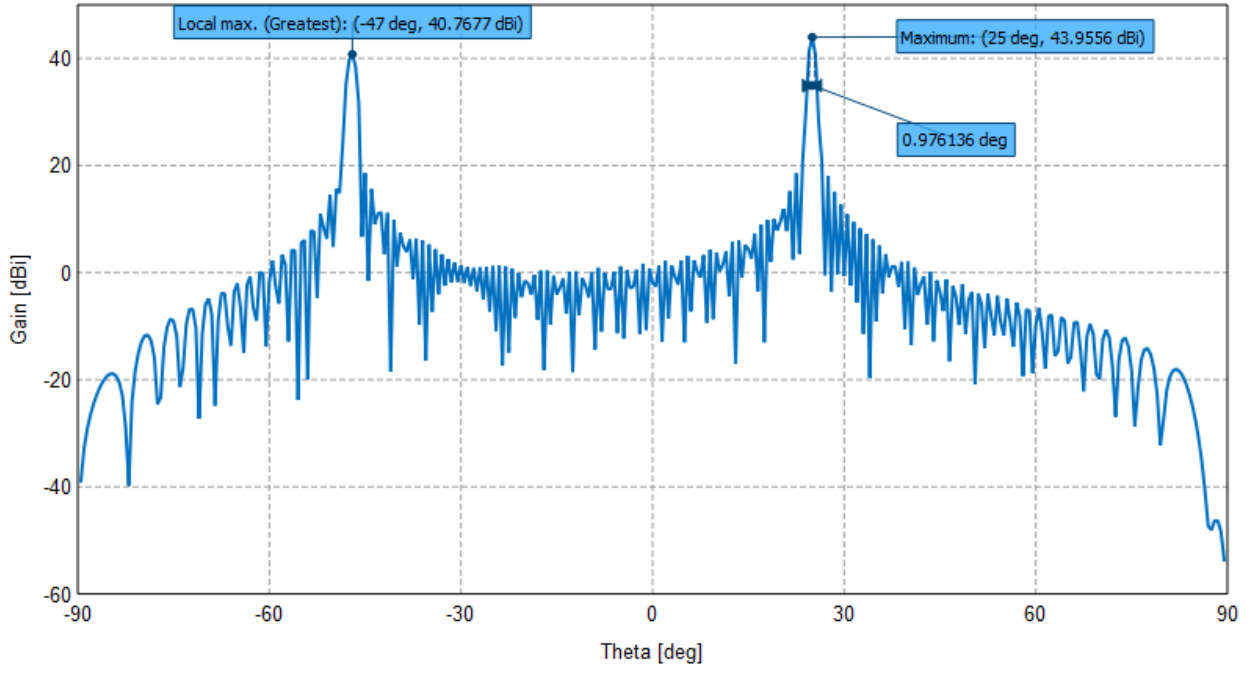


Figure 23: Resulting radiation pattern when system is steered to  $\phi=0^\circ$ ,  $\theta=25^\circ$ .

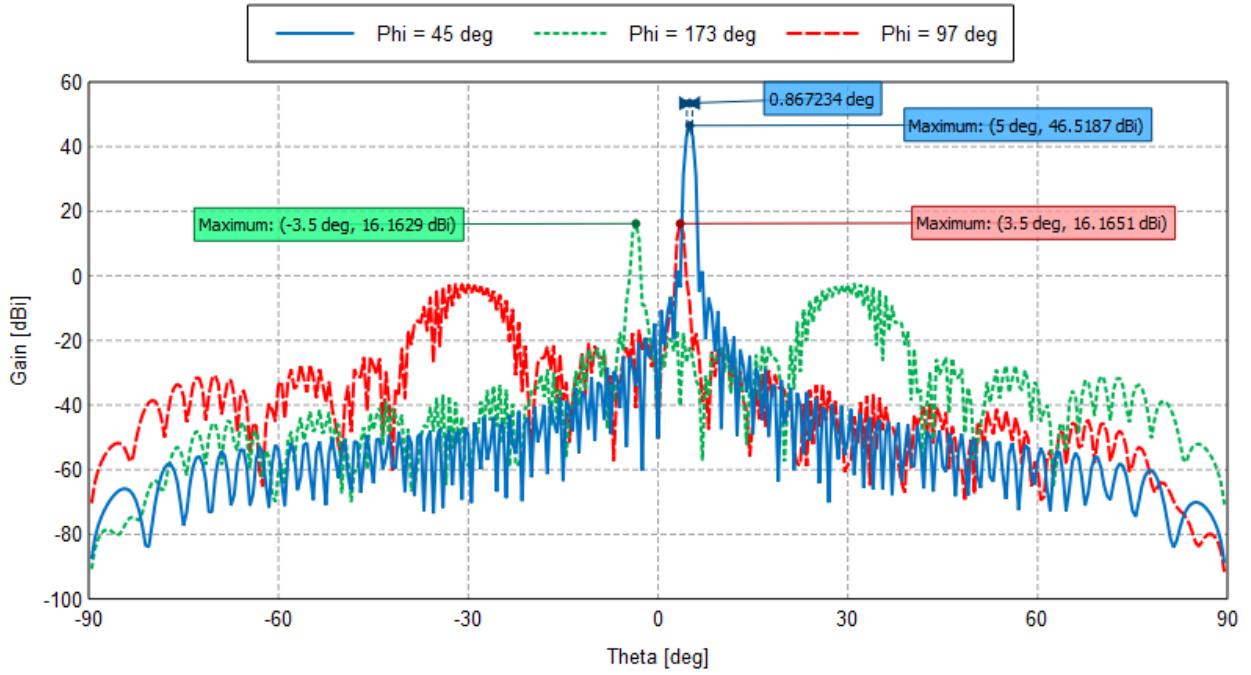


Figure 24: Resulting radiation pattern when system is steered to  $\phi=45^\circ$ ,  $\theta=5^\circ$ .

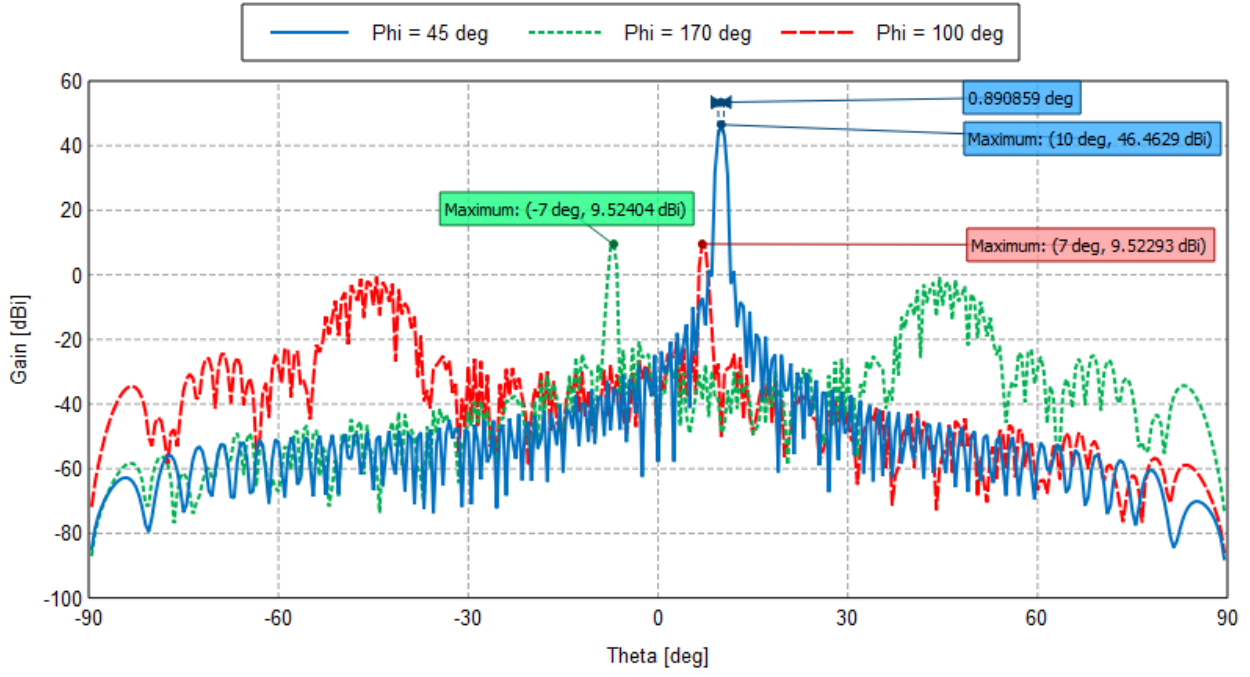


Figure 25: Resulting radiation pattern when system is steered to  $\phi=45^\circ$ ,  $\theta=10^\circ$ .

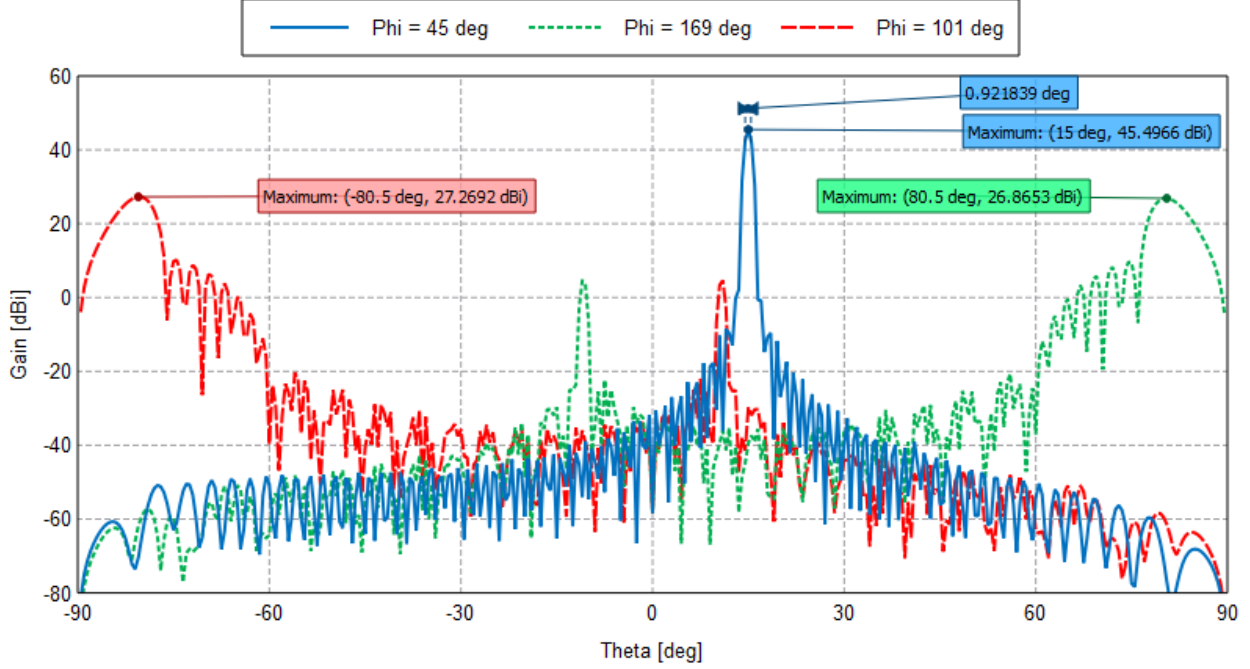


Figure 26: Resulting radiation pattern when system is steered to  $\phi=45^\circ$ ,  $\theta=15^\circ$ .

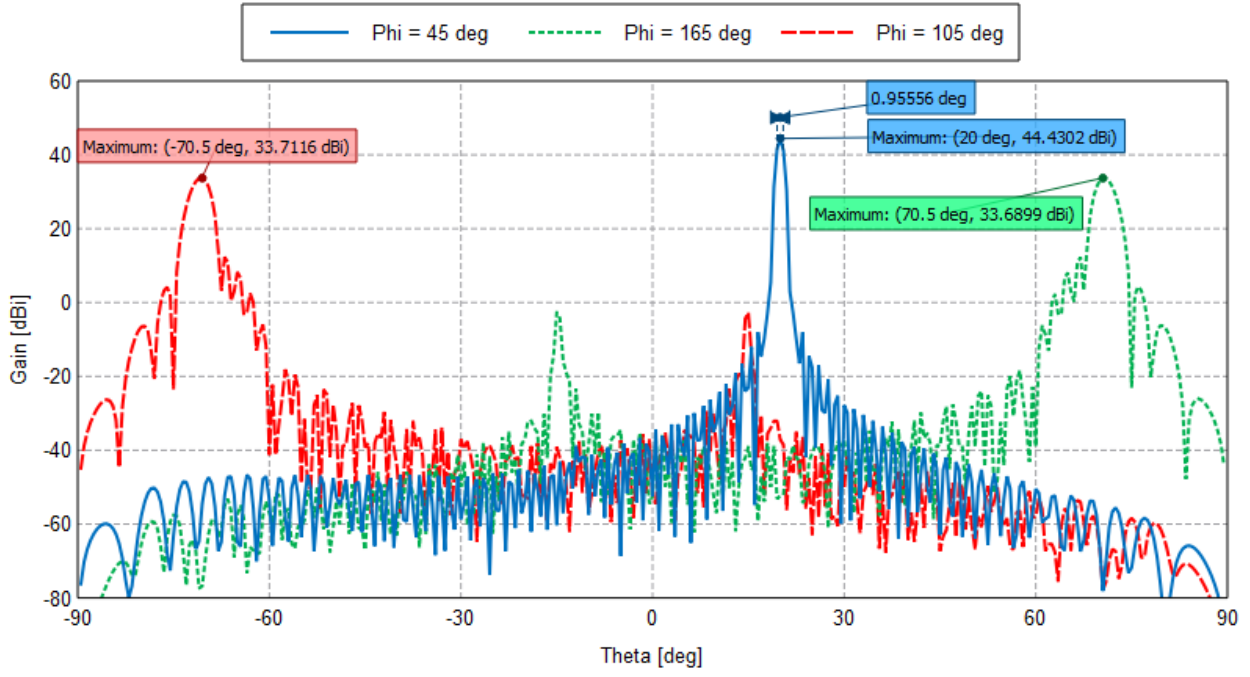


Figure 27: Resulting radiation pattern when system is steered to  $\phi=45^\circ$ ,  $\theta=20^\circ$ .

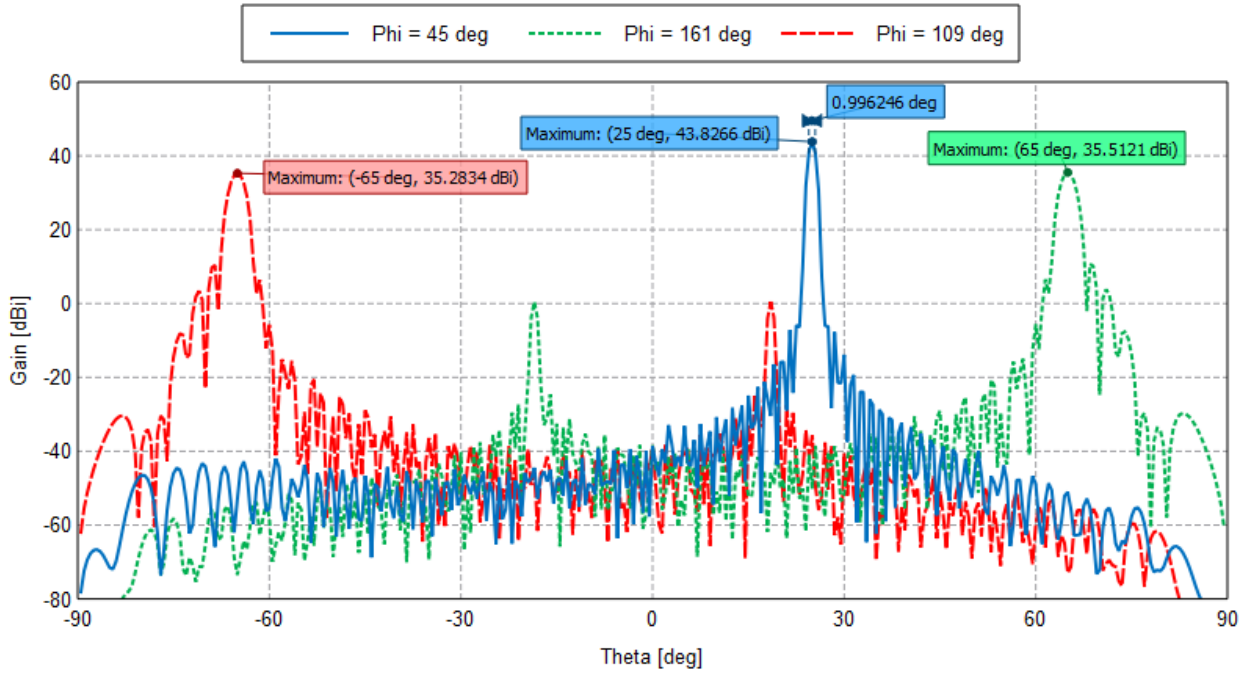


Figure 28: Resulting radiation pattern when system is steered to  $\phi=45^\circ$ ,  $\theta=25^\circ$ .



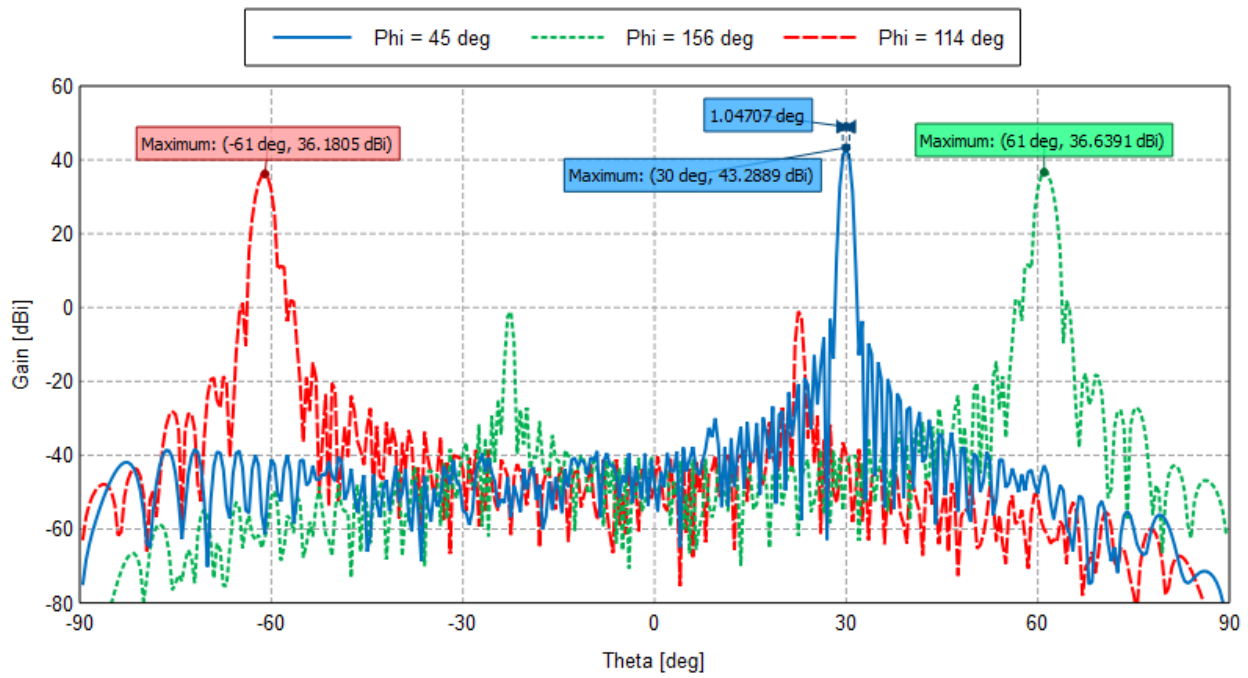


Figure 29: Resulting radiation pattern when system is steered to  $\phi=45^\circ$ ,  $\theta=30^\circ$ .

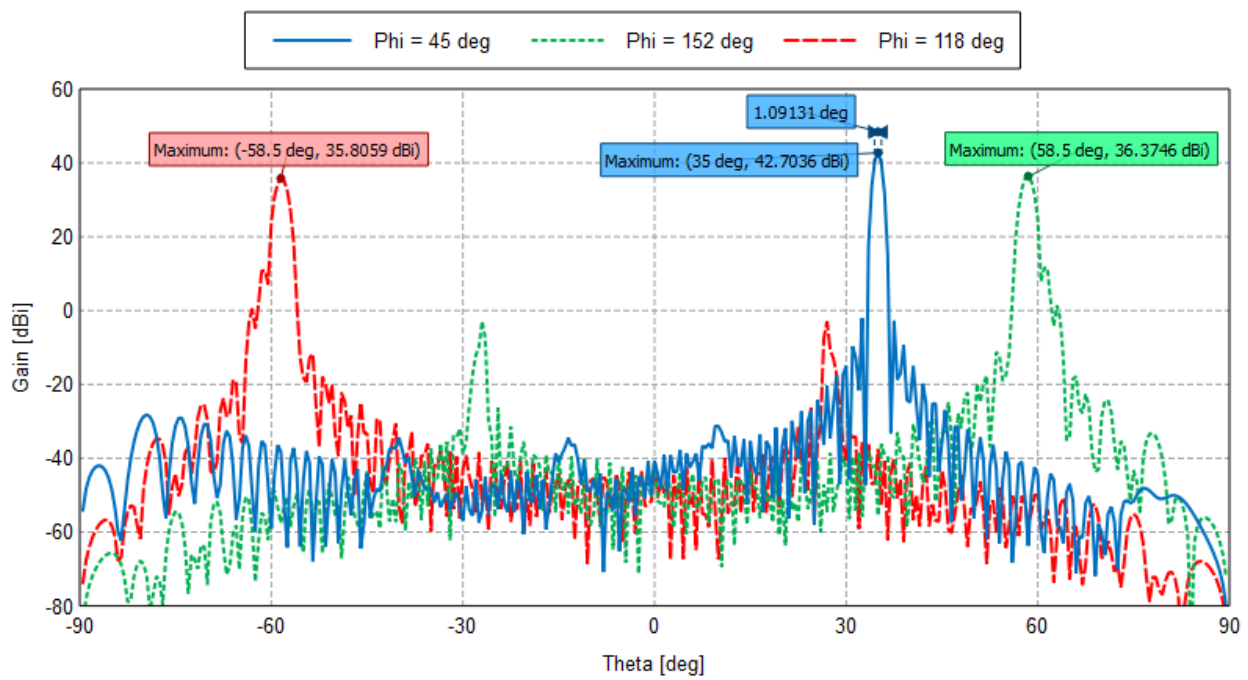


Figure 30: Resulting radiation pattern when system is steered to  $\phi=45^\circ$ ,  $\theta=35^\circ$ .

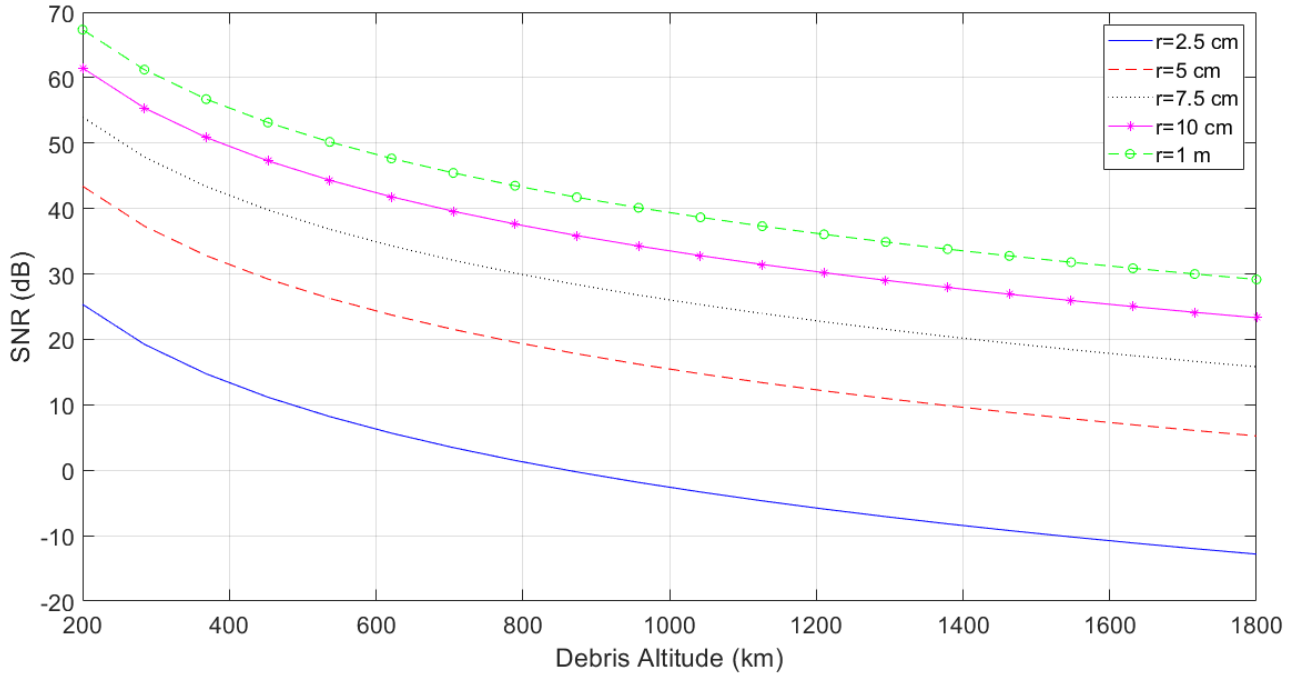


Figure 31: Sensitivity of the main beam when the system is steered to  $\phi=0^\circ$ ,  $\theta=0^\circ$ .

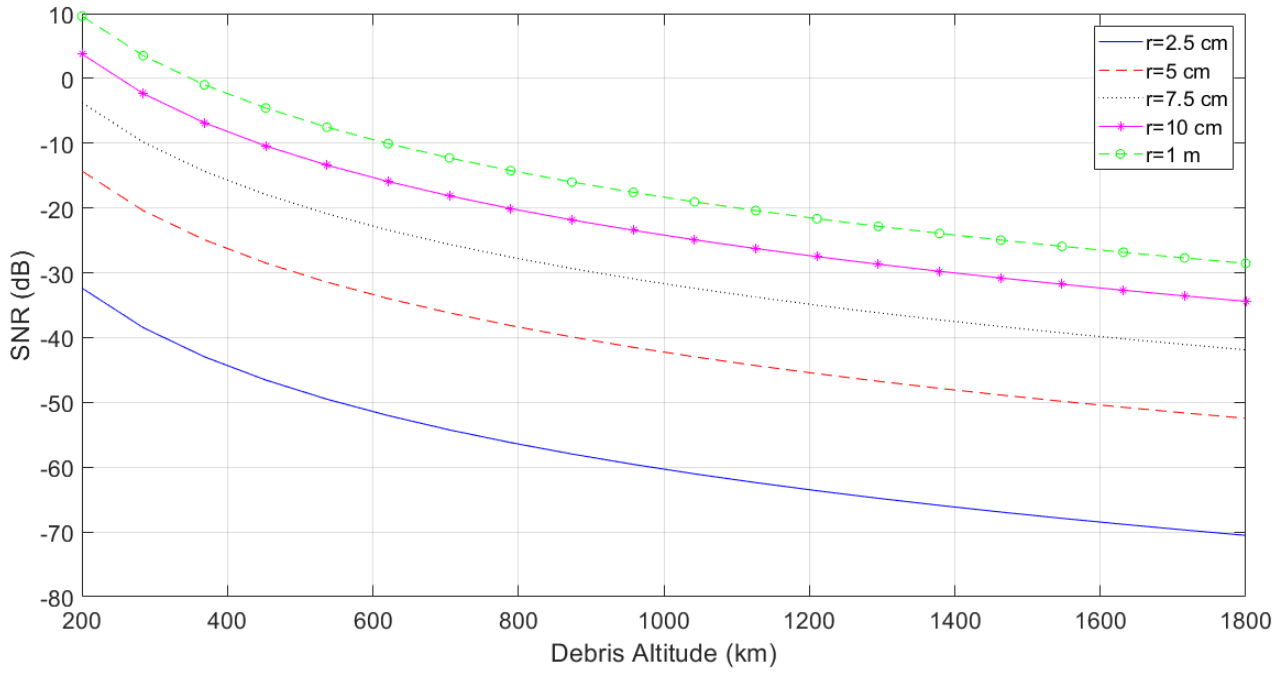


Figure 32: Sensitivity of the most dominant side lobe ( $\theta=\pm 2.99^\circ$ ) when the system is steered to  $\phi=0^\circ$ ,  $\theta=0^\circ$ .

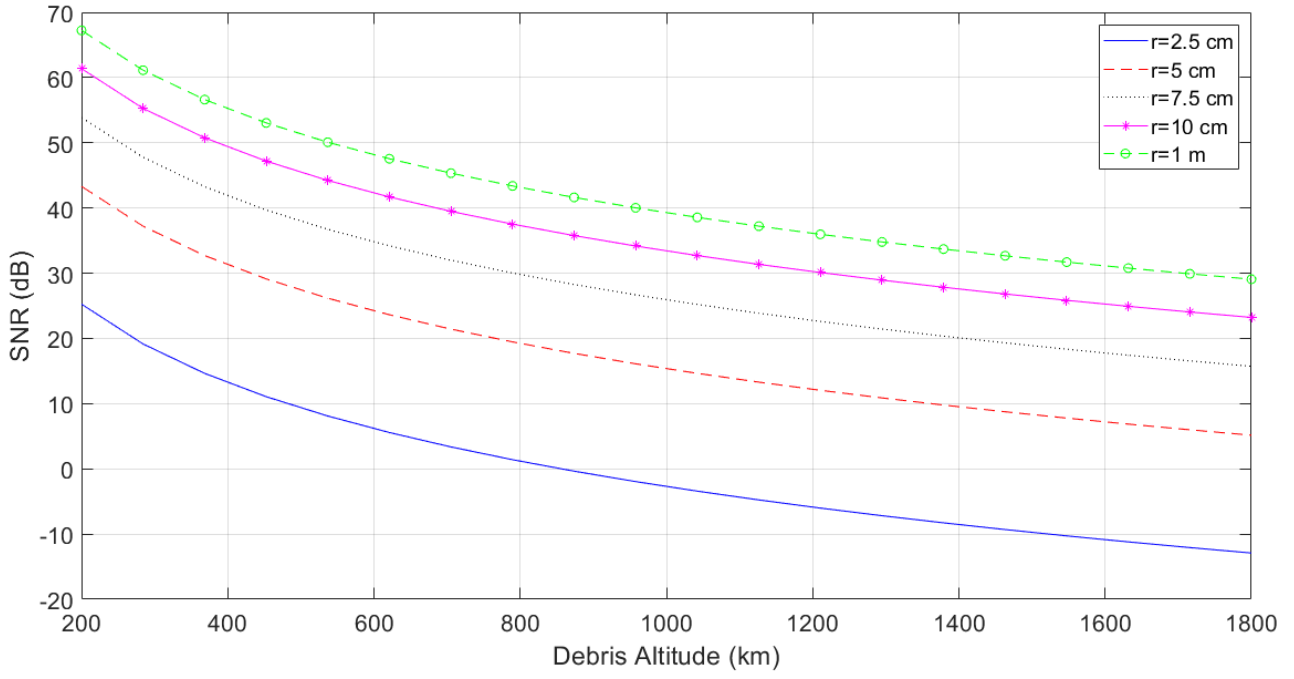


Figure 33: Sensitivity of the main beam when the system is steered to  $\phi=0^\circ$ ,  $\theta=5^\circ$ .

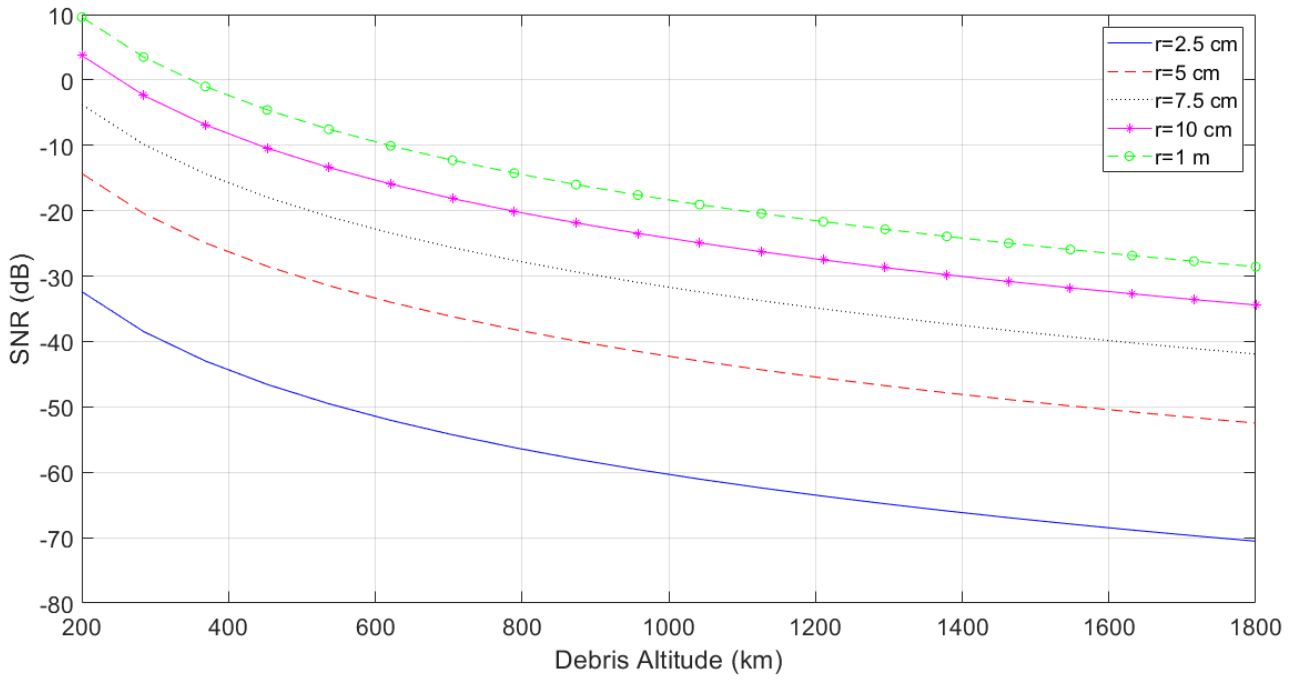


Figure 34: Sensitivity of the most dominant side lobe ( $\theta=-2.01^\circ$ ) when the system is steered to  $\phi=0^\circ$ ,  $\theta=5^\circ$ .

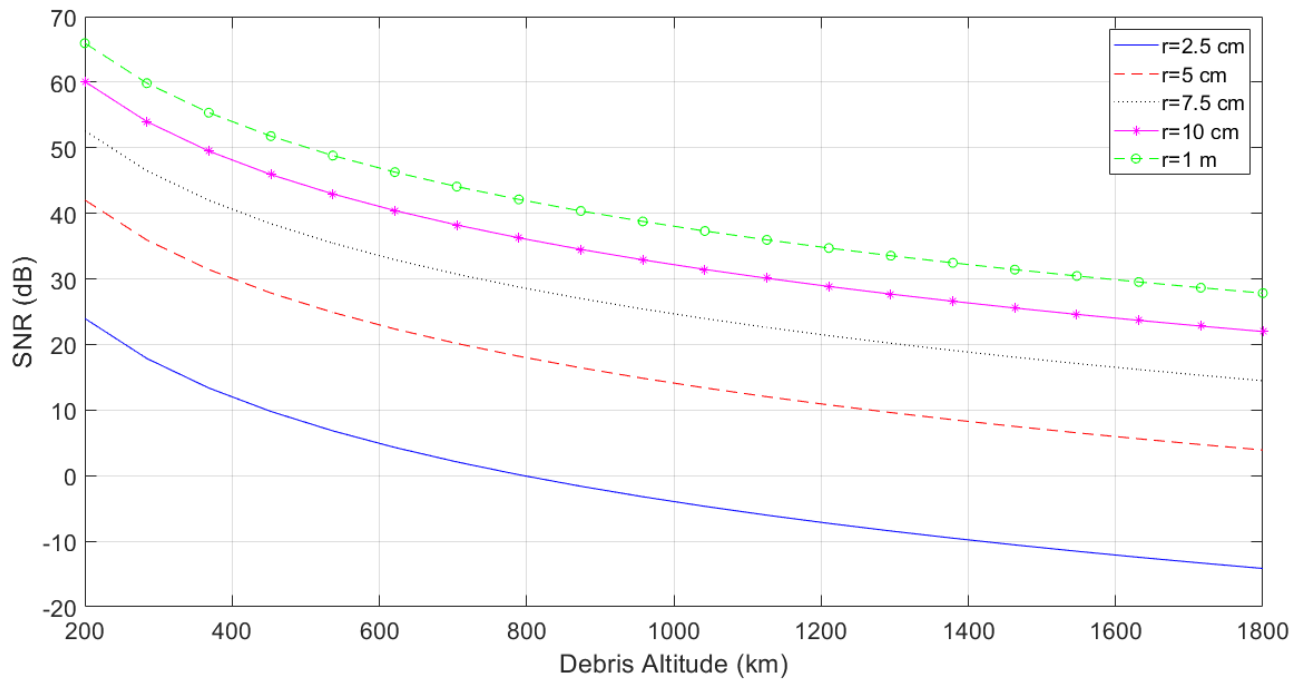


Figure 35: Sensitivity of the main beam when the system is steered to  $\phi=0^\circ$ ,  $\theta=10^\circ$ .

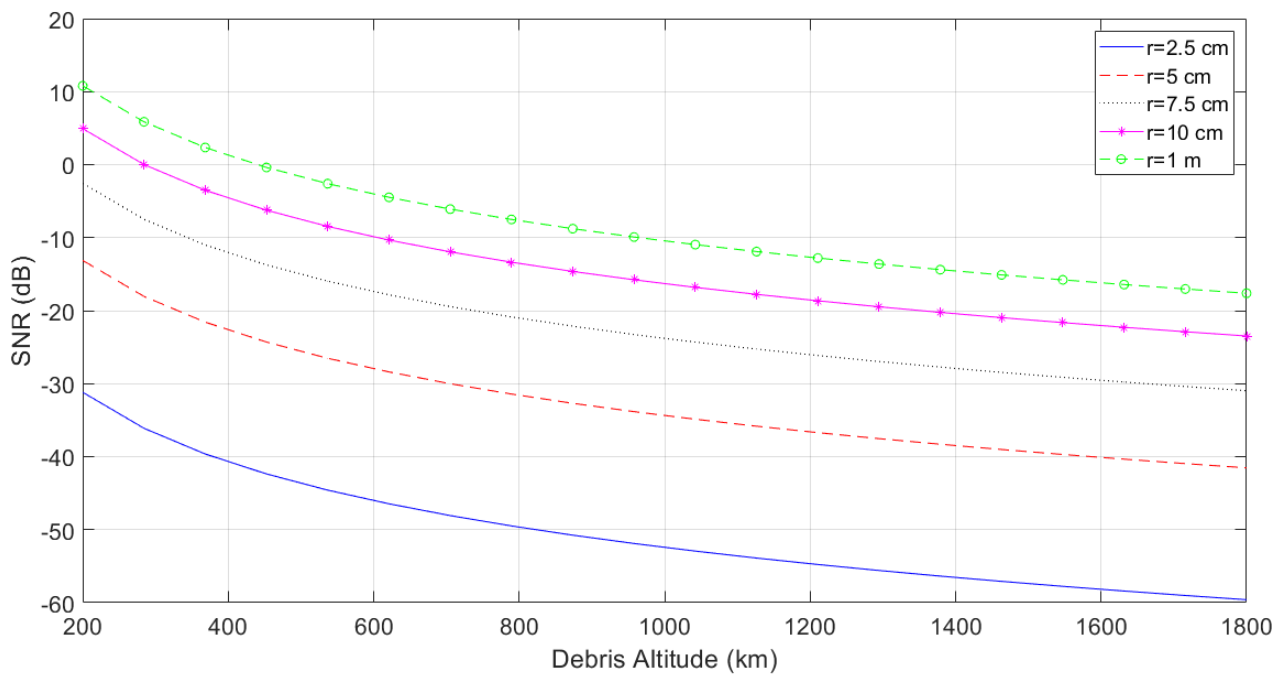


Figure 36: Sensitivity of the most dominant side lobe ( $\theta=-78.5^\circ$ ) when the system is steered to  $\phi=0^\circ$ ,  $\theta=10^\circ$ .

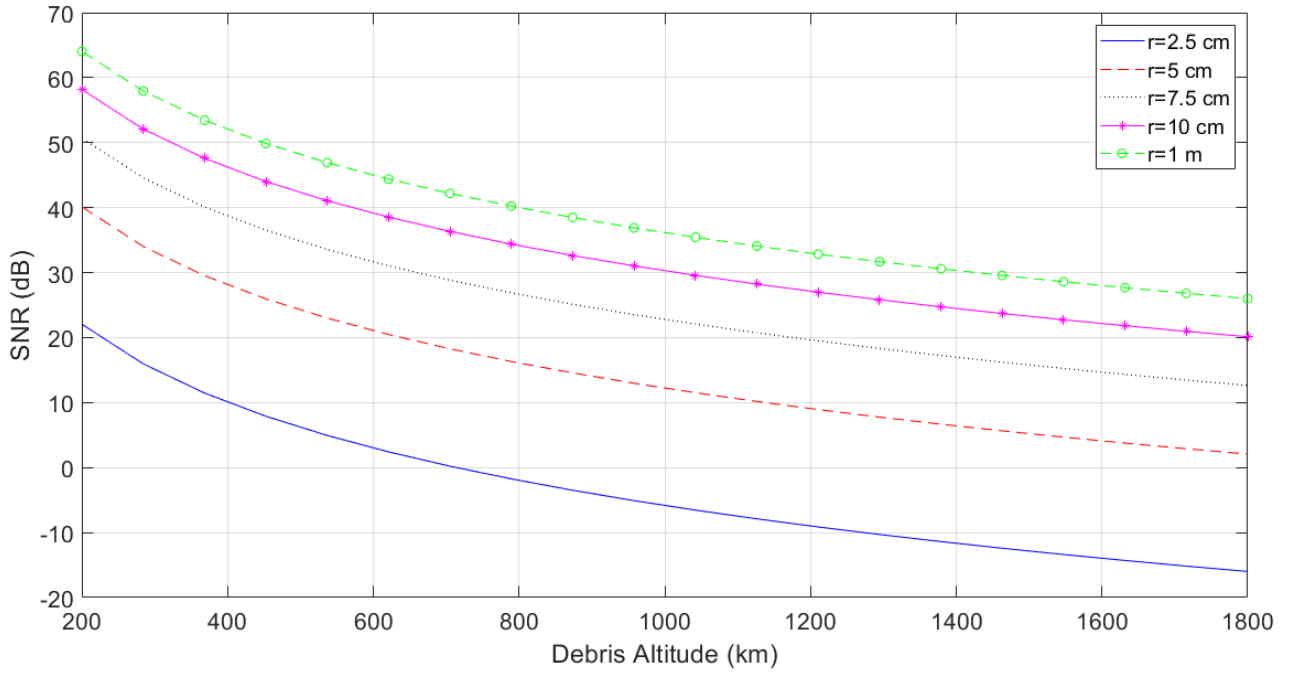


Figure 37: Sensitivity of the main beam when the system is steered to  $\phi=0^\circ$ ,  $\theta=15^\circ$ .

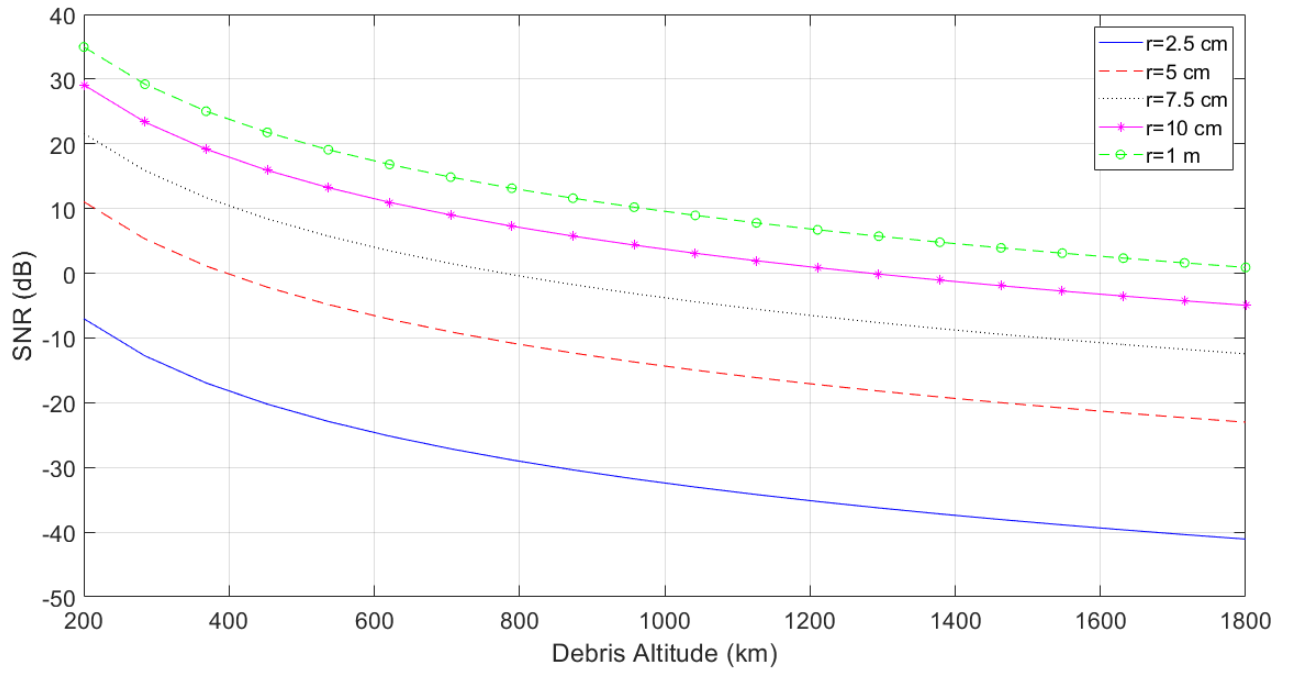


Figure 38: Sensitivity of the most dominant side lobe ( $\theta=-63.5^\circ$ ) when the system is steered to  $\phi=0^\circ$ ,  $\theta=15^\circ$ .

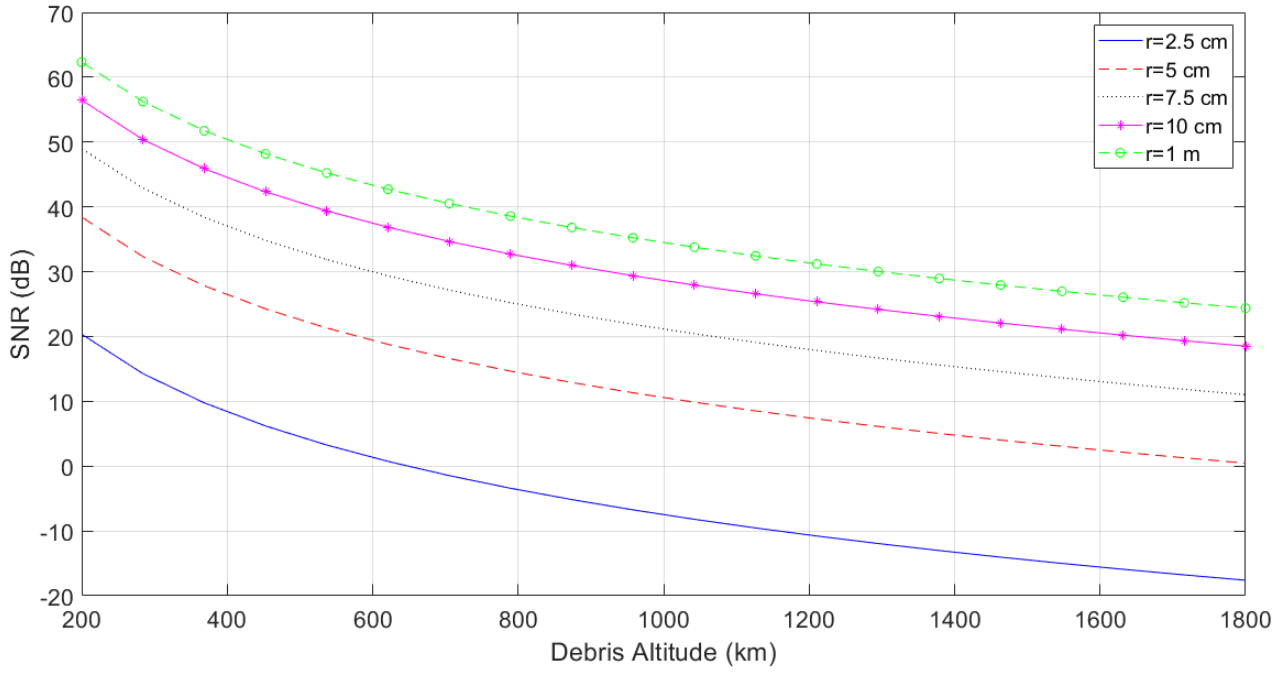


Figure 39: Sensitivity of the main beam when the system is steered to  $\phi=0^\circ$ ,  $\theta=20^\circ$ .

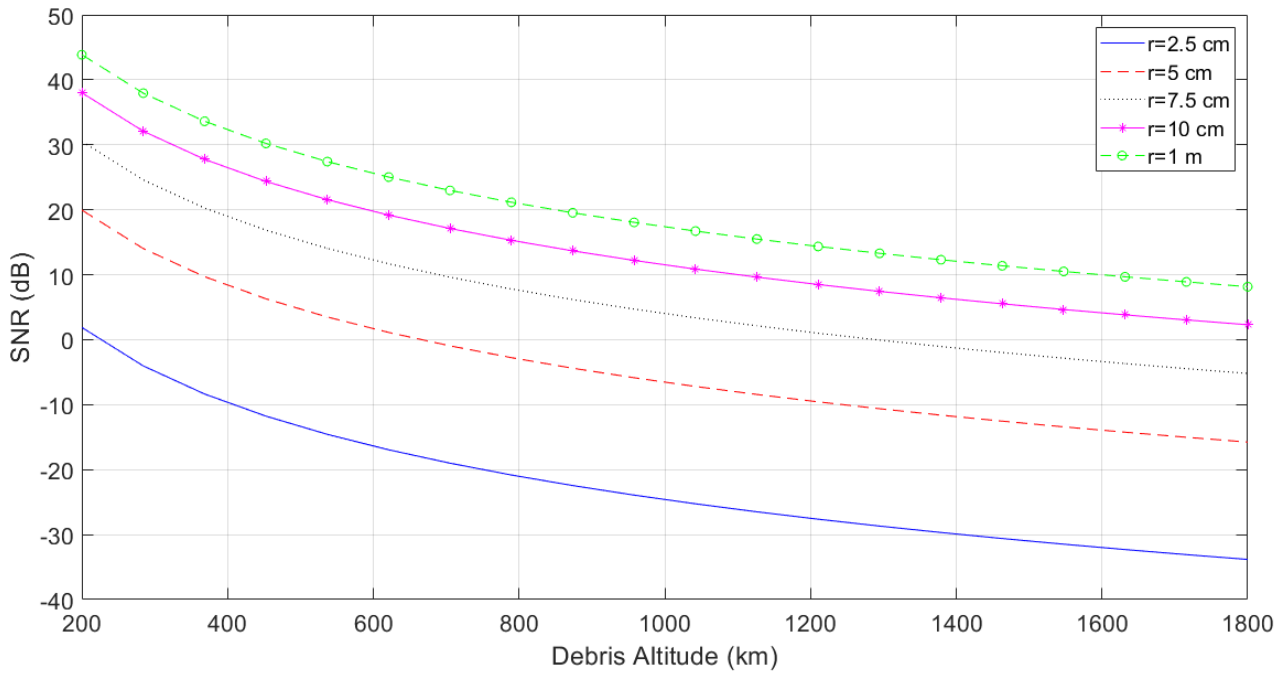


Figure 40: Sensitivity of the most dominant side lobe ( $\theta=-54.5^\circ$ ) when the system is steered to  $\phi=0^\circ$ ,  $\theta=20^\circ$ .

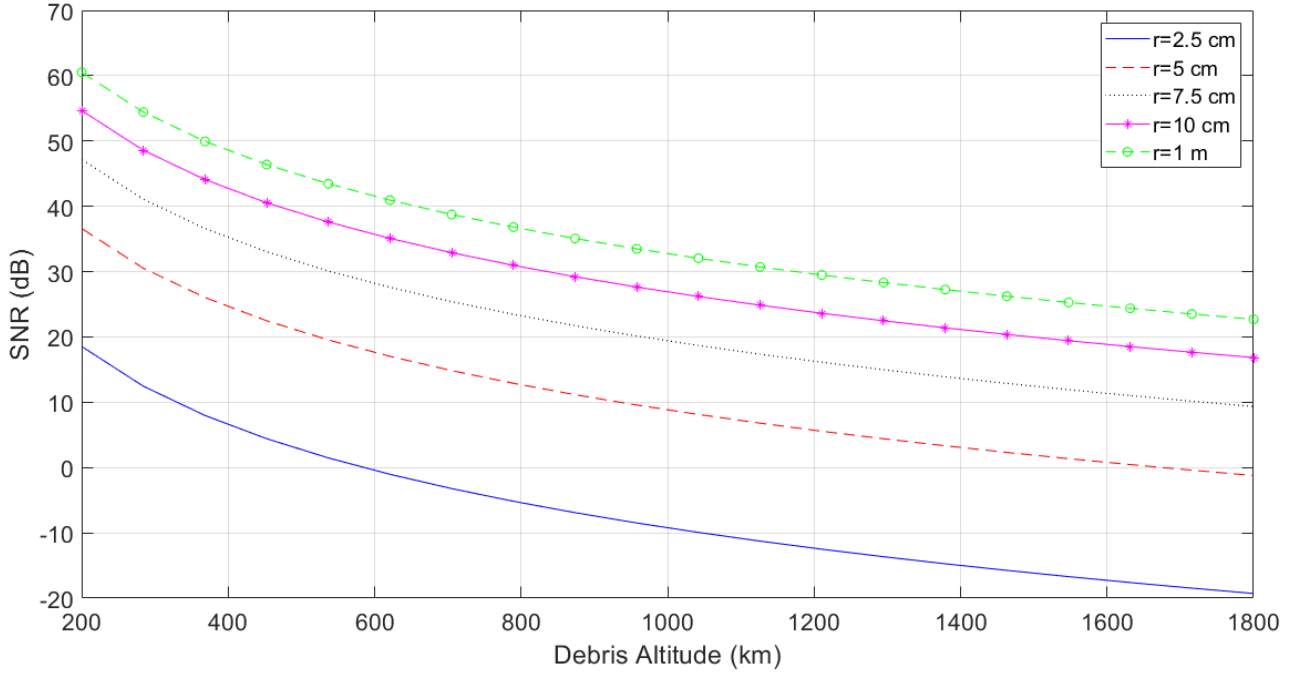


Figure 41: Sensitivity of the main beam when the system is steered to  $\phi=0^\circ$ ,  $\theta=25^\circ$ .

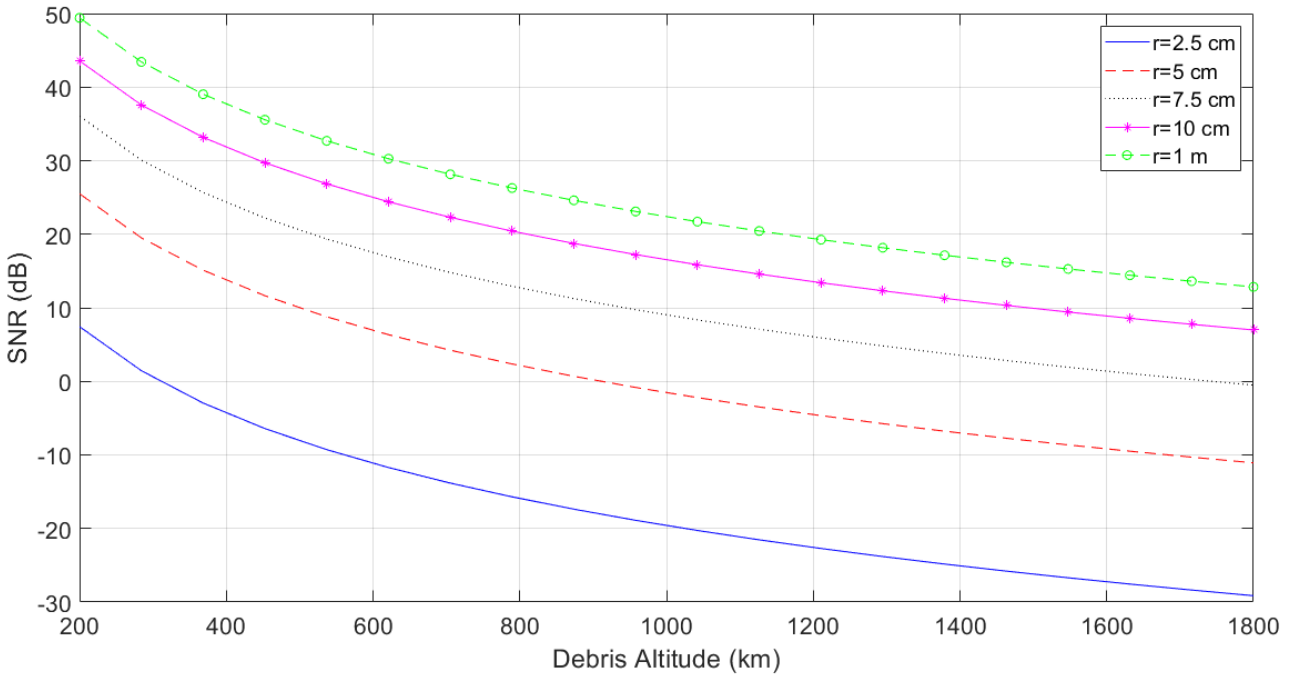


Figure 42: Sensitivity of the most dominant side lobe ( $\theta=-47^\circ$ ) when the system is steered to  $\phi=0^\circ$ ,  $\theta=25^\circ$ .

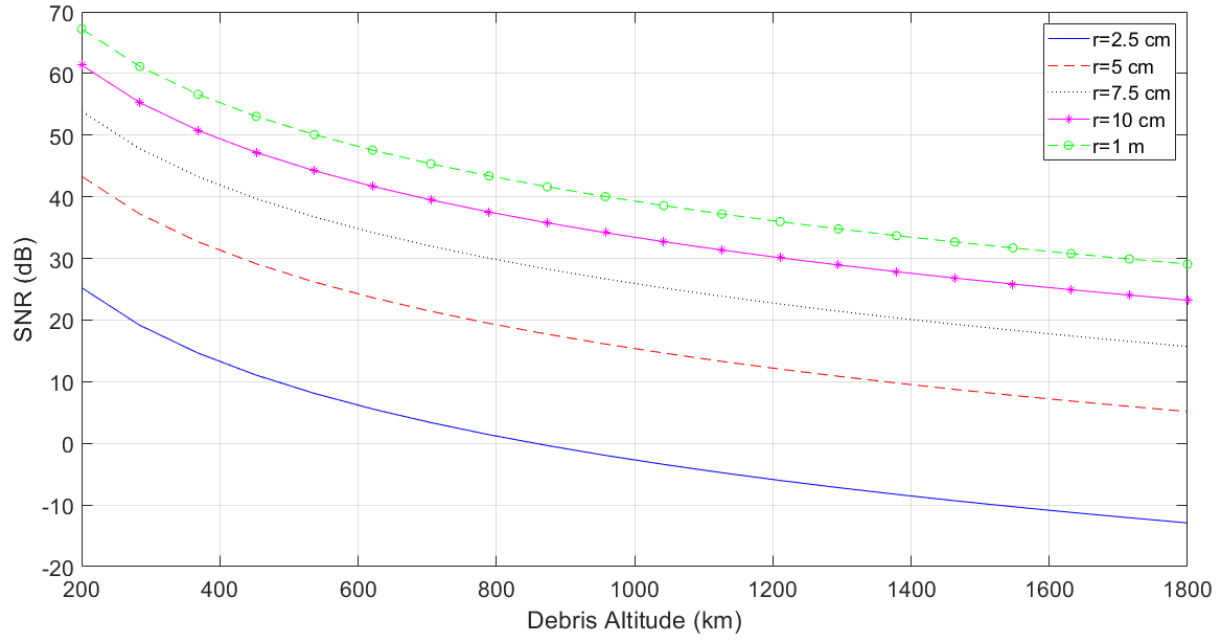


Figure 43: Sensitivity of the main beam when the system is steered to  $\phi=45^\circ$ ,  $\theta=5^\circ$ .

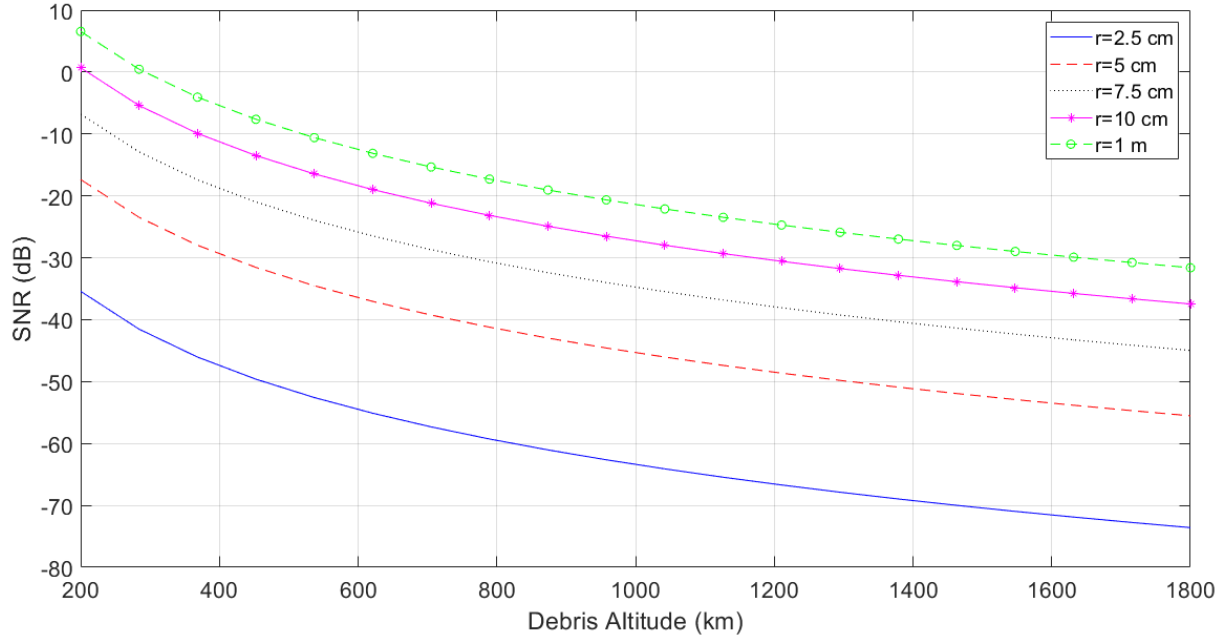


Figure 44: Sensitivity of the most dominant side lobes ( $\phi=173^\circ$ ,  $\theta=-3.5^\circ$  and  $\phi=97^\circ$ ,  $\theta=3.5^\circ$ ) when the system is steered to  $\phi=45^\circ$ ,  $\theta=5^\circ$ .



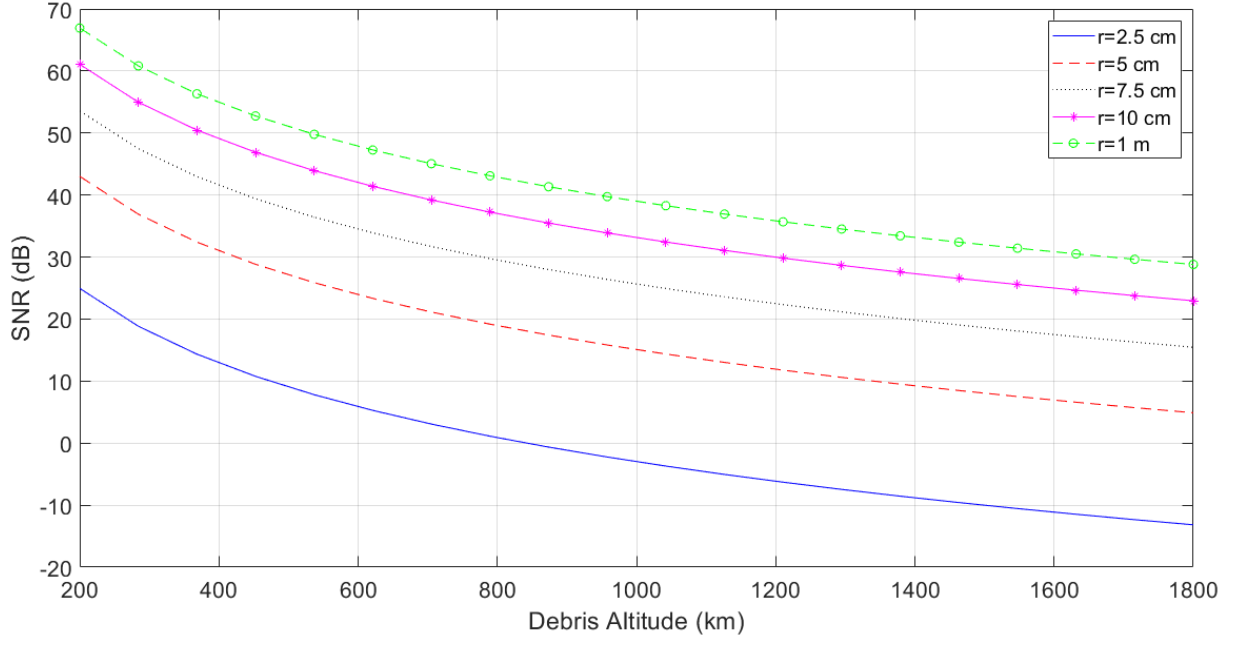


Figure 45: Sensitivity of the main beam when the system is steered to  $\phi=45^\circ$ ,  $\theta=10^\circ$ .

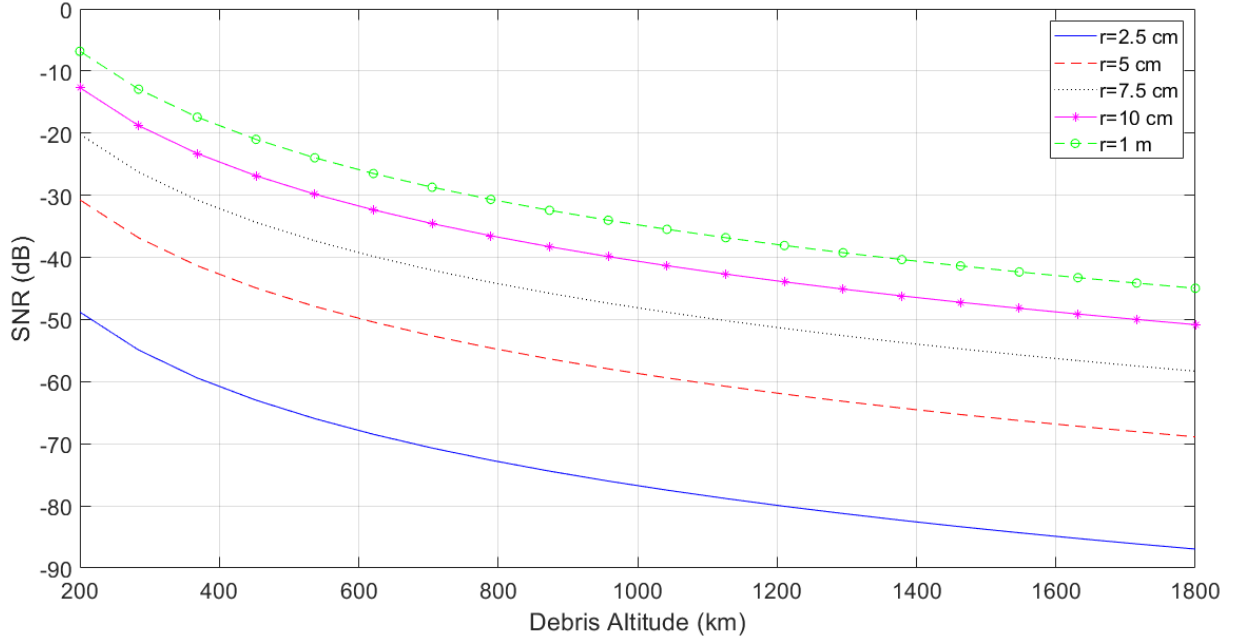


Figure 46: Sensitivity of the most dominant side lobes ( $\phi=170^\circ$ ,  $\theta=-7^\circ$  and  $\phi=100^\circ$ ,  $\theta=7^\circ$ ) when the system is steered to  $\phi=45^\circ$ ,  $\theta=10^\circ$ .

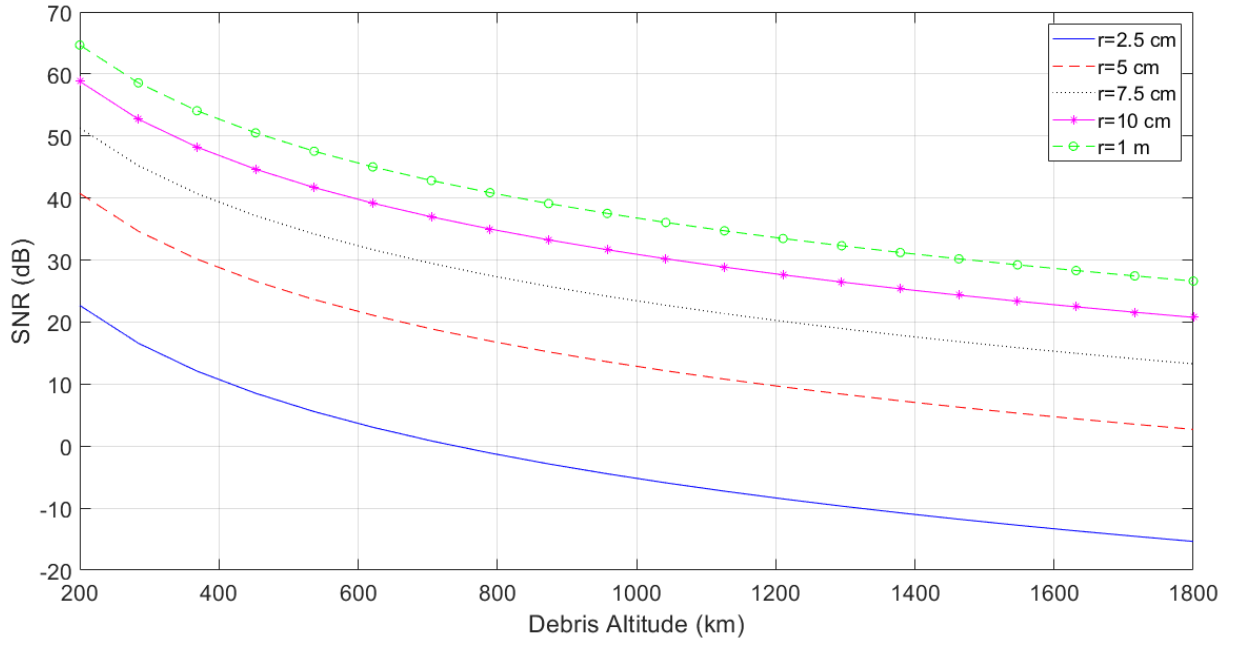


Figure 47: Sensitivity of the main beam when the system is steered to  $\phi=45^\circ$ ,  $\theta=15^\circ$ .

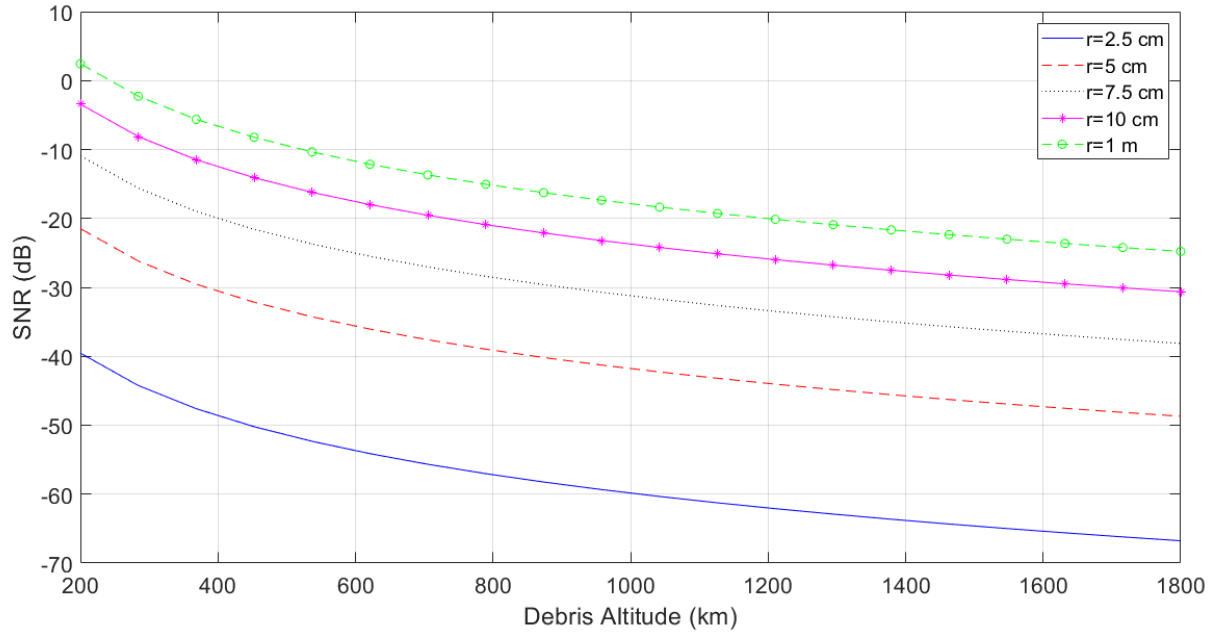


Figure 48: Sensitivity of the most dominant side lobes ( $\phi=169^\circ$ ,  $\theta=80.5^\circ$  and  $\phi=101^\circ$ ,  $\theta=-80.5^\circ$ ) when the system is steered to  $\phi=45^\circ$ ,  $\theta=15^\circ$ .

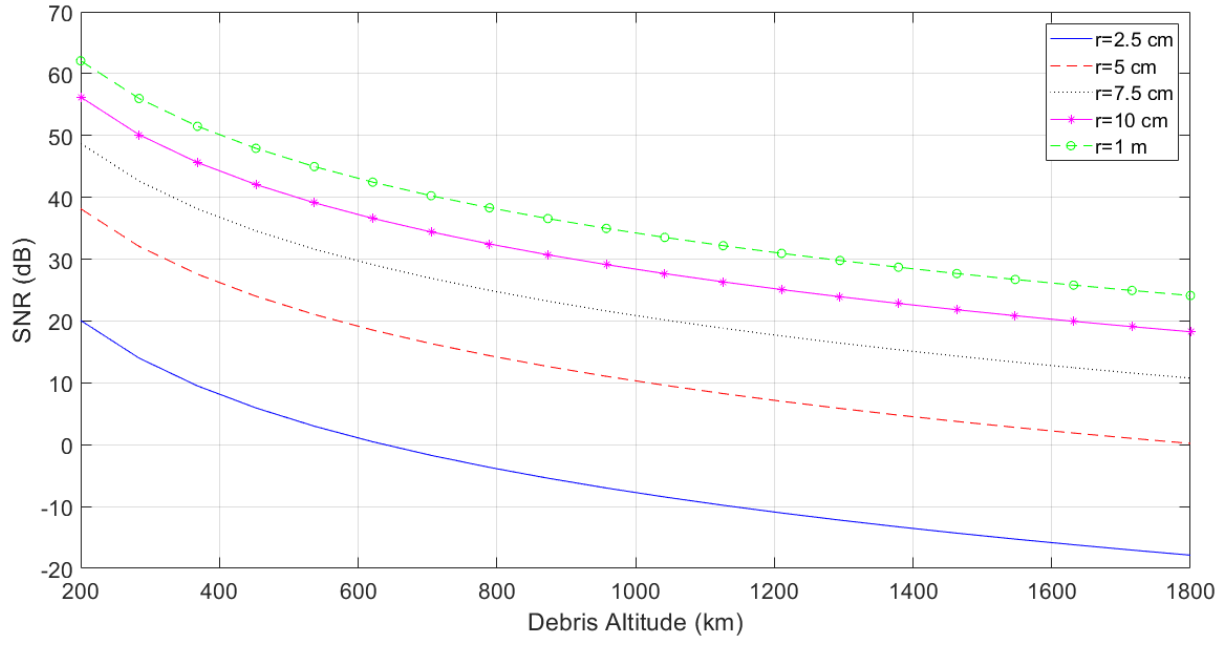


Figure 49: Sensitivity of the main beam when the system is steered to  $\phi=45^\circ$ ,  $\theta=20^\circ$ .

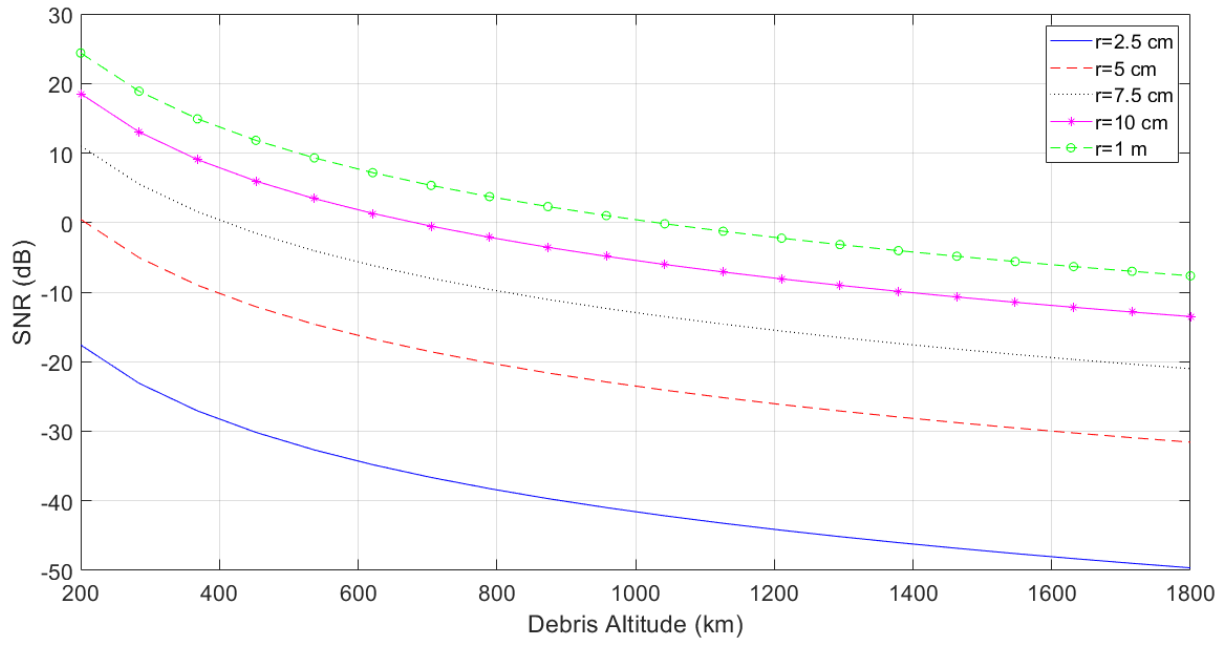


Figure 50: Sensitivity of the most dominant side lobes ( $\phi=165^\circ$ ,  $\theta=70.5^\circ$  and  $\phi=105^\circ$ ,  $\theta=-70.5^\circ$ ) when the system is steered to  $\phi=45^\circ$ ,  $\theta=20^\circ$ .

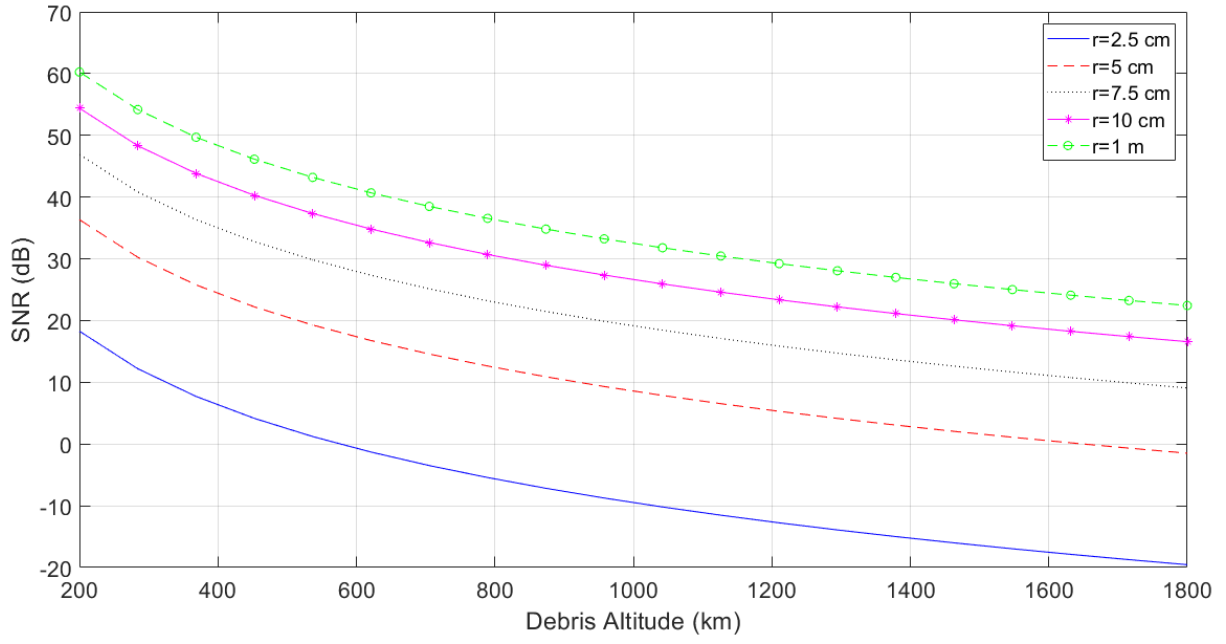


Figure 51: Sensitivity of the main beam when the system is steered to  $\phi=45^\circ$ ,  $\theta=25^\circ$ .

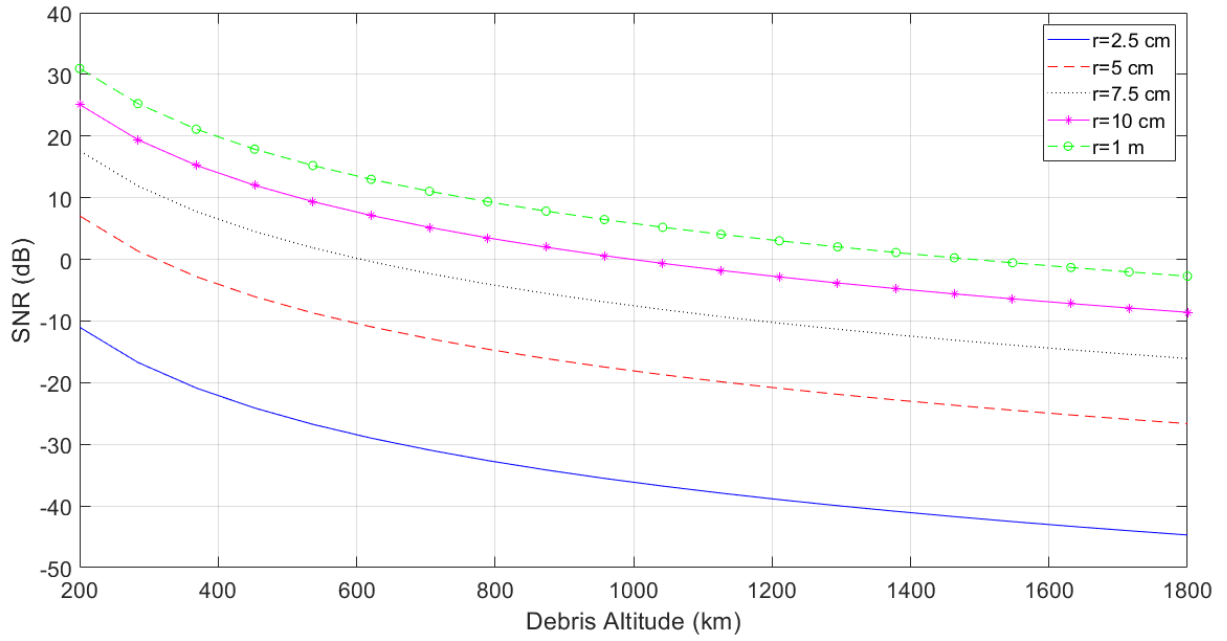


Figure 52: Sensitivity of the most dominant side lobes ( $\phi=161^\circ$ ,  $\theta=65^\circ$  and  $\phi=109^\circ$ ,  $\theta=-65^\circ$ ) when the system is steered to  $\phi=45^\circ$ ,  $\theta=25^\circ$ .

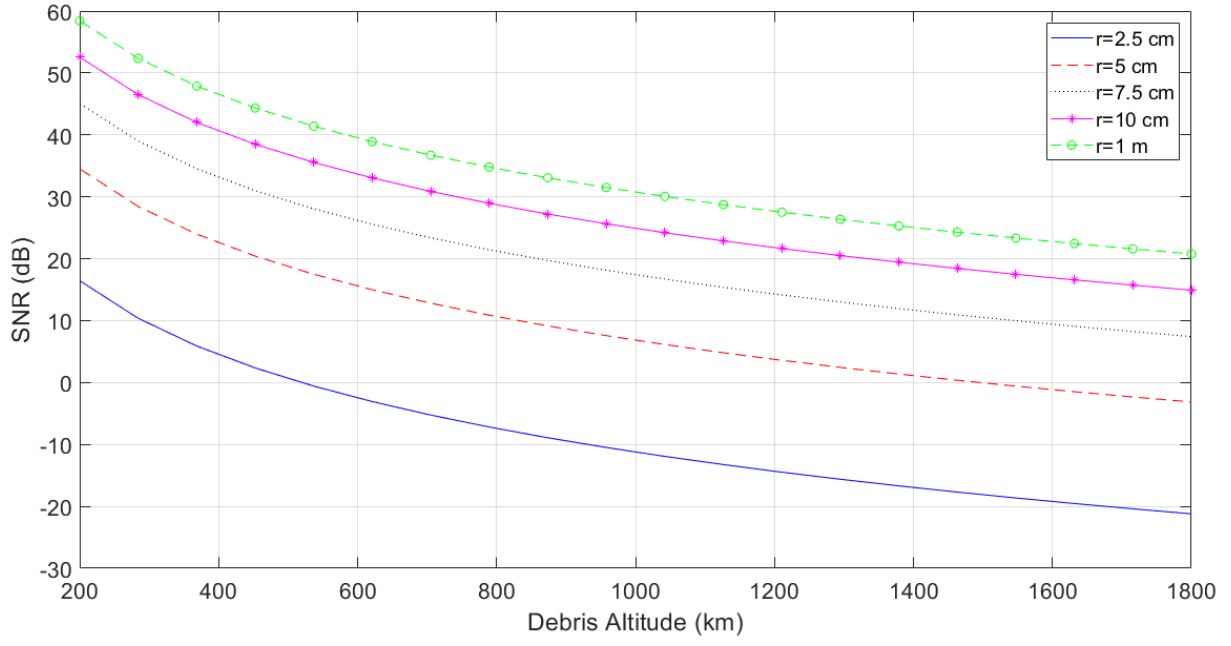


Figure 53: Sensitivity of the main beam when the system is steered to  $\phi=45^\circ$ ,  $\theta=30^\circ$ .

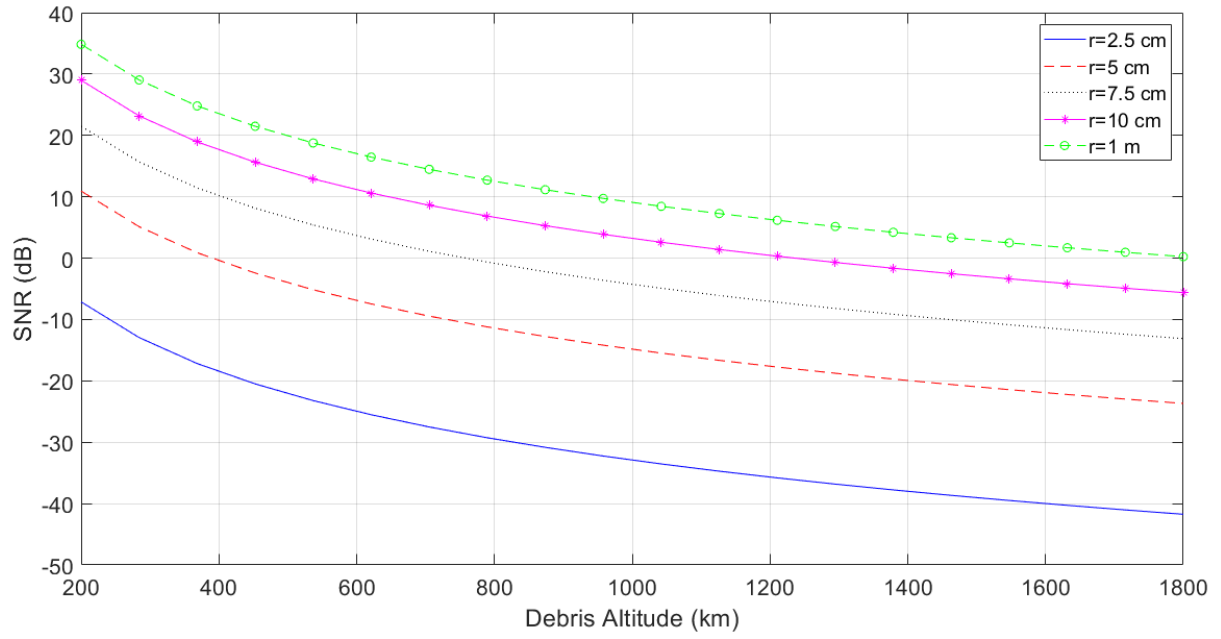


Figure 54: Sensitivity of the most dominant side lobes ( $\phi=156^\circ$ ,  $\theta=61^\circ$  and  $\phi=114^\circ$ ,  $\theta=-61^\circ$ ) when the system is steered to  $\phi=45^\circ$ ,  $\theta=30^\circ$ .

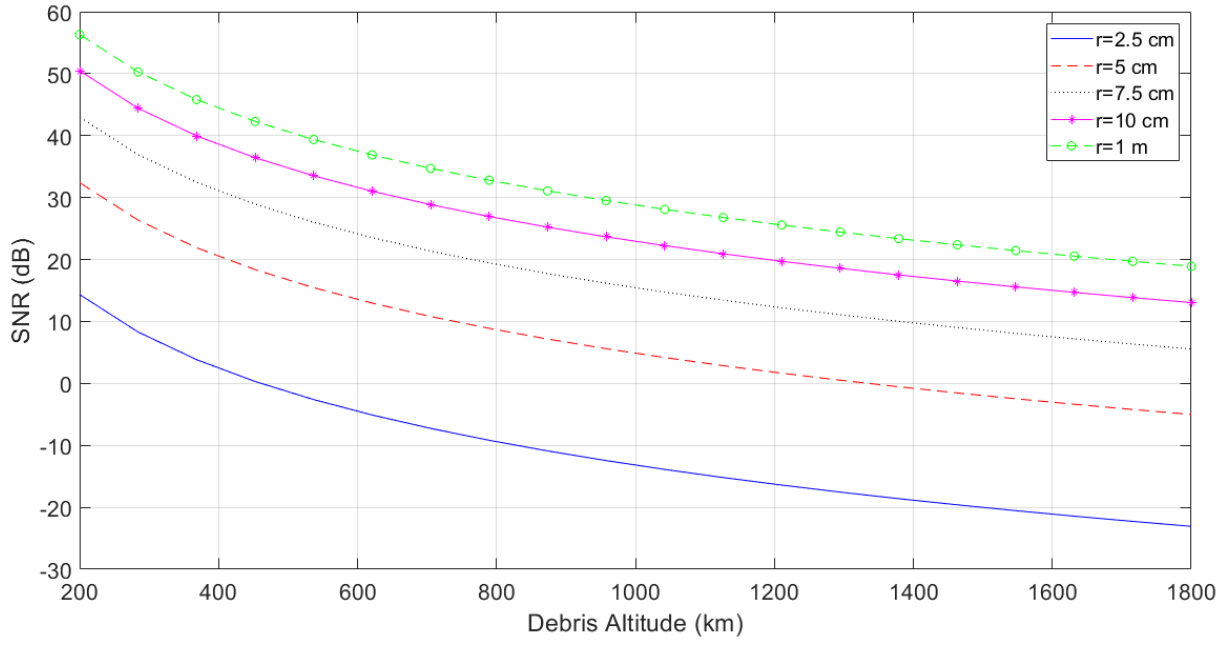


Figure 55: Sensitivity of the main beam when the system is steered to  $\phi=45^\circ$ ,  $\theta=35^\circ$ .

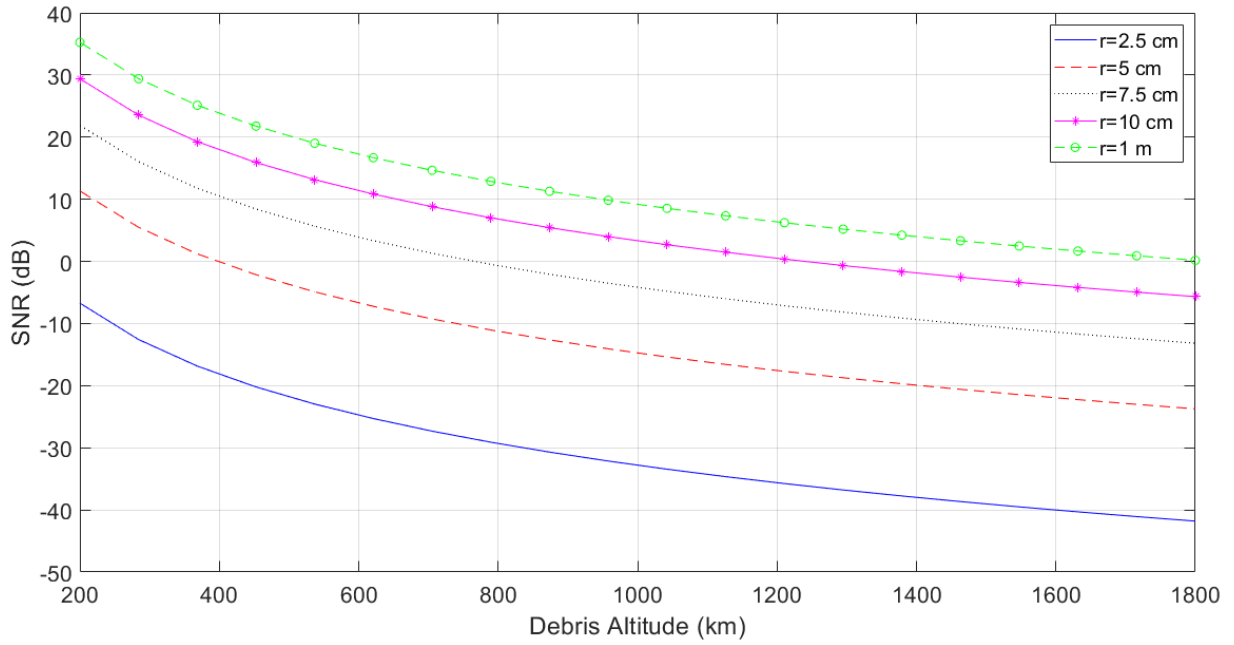


Figure 56: Sensitivity of the most dominant side lobes ( $\phi=152^\circ$ ,  $\theta=58.5^\circ$  and  $\phi=118^\circ$ ,  $\theta=-58.5^\circ$ ) when the system is steered to  $\phi=45^\circ$ ,  $\theta=35^\circ$ .

Table 1: Summary of the properties of the phased array radar

Property	Value
No. Elements	5776
Maximum gain ( $\theta=0^\circ$ )	46.54 dBi
Minimum gain ( $\theta=35^\circ$ )	42.70 dBi
Minimum HPBW ( $\theta=0^\circ$ )	$0.83^\circ$
Maximum HPBW ( $\theta=35^\circ$ )	$1.09^\circ$
FOV ( $\phi=0^\circ$ )	$\pm\theta=25^\circ$
FOV ( $\phi=45^\circ$ )	$\pm\theta=35^\circ$
FOV ( $\phi=90^\circ$ )	$\pm\theta=25^\circ$
FOV ( $\phi=135^\circ$ )	$\pm\theta=35^\circ$
Pulse width	$37 \mu s$
PRF	64.86 Hz
Peak Transmit Power	1 MW
Peak Input Transmit Power	2 MW
Average Transmit Power	2.4 kW
Average Input Transmit Power	4.8 kW

## I Cost Analysis

The cost analysis of the phased array radar was limited to the electrical components required to deliver the required power to all the elements in the array, important physical features of the array as well as the engineering hours, manual labour hours and price of suitably priced property for an area of implementation. All costing with regards to power supply infrastructure, data transfer storage and distribution infrastructure and signal processing of the system were not included and should be considered in the cost analysis as the system is developed further. All components that had to be imported were converted to ZAR at the exchange rate of R 14.40 USD<sup>-1</sup>. The most expensive component of the system was found to be the transmit/receive (T/R) module that would be required at every radiating element of the array. After extensive research into the pricing of these devices without obtaining a figure, it was decided that the device would be priced according to the individual components that it contains. The device consisted of a power amplifier, low noise amplifier (LNA), a digitally controllable phase shifter and two circulators. The most expensive component within the T/R module was the power amplifier rated at 350 W which cost approximately R 110692 [32]. The prices of this component was estimated by considering the price of 100 W and 50 W amplifiers [32]. The cost of the crossed dipole was calculated by using the price two 61.24 cm aluminium tubes having an outer diameter of 2.5 cm and a thickness of 2 mm [33]. The ground plane price was estimated using the price of an aluminium grid with 5 cm ( $\approx \frac{\lambda}{10}$ ) square holes [33]. Aluminium was selected as the material for these components as it was more resistant to environmental effects including corrosion.

As mentioned in the main report, a shortfall of the design of the radar system was the lack of an appropriate distributed feed network to provide each T/R module with a 440 MHz tone since 5776 was not a square number. In order to approximate the required number and length of power splitters and low loss coaxial cable respectively, an average between the  $2^{12}$  and  $2^{13}$  for number of array elements was used to acquire the relevant pricing for each component. It is for this reason that these quantities are represented with the \*\* symbol.

The cost of a plot in Brandvlei was included to approximate the effect of the Land Acquisition Process (LAP) if a partnership with the SKA was formed. The size of this property was 1370 ha. This property was larger than what was required for implementation of the array but was seen as an appropriate estimation of the price of property if it was required. It was assumed that the number of engineering hours required was equal to the engineering hours logged by the author in completing the design and

analysis of the system so far. Engineering rates that were applied were the same as those at Alaris Antennas and therefore met ECSA requirements [34, 35]. Finally, it was estimated that 10 manual labour workers would be required to fit, install and test all modular components of the system, each working for three 5-day weeks for 8 hours a day.

Table 2: Cost analysis for the construction of the phased array radar

<b>Component</b>	<b>Price per component (R)</b>	<b>Quantity</b>	<b>Total (R)</b>
Crossed Dipole Antenna	134.82	5776	778720.32
Ground plane	128.57	2209	284011.13
T/R Module	112703.36	5776	650974607.40
Power Splitter	647.28	**	8087.50
Circulator	500	5777	2888500
$\frac{\lambda}{4}$ low loss coaxial cable	588.67	**	7232988.29
Oscillator	1583.28	1	1583.28
Property	2500000	1	2500000
Engineering Hours	1300	240	312000
Manual Labour Hours	80	1200	96000
<b>Total</b>			<b>664 795 697.90</b>